REVIEW

ADVANCED ENERGY MATERIALS
www.advenergymat.de

3D Host Design Strategies Guiding “Bottom–Up” Lithium Deposition: A Review

Xi Wang, Zhen Chen, Kai Jiang, Minghua Chen,* and Stefano Passerini**

Lithium metal batteries (LMBs) have the potential to be the next-generation rechargeable batteries due to the high theoretical specific capacity and the lowest redox potential of lithium metal. However, the practical application of LMBs is hindered by challenges such as the uncontrolled growth of lithium dendrites, unstable solid electrolyte interphase (SEI), and excessive volume change of Li metal. To solve these issues, the design of high-performance lithium metal anodes (LMAs) with various 3D structures is critical. Targeting at realizing the “bottom–up” Li deposition to fully utilize the 3D architecture, in recent years, strategies such as gradient host materials construction, magnetic field modulation, SEI component design, and so on have attracted intensive attention. This review begins with a fundamental discussion of the Li nucleation and deposition mechanism. The recent advances in the aspects of construction strategies and modification methods that enable the “bottom–up” Li deposition within advanced 3D host materials, with a particular emphasize on their design principles are comprehensively overviewed. Finally, future challenges and perspectives on the design of advanced hosts toward practical LMAs are proposed.

1. Introduction

With the energy density of lithium-ion batteries approaching its limit, next-generation energy storage systems with substantially higher energy density are critically needed to meet the demands of long-range electric vehicles and large-scale grid storage.[1,2] Lithium metal exhibits over tenfolds the theoretical specific capacity of graphite, ca. 3860 versus 370 mAh g^{-1}, the lowest potential (−3.04 V vs standard hydrogen electrode), but a low density (0.534 g cm^{-3}).[3–5] Thereby, lithium metal, the “holy grail”, has been widely considered as the ultimate anode for the development of next-generation battery systems, such as lithium-insertion material, lithium–sulfur (2600 Wh kg^{-1}) and lithium–air (3500 Wh kg^{-1}) batteries.[6–8] Despite of these salient advantages, the practical commercialization of batteries comprising metallic lithium as the anode is hindered predominantly by 1) the dendritic lithium growth due to uneven Li^+ flux distribution; 2) the infinite volume changes upon Li stripping and plating; 3) the continuous destruction and reparation of solid electrolyte interphase (SEI) as a result of its unsatisfactory mechanical property and inhomogeneous thickness; and 4) the formation of “dead lithium” due to the root dissolution behavior (**Figure** 1a). These issues reduce the Coulombic efficiency (CE), shorten the cycle life, and impose potential safety hazard.

In the past decades, numerous efforts have been devoted to tackle the above-mentioned challenges, chiefly in the following five aspects: 1) constructing artificial SEI (ASEI) layers;[9–13] 2) introducing electrolyte additives;[14–17] 3) engineering modified separators;[18–20] 4) replacing liquid electrolytes with solid-state electrolytes;[6,21–26] and 5) designing 3D host current collectors (Figure 1b).[27–29] ASEI layers can facilitate uniform Li plating/stripping, but challenges remain in constructing robust ASEI with desired ionic/electronic conductivity. Electrolyte additives can form favorable interphases but may be consumed over long-term cycling. Modified separators generally enhance the safety property whilst at a cost of increased cell resistance that limits high-rate performance. Solid-state electrolytes have been recently investigated intensively because they can ideally enable dendrite suppression and allow for improved stability. Nevertheless, severe interfacial issues and relatively sluggish Li^+ kinetics are highly needed to be solved. In contrast, 3D current collectors offer unique advantages as hosts for Li metal anodes

---

X. Wang, Z. Chen, M. Chen
Key Laboratory of Engineering Dielectric and Applications (Ministry of Education)
School of Electrical and Electronic Engineering
Harbin University of Science and Technology
Harbin 150080, China
E-mail: chen.zhen@hrbust.edu.cn; mhchen@hrbust.edu.cn

K. Jiang
State Key Laboratory of Advanced Electromagnetic Engineering
School of Electrical and Electronic Engineering
Huazhong University of Science and Technology
Wuhan 430074, China

S. Passerini
Helmholtz Institute Ulm (HIU)
Helmholtzstrasse 11, D-89081 Ulm, Germany
E-mail: stefano.passerini@kit.edu

S. Passerini
Karlsruhe Institute of Technology (KIT)
P.O. Box 3640, D-76021 Karlsruhe, Germany

The ORCID identification number(s) for the author(s) of this article can be found under https://doi.org/10.1002/aenm.202304229

DOI: 10.1002/aenm.202304229

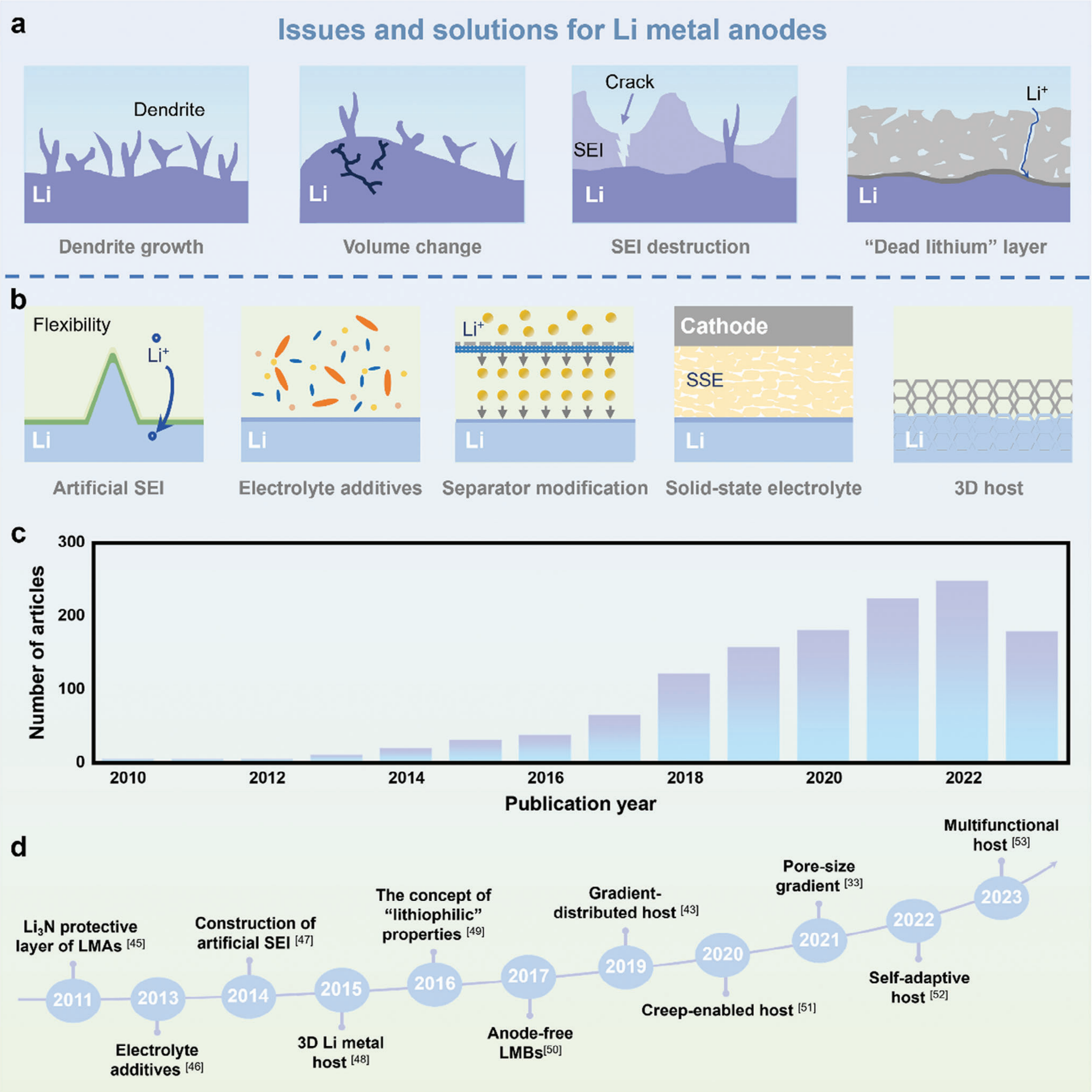

Figure 1. A summary of a) issues and b) solutions for LMAs. c) Number of publications on 3D LMA hosts from 2010 to 2023. d) A brief summary of the development of 3D LMA hosts.[33,49,54–62]

(LMAs). The high surface area allows for reduced effective current densities during charging and discharging to mitigate dendritic Li formation. The porous structure provides void space to accommodate Li deposit volume changes. Further, they enable sufficient electrolyte wetting for Li-ion flux while providing a mechanically robust framework. However, surface engineering is still needed to optimize interfacial properties between the 3D host and Li metal.[30] Generally, 3D current collector hosts can be categorized into five types, for example, metal-based hosts,[31,32] alloy-based hosts, carbon-based hosts,[33–35] composite hosts,[36–38] and dielectric-based hosts.[39,40] The conventional Cu, Ni-based, and carbon-based current collectors, nevertheless, suffer poor lithiophilicity with Li leading to high energy barrier for Li nucleation.[41] In this regard, decorating lithiophilic materials such as metals (i.e., Au,[42] Ag,[43] Zn,[44] and Mg[45]) and metal oxides (i.e., ZnO,[39] Al_2O_3,[46] and MgO[47]) among others, on 3D hosts is an effective strategy to improve the affinity between current collector and lithium.[48] However, such a design in general cannot guarantee the uniform Li deposition within the entire 3D structure, resulting from the preferential

Li nucleation and growth on top of the porous skeleton. The deposited Li further prevents the electrolyte, that is, the Li^+, from penetrating into the 3D host's inner space, failing to fully utilize the advantageous high porosity and surface area. Moreover, the thicker lithium deposition gradually weakens the positive impact of the decorated lithiophilic layer. This phenomenon is exacerbated when operating cells at high current densities and capacities, eventually leading to poor cycling stability and safety hazards. In response to the aforementioned remaining challenges, researchers have recently proposed various strategies guiding Li^+ deposition at the bottom of 3D hosts (namely, the "bottom–up" Li deposition), thus successfully confining the Li deposition within the 3D host architectures.[39,49,50] The development of design strategies for 3D LMA hosts is shown in Figure 1c,d.

This approach is also applicable to other alkali metal batteries. He et al.[51] introduced a 3D-printed Zn anode interspersed with layers of Ag nanoparticles that taper in concentration from bottom to top (3DP-BU@Zn). This structure facilitates ion migration toward the bottom. Similarly, Kwak et al.[52] constructed a 3D scaffold by stacking three mesh layers with incrementally varying Mg affinities. The arrangement of these layers progresses from magnesiophilic at the foundation to magnesiophobic at the top, giving rise to the 3D Mg affinity-controlled architecture (3D-MACA). This design is instrumental in directing Mg metal deposition toward the bottom, effectively mitigating the issue of top plating. Moreover, He et al.[53] designed a series of h-Ti_3C_2-based scaffolds endowed with a stepped sodiophilicity gradient (h-M-SSG). The pronounced sodiophilicity of h-Ti_3C_2 at the base is tailored to induce Na^+ deposition preferentially at the bottom of the anode, thus enhancing deposition uniformity and stability. These advancements reveal a promising strategy for enhancing the performance and longevity of alkali metal batteries through the structural engineering of their anodes.

In this review, we provide a comprehensive and systematic overview of the recent progresses of the various "bottom–up" design strategies, including advances in gradient host design and other less investigated methods. The former includes mainstream methods, such as the construction of electric conductivity gradient, lithiophilicity gradient, electron-ion dual gradient, and pore-size gradient. The less investigated methods include engineering doping/defects, building homogenized electric field, applying external magnetic field, and manipulating desirable SEI components. The in-depth mechanisms of lithium stripping-plating and various "bottom–up" strategies are also encompassed. Finally, remaining key challenges are outlined. It is anticipated that this review shall trigger more interesting works in the relevant field.

2. Mechanisms of Lithium Plating and Stripping

During cycling of a Li metal cell, metallic lithium is repeatedly plated and stripped on a given substrate. The lithium dendritic growth and infinite relative volume change generated at each cycle are the two critical challenges remaining to be tackled, which largely impede wide commercialization for practical applications. An in-depth understanding of the Li nucleation and growth mechanisms is essential to achieve long cycle lifespan and high safety. However, the Li nucleation and growth mechanism during Li metal electroplating is still not well understood. In this chapter, we overview the mainstream theories and mechanisms reported so far.

2.1. Li Nucleation

Based on the classical nucleation theory,[63] the Li nucleation initiates when decreasing the potential, accompanied by local composition fluctuation and energy fluctuation at the Li|electrolyte interface. The end of Li nucleation is reflected by the emergence of Li nuclei.[64] The overpotential for Li embryo nucleation (η_n) is defined as the magnitude of voltage spike occurring at the onset of Li deposition, while the overpotential for Li growth (η_p) is the extra voltage necessary to sustain the deposition and enlargement of lithium structures after the initial nuclei have formed. The difference between the growth overpotential and the nucleation overpotential ($\eta_p - \eta_n$) suggests the nucleation overpotential of substrates, indicating the relative ease with which Li can nucleate and grow on the substrate. (**Figure 2a**).[65,66] In an ideal condition, homogeneous nucleation can be realized. According to the classical equations of homogeneous nucleation,[67,68] one can correlate the size of electrodeposited Li nuclei with overpotential and applied current density. To form spherical nuclei with a radius r, the Gibbs energy ($\Delta G_{\text{nucleation}}$) can be formulated (Equation (1))[64] by the sum of its volume free energy ΔG_v and surface free energy Υ (Figure 2b):

$$\Delta G_{\text{nucleation}} = -4/3\pi r^3 \Delta G_v + 4\pi r^2 \gamma \qquad (1)$$

where ΔG_V (J m^{-3}) is the free energy change per volume and Υ (J m^{-2}) is the surface energy per area of the Li|electrolyte interface.

The correlation of ΔG_V and overpotential η is referred to Equation (2)[69]:

$$\Delta G_V = F\,|\eta|\,/\,V_m \qquad (2)$$

where F (96485 C mol^{-1}) is the Faraday's constant and V_m (m^3 mol^{-1}) is the molar volume of Li.

The critical radius (r_c) can be derived when the differential of the $\Delta G_{\text{nucleation}}$ becomes zero, as shown in Equation (3).[65] Notably, embryos with a radius larger than r_c will survive (and further grow) while the smaller ones will dissolve into the electrolyte.

$$r_c = 2\gamma/\Delta G_V = 2\gamma V_m/F\,|\eta_n| \qquad (3)$$

It is seen from Equation (3) that r_c is inversely proportional to η_n. The Li nuclei density N is, therefore, proportional to the cube of η_n ($N \approx \eta_n 3/r^3$, Figure 2c). This was verified experimentally by Pei et al.[65] who found that increasing the electrodeposition overpotential led to decreased nuclei size and increased nuclei number. According to the Butler–Volmer electrode kinetics, the overpotential is proportional to the current density.[70] Thus, one can tune the size of Li nuclei via manipulating the η_n as well as the current density i. Pei et al.[65] reported the sparsely located Li nuclei embryos at high current density while densely packed Li nuclei were observed at low current density (Figure 2d). Biswal et al.[66] proposed a theoretical formulation (Equation (4)) which

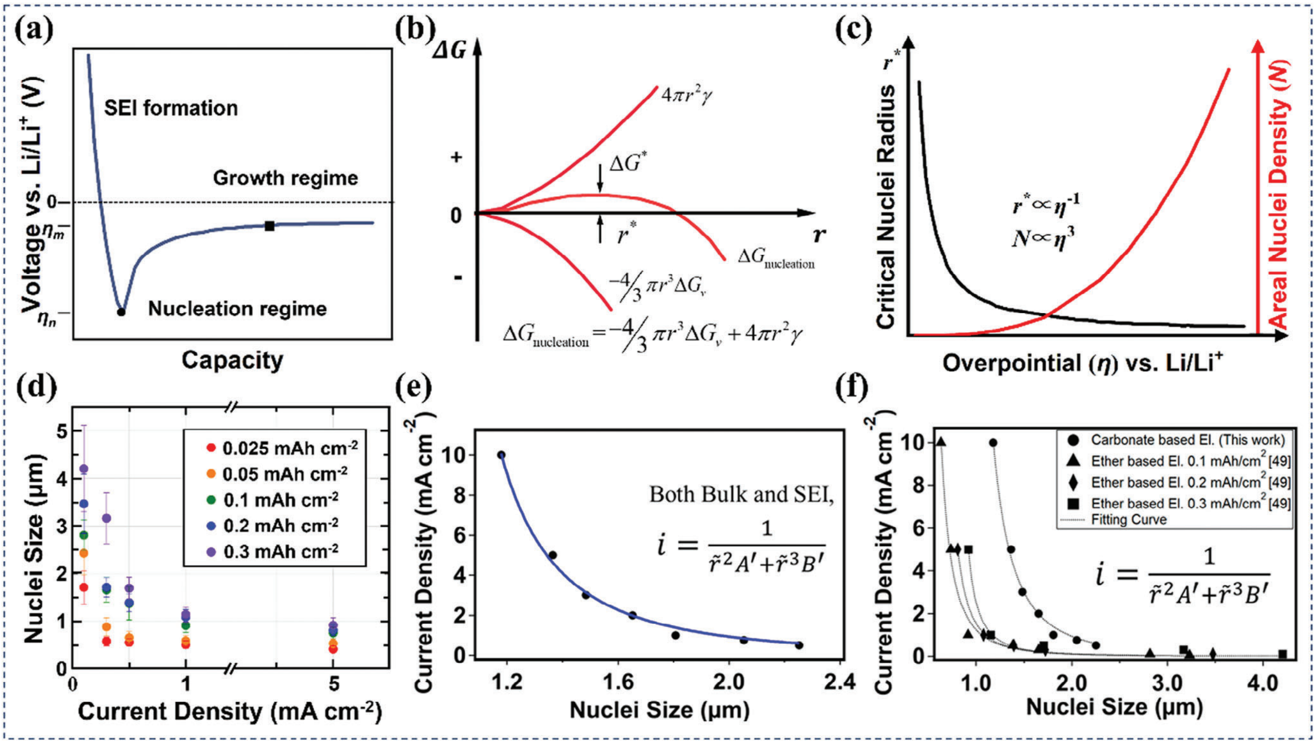

Figure 2. a) Schematic voltage versus capacity plot demonstrating the profile of galvanostatic Li deposition. Reproduced with permission.[66] Copyright 2019, American Chemical Society. b) Homogenous nucleation energy curve as a function of nuclei radius. Reproduced with permission.[64] Copyright 2021, American Chemical Society. c) Schematic plot of the dependence of critical Li nuclei radius and the areal nuclei density on the overpotential; d) Plot of Li nuclei size versus current density at various capacities. Reproduced with permission.[65] Copyright 2017, American Chemical Society. e,f) The dependency of average nuclei radius on current density involving the synergistic effects of bulk diffusion overpotential and SEI diffusion overpotential. Reproduced with permission.[66] Copyright 2019, American Chemical Society.

disclosed a square-cubic inverse dependency of average nuclei radius on current density (Figure 2e,f), indicating both bulk and surface ion diffusion overpotential synergistically contribute to the lithium electroplating.

$$i = 1/\left(\tilde{r}^2A' + \tilde{r}^3B'\right),$$

where

$$A' = RT/(2\gamma VD_BC_BF),\ and\ B' = RT/(\gamma VD_sC_sF) \tag{5}$$

where $\tilde{r}$ is the average nuclei radius, D_BC_B and D_SC_S are the bulk and surface ionic conductivity respectively, γ is the surface energy, V is the molar volume of metal, R is the universal gas constant, T is the temperature, and F is the Faraday constant, respectively.

In practical cases, heterogeneous lithium nucleation is often occurring instead of the above-mentioned homogeneous nucleation. Heterogeneous lithium nuclei are known to preferentially deposit on defect sites, such as impurities, grain boundaries, SEI cracks, etc. After nucleation initiates, there are three interfaces coexisting in the system, which are Li-electrolyte (*le*), substrate-electrolyte (*se*) and Li-substrate (*ls*) (**Figure 3**a). At the equilibrium state, the interface tension and contact angle can be expressed as Equation (6)[64,71]:

$$\gamma_{se} = \gamma_{ls} + \gamma_{le}cos\theta \tag{6}$$

The critical nucleation energy is expressed in Equation (7):[72]

$$\Delta G_c = 16\pi\gamma_{le}/3\Delta G_v{}^2\left(2 - 3cos\theta + cos\theta^3/4\right) \tag{7}$$

According to Equation (8), ΔG_c drops to zero when the contact angle θ is 0°, implying no nucleation barrier for Li electrodeposition. The angle θ is an important parameter which characterizes the lithiophilicity of substrates (Figure 3b,c). The difference between plating overpotential η_p and η_n, $\Delta\eta = (\eta_p - \eta_n)$, can partially reflect the lithiophilicity of substrates. The smaller value of $\Delta\eta$ is, the better lithiophilicity of a substrate is. Another indicator which reflects the lithiophilicity of substrate is the binding energy between lithium and substrate. A more negative binding energy indicates better lithiophilicity of substrate. Generally, a higher lattice mismatch between lithium and substrate leads to poorer lithiophilicity of substrate. Cu has the face-centred cubic (fcc) structure with an atomic radius of 1.28 Å, while Li has the body-centred cubic (bcc) structure with an atomic radius of 1.52 Å. Thus, Cu is commonly known as a poor lithiophilicity substrate (Figure 3d). Au has the same fcc structure as Cu, but, its atomic radius is larger (1.44 Å). Albeit the structure mismatch,

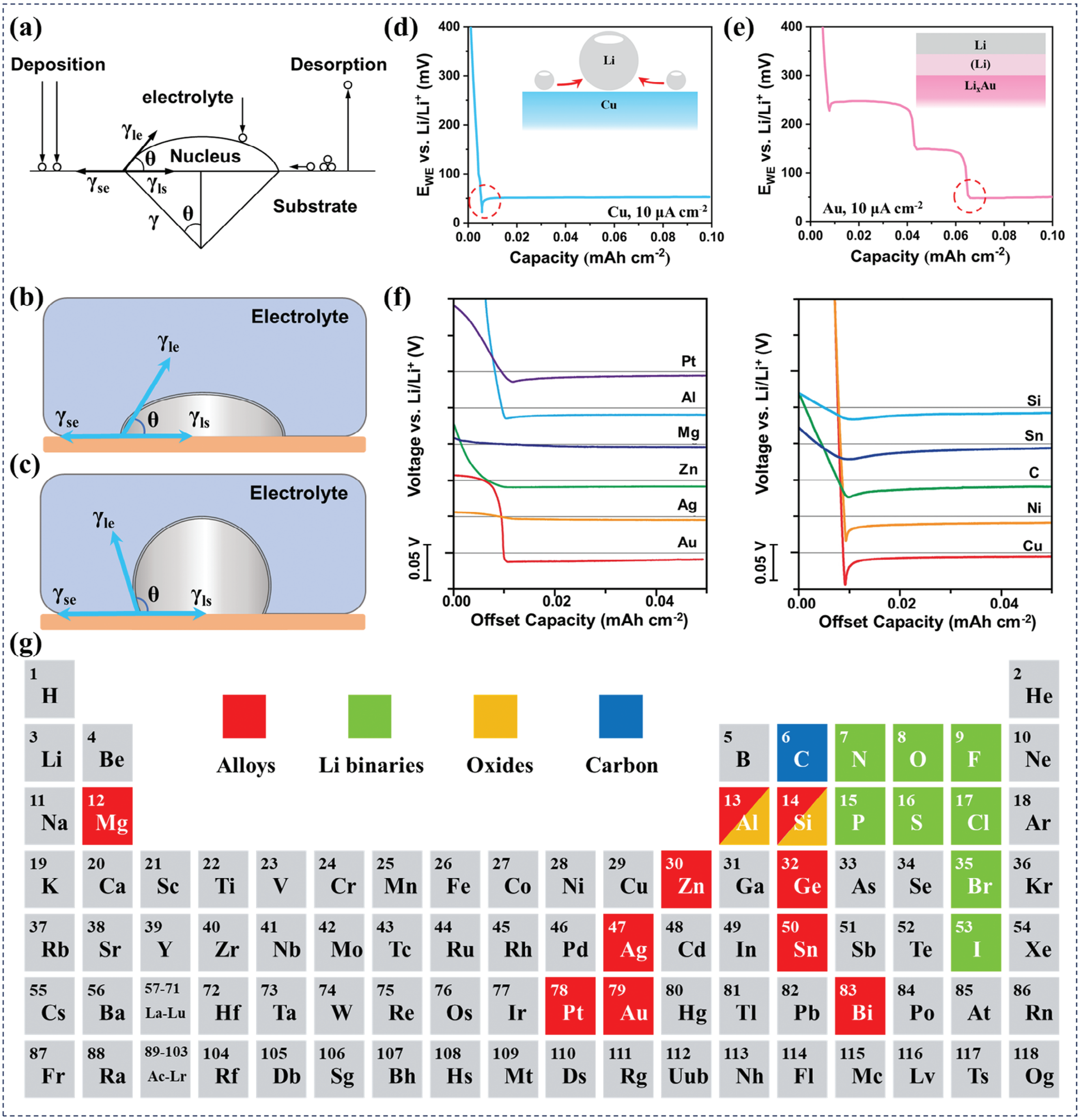

Figure 3. a) The scheme demonstrating the heterogeneous nucleation on substrate and relevant parameters. Young's angle and three surface forces when substrate exhibits b) high and c) low lithiophilicity. Reproduced with permission.[73] Copy right 2021, Royal Society of Chemistry. d–f) Overpotential during Li deposition on various substrates. Reproduced with permission.[41] Copyright 2016, Nature Portfolio. g) Elements enhancing the lithiophilicity of various substrate highlighted in the periodic table via alloy formation (red), binaries (green), artificial metal–oxide interphase (yellow), and intercalation reactions (blue). Reproduced with permission.[73] Copy right 2021, Royal Society of Chemistry.

Au shows negligible energy barrier for Li deposition. This is primarily due to the formation of Li$_x$Au alloy and the solid solution layer which exhibit high solubility and a similar lattice structure as the pure Li (Figure 3e).[41] Similar substrates which can alloy with Li are Ag, Mg, Al, Zn, Sn, Si, Ge, and Bi (Figure 3f,g).[73] Thus, one can tune the current collector's lithiophilicity via surface coating various materials which are capable of largely reducing the energy barrier for Li deposition.

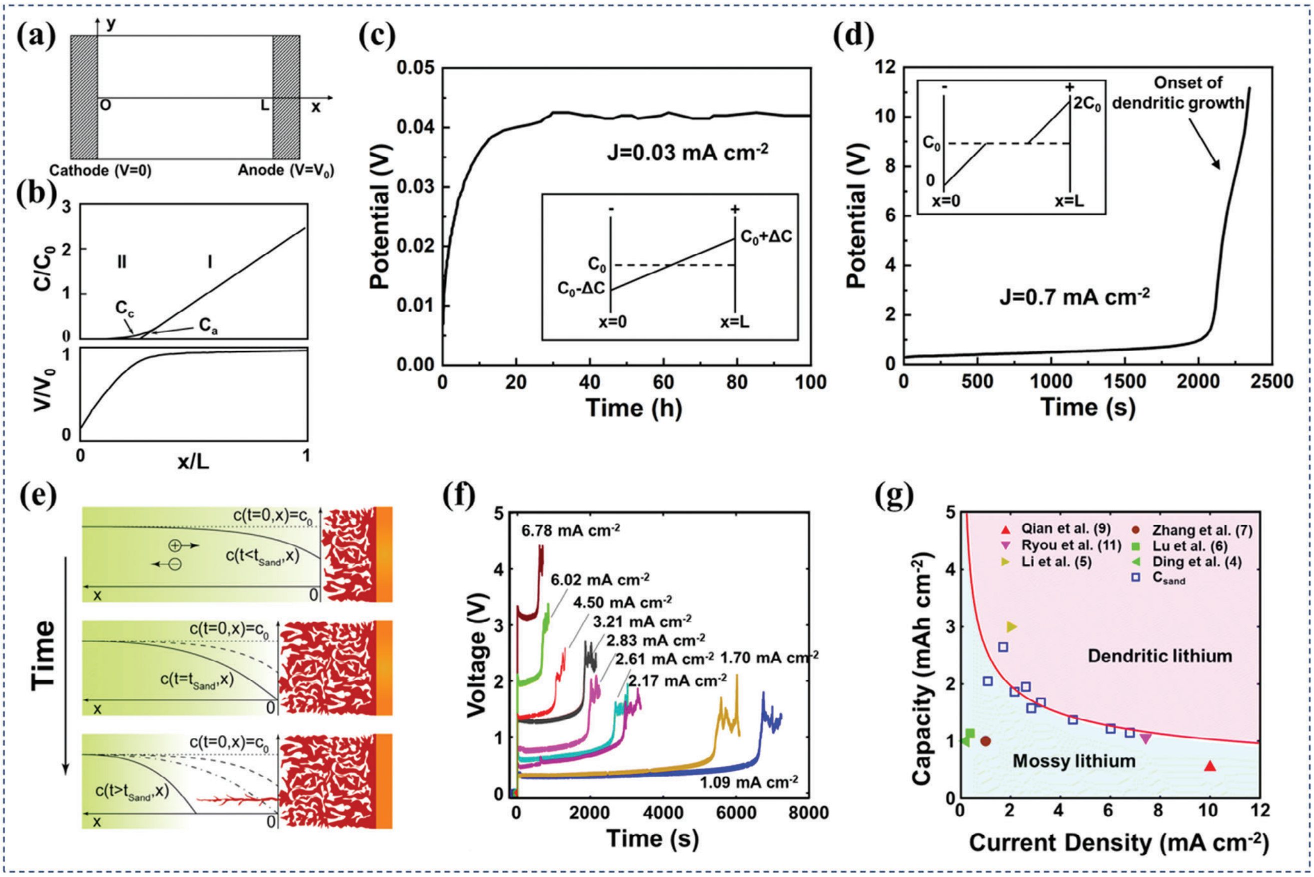

Figure 4. a) Schematic illustration of the cell; b) Profile of the ion concentrations C_c, and C_a, and electrostatic potential V resulting from the numerical simulation in the hypothetical case of uniform deposition with negligible growth of the cathode. Plots of potential versus time at c) a low current density ($J < J^*$) and d) a high current density ($J > J^*$). Reproduced with permission.[78] Copyright 1990, American Physical Society. e) Theoretical interpretation of the growth mechanisms of lithium electrodeposition during concentration polarization; f) Change of growth mechanism at Sand's time during concentration polarization; g) Current-dependent Sand's capacity with previous reports shown. Reproduced with permission.[82] Copyright 2016, Royal Society of Chemistry.

2.2. Dendritic Li Growth

The morphology of Li dendrites plays a pivotal role in influencing Li deposition behavior. The morphology varies significantly based on factors such as the type of electrolyte, current density, capacity, and the presence of impurities.[74] In ether-based electrolytes, Li deposition often takes an "island-like" form, while in carbonate-based electrolytes, it frequently appears as dendrites with various shapes.[65] For the sake of simplicity, these morphologies are broadly categorized into two types: "island-like" and dendritic, with the latter further being divided into "needle-like" and "moss-like" dendrites.[75] However, it's worth noting that "island-like" Li deposition is not as prevalent as its dendritic counterpart.[76]

Dendritic Li generates at high current density and over prolonged cycles. It is initiated by the relaxation of Li deposition-induced stress and the drain of Li$^+$ at the anode site. The dendrite growth usually follows a tip-growth pattern as a result of the high electric field and less concentration polarization at the tip site.[77] "Sand's time model" and "space charge model" are two famous and dominant theories for Li dendrite prediction. In 1990, Chazalviel[78] proposed the "space charge model" via disclosing the onset of ramified metallic copper growth from dilute binary electrolyte in a thin rectangular cell (**Figure 4a**). When polarizing the cell, cations and anions migrate in opposite directions under the force of the electric field. Approaching the cathode side, the ion motion is governed by diffusion (quasi-neutral region I, Figure 4b). Close to the anode side, the ion transport is driven by electric field migration (space charge region II, Figure 4b). At "Sand's time", t_{sand}, which was first reported by Sand in 1901,[79] the cations in the electrolyte are rapidly consumed, after which the concentration of cations in the vicinity of the electrode is expected to drop to 0 at some point, after which a strong negative electric field electrically absorbs and electrodeposits numerous lithium ions in a short period of time, thus inducing dendritic growth. The deposition velocity was revealed to be associated with the velocity of anions v_a and electric field in the neutral region of the electrolyte E_0.[80] The critical time for the initiation of Li dendrite is known as the "Sand's time" (Equation (8)),[79] where Z_c is the charge number of cation ($Z_c = 1$ for Li$^+$), D is the ambipolar diffusion coefficient, C_0 is the initial concentration of cations, J is the current density, and τ_a is the anion transference number.

$$t_{sand} = \pi D\left(Z_c F C_0\right)^2 / 4J^2 {\tau_a}^2 \tag{8}$$

In 1999, Brissot et al.[81] investigated the dendritic Li growth in symmetric Li|PEO-LiTFSI|Li cells, attempting to transfer the metal deposition from copper to lithium. After cell polarization, the ionic concentration gradient follows the formula as shown in Equation (9), where e is the elementary charge, μ_a and $\mu_{Li}{}^+$ are the mobilities of anion and Li$^+$, respectively. This study raised an important indicator, the limiting current density J^*. For a given inter electrode distance of L, J^* can be derived when dC/dx equals $2C_0/L$, thus J^* is formulated as Equation (11). Below the J^*, the system is at a steady state and the ion concentration from negative to positive electrode changes linearly (Figure 4c). However, when J exceeds J^*, the cation concentration reduces to zero at the negative electrode and the cell potential diverges at the Sand's time (Figure 4d).

$$\partial C/\partial x \ = \ J\mu_{\mathrm{a}}/eD\left(\mu_{\mathrm{a}} + \mu_{\mathrm{Li}}{}^{+}\right) \tag{9}$$

$$J^* = \ 2eC_0 D/C\tau_{\mathrm{a}} L,$$

where

$$\tau_{\mathrm{a}} = \mu_{\mathrm{a}}/\left(\mu_{\mathrm{a}} + \mu_{\mathrm{Li}}{}^{+}\right) \tag{11}$$

$$C_{\mathrm{sand}} = J_{t_{\mathrm{sand}}} \ = \ \pi D\left(Z_{\mathrm{c}} F C_0\right)^2/4J\tau_{\mathrm{a}}{}^2 \tag{12}$$

Bai et al.[82] measured the "experimental Sand's time" from the voltage–time plots at various current densities in a glass capillary cell using in situ snapshots (Figure 4e,f). The "Sand's capacity", C_{Sand}, was raised following a formula shown in Equation (12). The authors proposed two mechanisms of lithium growth in liquid electrolyte (Figure 4g). Below the C_{Sand}, reaction-limited mossy lithium forms and grows from the roots whereas above the C_{Sand}, transport-limit dendritic lithium grows from the tips. The latter causes potential cell short circuit and brings safety hazard.

3. Engineering 3D Hosts

The elucidation of processes governing Li metal nucleation and dendritic growth has underscored the pressing need for advanced strategies to address associated challenges limiting practical LMBs. Incorporating Li metal within 3D frameworks is proven an effective approach to minimize the substantial volume fluctuations and inhibit Li dendrite formation during prolonged cycling. Specifically, the porous structure of 3D scaffolds can readily accommodate Li metal volume changes and enable facile ion transport. With this context, the following sections will discuss methods to fabricate 3D LMA hosts and the application of different host materials.

3.1. Construction Methods of 3D Hosts

Various advanced fabrication techniques have been explored to construct 3D porous current collectors for LMAs, including electrostatic spinning, template methods, dealloying method and 3D printing.

3.1.1. Electrostatic Spinning

The nanofiber structures obtained through electrospinning possess high porosity and interconnected pores, which can serve as nucleation sites for uniform lithium deposition. Typically, polymer nanofibers are produced from their precursor solutions via electrospinning, and then converted to carbon or other lithium-compatible materials. The fiber diameter and porous structure can be tuned by controlling the solution properties and electrospinning parameters. The lithium deposition performance can be improved by introducing lithiophilic sites onto the nanofiber surfaces through further surface modification. The nucleation of Li on porous carbon nanofibers (CNFs) is further promoted because of the greatly reduced nucleation barrier. This helps address the issues caused by the large lattice mismatch between carbon materials and lithium metal, effectively suppressing lithium dendrite formation and growth. For example, Kim et al.[83] developed a 1D hollow carbon fiber (1D HCF) embedded with lithiophilic gold nanoparticles (Au NPs) via dual-nozzle electrospinning. The core solution contained a gold precursor and poly(methyl methacrylate) (PMMA), while the shell solution contained polyacrylonitrile (PAN). Following electrospinning and subsequent heat treatments, Au NPs were formed within the hollow carbon fiber cores (**Figure** 5a). The resulting nanostructured fibers enabled uniform Li deposition and suppressed dendrite growth, leading to improved battery cycling lifetime. Benefitting from the 3D porous structure and the introduction of lithiophilic sites, the electrospun nanofiber-based current collectors demonstrate superior performance in stabilizing the LMAs. While electrospinning nanofibers can be flexibly fabricated in batch processes with consistent pore sizes, their poor mechanical properties remain an issue. The expansions and contractions during cycling may degrade the nanoporous structures over time. This could lead to capacity fading or even mechanical fractures after prolonged stripping/plating, negatively impacting cell lifetime. Further research is needed to improve the mechanical integrity of electrospinning nanostructures without compromising other properties.

3.1.2. Template Method

Template-based approaches have been widely explored for fabricating 3D porous current collectors with tailored architectures. These methods utilize sacrificial template materials such as polystyrene microspheres, NaCl particles, or PMMA spheres to form porous structures. The template is first infiltrated with the current collector material, typically via electrodeposition, and then removed using solvents or etching to obtain the final 3D porous network. Tang et al.[84] fabricated a three-dimensionally ordered macroporous (3DOM) Cu current collector utilizing PMMA microspheres as the template (Figure 5b). Cu was electrodeposited on the PMMA template, which was constructed by aligning PMMA microspheres of around 450 nm diameter on a Cu wafer through electrophoresis. The subsequent removal of the template using acetone formed the porous Cu structure. This 3DOM configuration reduces local current density and accommodates volume changes during cycling, promoting uniform Li deposition and advancing anode electrochemical performance.

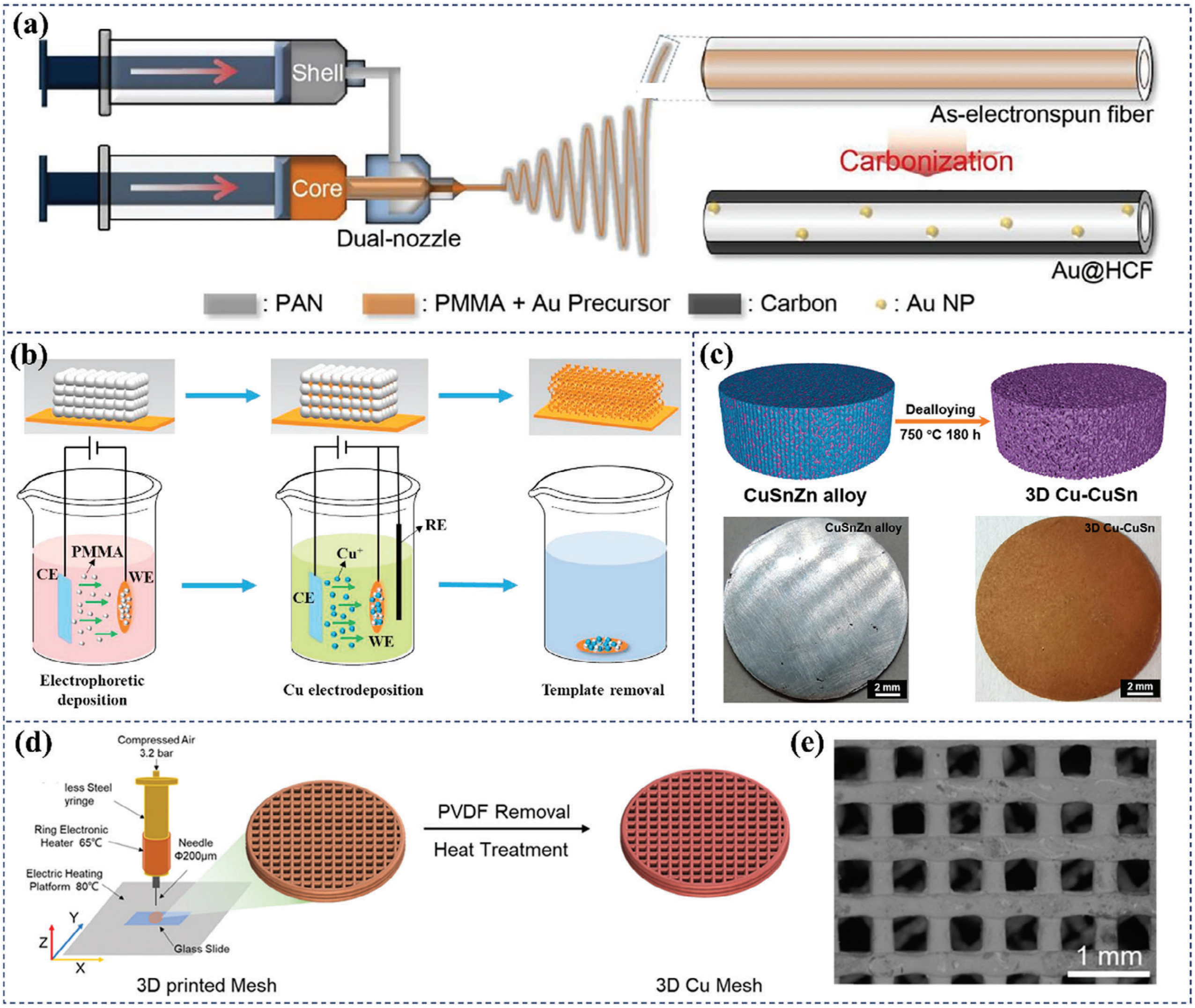

Figure 5. a) Experimental scheme for the electrospinning of Au@HCF. Reproduced with permission.[83] Copyright 2021, Elsevier. b) Schematic illustration of the fabricating process of 3DOM Cu. Reproduced with permission.[84] Copyright 2018, Elsevier. c) Schematic illustration of the preparation of 3D Cu-CuSn and corresponding digital photos. Reproduced with permission.[86] Copyright 2023, American Chemical Society. d) Schematic diagram of the 3D printing mechanism and postprocessing process of the Cu mesh; e) Morphology of the 3D Cu mesh. Reproduced with permission.[88] Copyright 2021, American Chemical Society.

Overall, while template-directed fabrication enables simple and scalable manufacturing of 3D current collectors, there remain barriers to widespread adoption. The sacrificial templates are single-use materials, presenting cost and sustainability challenges for large-scale industrialization. The fixed template sizes and shapes also limit flexibility in designing diverse pore configurations. Continued development of novel templating materials and current collector coatings will further enhance the versatility of this promising technique.

3.1.3. Dealloying Method

3D porous current collectors can be fabricated through dealloying, where active elements are selectively dissolved from a precursor alloy, forming a porous structure. For instance, Zhao et al.[85] reports an electrochemical etching method for Cu–Zinc (Zn) alloy to precisely engrave a 3D Cu structure with a uniform, smooth and compact porous network. This continuous 3D Cu structure has excellent mechanical properties and high electrical conductivity. The uniform and smooth pores with a large internal surface area ensure well dispersed current density for homogeneous Li deposition and accommodation. In the work by Li et al.,[86] a novel 3D Cu-CuSn current collector was fabricated via vapor phase dealloying from a Cu-Zn-Sn ternary alloy (Figure 5c). The higher vapor pressure of Zn facilitated its selective removal at 300–1500 K, leading to the formation of a microporous Cu-CuSn structure with a pore size in the range of 2–5 μm. The de-alloyed structure was subsequently infused with molten Li to create the 3D Cu-LiSn-Li composite electrode. The resultant composite electrode delivers enhanced cycling performance, lower overpotential, and exceptional rate capabilities at various temperatures, highlighting its potential for high-performance LMBs. In general, dealloying enables facile and scalable fabrication of 3D porous current collectors with tunable pore sizes and highly interconnected porous networks. However, many processes rely on harsh etching conditions involving high temperatures, strong acids, or corrosive salts to selectively leach alloying elements. There is also a risk of toxic fume emission during high-temperature vapor phase dealloying. With increasing shift toward sustainable manufacturing, environmentally benign dealloying techniques may enable clean, scalable production of 3D current collectors for high-performance batteries.

3.1.4. 3D Printing

3D printing has emerged as a promising technique to construct complex 3D current collectors for batteries. Various printing approaches have been explored, including extrusion-based, inkjet, and stereolithography techniques. These methods allow precise control over the 3D architecture at a microscale level, enabling designs that are not feasible with conventional fabrication. For example, Lim et al.[87] developed a novel extrusion-based direct ink writing method for the fabrication of three-dimensionally printed pure Cu frames for LMBs. Through the newly developed Cu precursor, crack-free bodies in mesh-like architectures with microchannels in the order of 100–300 µm can be obtained. Chen et al.[88] fabricated a conductive 3D Cu mesh for LMBs using a direct ink writing method. They extruded a viscous ink composed of copper powder, polyvinylidene difluoride (PVDF) binder, and methylpyrrolidone solvent through a fine nozzle onto a heated platform to create a grid with a high aspect ratio. Subsequent thermal processing removed the PVDF, enhancing conductivity, while a hydrogen atmosphere reduced the CuO (Figure 5d). The resulting mesh structure, with its interconnected filaments and uniform pores, improved current distribution and electrolyte flow, and mitigated lithium dendrite formation (Figure 5e). In general, 3D printing enables rapid prototyping and customizable designs to optimize properties like porosity, conductivity, and mechanical integrity. However, limitations remain in terms of print resolution, material options, and scalability. Further developments in multi-material printing and high-throughput techniques will make 3D printing a versatile tool for fabricating advanced 3D current collector architectures.

3.2. Types and Applications of 3D Host Materials

3.2.1. Metal-Based 3D Hosts

Metal-based materials, especially Ni and Cu, are the most common hosts for LMAs due to their high electronic conductivity, chemical stability, mechanical strength, and low cost. However, their planar and lithiophobic nature promotes Li dendrite growth. 3D metallic substrates (like metallic fibers and meshes) made by various methods increase surface area and mechanical stability. In particular, integration with lithiophilic materials as 3D hosts has been extensively explored. For instance, Chen et al.[89] fabricated a 3D composite anode (denoted as Li@CuM/Ag) through the application of magnetron sputtering to deposit a uniform layer of Ag on a Cu mesh substrate (**Figure 6a**). This surface engineering confers lithiophilic properties upon the Cu mesh. Upon depositing 5 mAh cm^{-2} of Li, the Li@CuM/Ag composite anode displays a smooth and dendrite-free lithium metal layer (Figure 6b). Nevertheless, the high mass density of metal hosts relative to lithium poses a key drawback for energy density. Further development of lightweight, porous metal hosts with high lithium loading capacity will be critical to enable the practical application of LMAs.

3.2.2. Alloy-Based 3D Hosts

Li alloy anodes present several advantageous properties as hosts for lithium metal, including rapid lithium diffusion, improved retention of structural integrity against volume changes, reduced local current densities, suppressed side reactions with electrolytes, and better air stability. Moreover, they can be readily fabricated under moderate conditions amenable to large-scale production. Li et al.[90] developed a novel alloy material for LMAs using a straightforward smelting-rolling technique. The fabrication process involved melting metallic lithium in a crucible and sequentially adding Al and Mg (AM-Li). The mixture was continuously stirred at high temperatures before being cooled and cast into blocks, which were then rolled into alloy strips (Figure 6c). The alloying process significantly improves the air stability of the LMA. The comparative air exposure tests between AM-Li alloy and bare Li show that the AM-Li alloy exhibits superior air resistance, maintaining its structural integrity and displaying considerably less oxidation (Figure 6d). However, the lower lithium content of alloys compared to pure lithium metal reduces the achievable energy density. Furthermore, dealloying processes during cycling may induce mechanical stresses and electrode pulverization after prolonged cycling. Overall, Li alloys are promising hosts that balance high capacity with capabilities to enable stable morphology and mitigated safety risks.

3.2.3. Carbon-Based 3D Hosts

Carbon-based hosts, particularly those made from carbon nanotubes (CNTs) or graphene,[91] can offer excellent electronic conductivity, high surface area for Li deposition, low weight, and reasonable cost. Furthermore, introducing lithiophilic functional groups on the surface of carbon can further guide uniform Li deposition. From an economic standpoint, Lu et al.[92] developed a nitrogen and phosphorus dual-doped carbon host material (NPCQP) using cost-effective quantitative filter paper as a precursor. The two-step fabrication process initiates with the pre-carbonization of filter paper at 500 °C under nitrogen atmosphere, a crucial step that purges the material of H and O elements to enhance the stability of the substrate. In the subsequent stage, the carbon matrix is enriched with nitrogen and phosphorus through liquid phase impregnation and vapor deposition techniques, culminating in the synthesis of NPCQP (Figure 6e). When paired with the commercial $LiFePO_4$ (LFP) cathode, the full cell with NPCQP@Li anode displays impressive long-term cycle stability and rate capability. However, carbon-based materials still struggle to completely avoid "dead lithium" formation caused by microscopic inhomogeneity after long-term cycling.

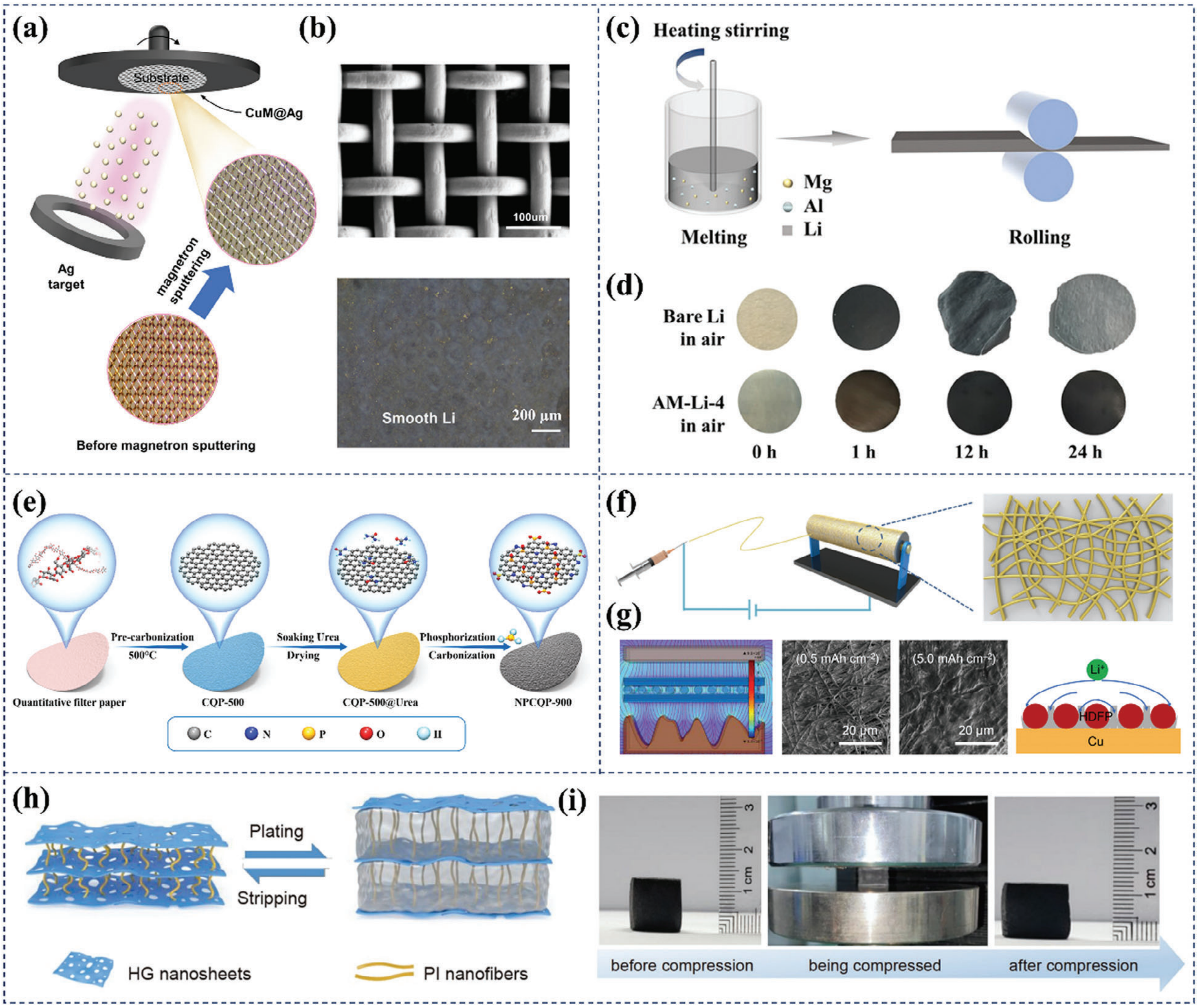

Figure 6. a) Schematic diagram of CuM/Ag prepared by magnetron sputtering; b) SEM images of the CuM/Ag before and after Li deposition. Reproduced with permission.[89] Copyright 2023, Wiley. c) Schematic illustration of the fabrication process for AM-Li anodes; d) Photographs of pristine Li and AM-Li-4 exposed to air with a relative humidity of 20% for various times. Reproduced with permission.[90] Copyright 2023, Wiley. e) Scheme illustration of the synthesis process of NPCQP.[92] Copyright 2023, Elsevier. f) Schematic diagrams of the Cu-HDFP framework; g) COMSOL simulation, SEM images, and schematic mechanism of Li deposition models on b-Cu-HDFP surface. Reproduced with permission.[93] Copyright 2023, Springer. h) Schematic illustrating the Li plating and stripping behavior in the hosts of the PI-HGCA framework; i) Sequential compression-recovery test of PI-HGCA. Reproduced with permission.[94] Copyright 2023, Springer.

Besides, they generally show relatively low mechanical strength and cannot effectively withstand the stress induced by the volume change of Li. Therefore, future research needs to continue optimizing the composition and structure of carbon-based materials, and combine them with mechanically robust materials to further improve their mechanical properties. In summary, while suitably designed carbon-based materials can serve as effective supports for lithium metal anodes, addressing the challenges in regard to the long-term cycling stability remains an ongoing endeavor.

3.2.4. Dielectric-Based 3D Hosts

Employing dielectric polymers as 3D hosts is a promising strategy to induce uniform lithium plating in a “bottom–up” manner. The polar groups in electrically nonconductive polymers can effectively regulate Li^+ distribution, forcing the ions to deposit only on existing lithium metal or the conductive current collector. This reduces ion concentration gradients and prevents uneven plating. Moreover, the polymer’s flexibility accommodates volume changes well. Kang et al.[93] developed a technique using electrospinning to create high dielectric functional polymer (HDFP) nanofibers embedded with C–F groups on bare Cu substrates (b-Cu-HDFP) (Figure 6f). The HDFP nanofiber layer provides abundant deposition sites and enables Li^+ flux due to the presence of strong dipoles along its fibers. Moreover, the high lithiophilicity of the HDFP nanofiber layer helps even out the irregular local Li^+ concentration accumulating on the b-Cu-HDFP surface by spreading out Li^+ pathways along the polar HDFP fibers. This leads to a lower nucleation overpotential and more uniform Li deposition (Figure 6g). The scalability of the electrospinning process is demonstrated by the successful production of electrode layers as large as A4 paper size (>600 cm^2). However, there are challenges in practical application. The polymer host must be coupled with a conductive substrate for the anode, but weak binding between the nonconductive polymer and substrate impacts the stability. The polymer may detach from the substrate when infiltrated with electrolyte. Furthermore, the interface impedance between substrate and polymer host is a concern. Overall, dielectric polymers are advantageous due to their low cost and tunable properties, but their interface stability and ionic conductivity must be optimized.

3.2.5. Composite-Based 3D Hosts

While 3D porous architectures have demonstrated promise in research for high-capacity LMAs, their complexity and lack of scalability remain a key barrier for commercialization. Regarding practical application potential, metal- and alloy-based hosts may be more suitable for high-power applications owing to their high electronic conductivity and mechanical strength. Carbon-based hosts could be more appropriate for lightweight or cost-sensitive applications. Dielectric hosts might exhibit greater applicability in high-temperature environments given their high thermal stability. Composites, formed by combining two or more materials, can provide a balance of properties that shall be advantageous for LMA hosts. For example, composites of a carbon and a metal or an alloy may offer favorable electronic and Li-ion conductivity, improved mechanical strength, and reasonable cost. Feng et al.[94] developed a 3D composite comprising polyimide (PI) nanofibers interlocked with holey graphene (HG) nanosheets as a hierarchical porous host (PI-HGCA) for LMAs (Figure 6h). The PI nanofibers act as supporting pillars between the layered HG nanosheets, imparting exceptional mechanical resilience against volume fluctuations during battery cycling. Therefore, the hierarchically porous architecture of PI-HGCA could be completely restored without any mechanical fracture during sequential compression-recovery tests (Figure 6i). This reveals the significance of the synergistic design with PI nanofibers to achieve self-adapting compressibility. Moreover, composite hosts could offer the most versatility, with composition tailored to specific applications. Notably, the optimal 3D host material is highly dependent on the intended battery application and associated performance requirements. Therefore, ongoing research and development are crucial to optimize these materials according to their targeted usages.

3.3. Tortuosity Effects in Lithium-Metal Host Anodes

In the development of gradient designs for 3D current collectors, the factor of tortuosity plays a crucial role in affecting Li deposition. Chen et al.[95] reported that electrodes composed of horizontally aligned reduced graphene oxide (rGO) exhibit a high degree of tortuosity (up to 4.46) which results in elongated and convoluted paths for Li$^+$ transport. Such a configuration promotes preferential Li deposition and stripping at the upper layer of electrode where ion transport is less restricted. During stripping, the high tortuosity enhances localized current density, fostering the formation of "dead Li" and additional SEI layers at the surface. This reduces the reversibility of the anode and blocks ion channels, leading to accelerated anode failure. Conversely, they found that electrodes with vertically aligned rGO channels with the lowest tortuosity of 1.25, enable more uniform Li$^+$ transport and deposition. This structure ensures direct ion paths, distributing lithium evenly across the electrode and preventing the blockage of ion-transport channels. Consequently, this low-tortuosity arrangement sustains homogenous current density during cycling and reduces the emergence of "dead Li" and SEI, ultimately enhancing the structural integrity and electrochemical reversibility. Moreover, randomly arranged rGO presents an intermediate tortuosity of 1.76, suggesting a balance between directness and length of ion pathway. Therefore, when designing 3D current collectors for LMBs, it is preferable to aim for a structure with low tortuosity. Wu et al.[96] developed a composite LMA supported by lithiophilic and low-tortuosity TiO_2/polyvinyl pyrrolidone (PVP) nanofibers using a simple rolling method. The vertically aligned TiO_2/PVP nanofibers provide a low-resistance path for Li$^+$, promoting uniform Li deposition during charging cycles. The micrometer-scale spaces between the TiO_2/PVP fibers accommodate the substantial volume changes associated with Li plating and stripping without structural collapse, thereby ensuring stable cycling. Zhang et al.[97] introduced a novel 3D current collector for LMBs, made from carbonized wood (C-wood) with vertically aligned channels. These straight channels minimize tortuosity and enhance ion transport. C-wood coated with zinc oxide enables rapid and uniform Li infusion, thereby improving charge efficiency and reducing dendrite growth. This leads to better stability and cycle life, showcasing the synergy between natural structures and advanced battery technology. In conclusion, the 3D structure with vertically aligned channels exhibits low tortuosity, which theoretically facilitates more uniform Li$^+$ transport and deposition. However, the design of 3D hosts necessitates comprehensive consideration of the specific characteristics of the collector materials, including their properties, porosity, and tortuosity. Therefore, the selection and design of 3D host should be a customized process that thoroughly considers material properties and battery requirements.

3.4. Necessity for "Bottom–Up" Lithium Deposition

The construction of 3D hosts possessing large specific surface areas not only reduces the local current density and suppresses the Li dendrites, but moreover provides space for volume changes over repeated Li stripping and plating avoiding for the volume change of the whole cell upon discharge and charge. Ideally, for preventing the dendritic and " dead lithium" growth, it is prerequisite to uniformly confine the Li within 3D host frameworks. However, single conductive or dielectric hosts are generally insufficient for the uniform lithium deposition owing to their inherent shortcomings. For electrical conductor host, after electrolyte wetting, the entire 3D framework turns to be an equipotential conductor, therefore, Li is preferentially deposited on top of the conductive host (called "top deposition") because of the predominantly vertical electric field and shorter ion diffusion pathways.[98] Research by Li et al.[37] demonstrates that unmodified CNFs exhibit highly non-uniform Li deposition, characterized by significant agglomeration both within the host matrix and on its surface, indicating suboptimal electroplating efficiency. Complementary findings by Jiang et al.,[99] employing in situ optical microscope to observe the Li deposition process, revealed the formation of pronounced Li dendrites and a near-doubling in volume of a carbon fiber cloth (CFC) electrode, highlighting the substantiality of top-focused deposition. Furthermore, Zhang et al.[47] confirmed that Li plating on Cu meshes predominantly occurs in the top region, reinforcing the notion of "top deposition" preference. Crucially, the incidence and severity of these deposition anomalies are amplified at elevated current densities, suggesting that uniform deposition remains a challenge under high-rate electroplating conditions.

On the other hand, given the fact that the dielectric 3D hosts can not transfer electrons through the framework, thus, only quite limited electrochemical-active area (contact points with metal substrate such as Cu, stainless steel etc.) is accessible for the Li deposition/dissolution process.[100,101] In this case, the lithium growth follows the "bottom deposition". Li et al.[102] provided an empirical evidence for this phenomenon. They not only observed the preferential aggregation of Li metal on the top surface within a conductive sponge, leading to dendritic growth but also identified a significant shift in deposition behavior in the dielectric counterpart. After Li deposition, the bottom of the current collector becomes a primary site for lithium accumulation, with substantial dendritic and filamentous growth observed within the pores of the dielectric sponge. This drawback greatly influences the cell performance at high current densities.

To circumvent the limitations of both "top deposition" and "bottom deposition", strategies which allow the "bottom–up" lithium deposition even under conditions of high current densities and high areal capacities are highly needed.

3.5. Principles Behind the "Bottom–Up" Lithium Deposition

By far, many design strategies have been reported to realize the "bottom–up" lithium deposition within 3D hosts. Constructing gradient architecture is widely studied, including electrical conductivity gradient, lithiophilicity gradient, electron-ion dual conductivity gradient and pore-size gradient. Some other methods such as introducing doping/defects, building homogenized electric field, applying external magnetic field, and manipulating desirable SEI components, are also effective but are relatively less investigated. In this section, the principles behind the "bottom–up" lithium deposition of each method are concisely discussed.

3.5.1. Electrical Conductivity Gradient

The construction of electrical conductivity gradient which gradually increases from top to bottom provides a potential gradient distribution of the 3D framework. Therefore, electrons are more easily available at the bottom part of the 3D framework, which offers more preferred Li deposition and dissolution sites with respect to the top region. Consequently, constructing an electrical conductivity gradient is regarded as a feasible method to guide the "bottom–up" Li deposition.

3.5.2. Lithiophilicity Gradient

In constructing 3D hosts for LMAs, a lithiophilicity gradient is strategically developed by choosing materials with strong lithiophilic properties at the bottom, which favor Li^+ attachment due to their lower nucleation barriers and more negative lithium binding energy. This creates a directed pathway for Li^+ to deposit preferentially at the bottom of the host structure. In contrast, the top region of the host is designed with lithiophobic materials, which present a high nucleation barrier, deterring lithium accumulation and deposition at the surface.

The incorporation of a lithiophilicity gradient within the 3D host structure not only guides the preferential "bottom–up" Li deposition but also significantly influences the ion conductivity within the LMA. By directing the Li^+ toward sites of high lithiophilicity, ion migration is facilitated through the host, promoting uniform deposition and enhancing ion conductivity. This approach ensures that Li^+ is deposited in a controlled manner, reducing the risk of dendrite formation and improving the overall safety and longevity of the LMA.

3.5.3. Electron-Ion Dual Conductivity Gradient

Constructing electron-ion dual conductivity gradient requires the selection of two or more materials which display a trend of increased electric conductivity and lithiophilicity from top to bottom. This strategy synergistically utilizes the advantages of electron conductivity gradient and lithiophilicity gradient, which can more effectively guide the "bottom–up" Li deposition and suppress the growth of dendritic Li.

3.5.4. Pore-Size Gradient

Constructing a pore-size gradient entails designing an anode where the size of the pores gradually decreases along the depth direction. This results in higher porosity close to the top surface, with smaller and denser pore structures toward the bottom. The gradient can be achieved by one-step synthesis using pore-forming agents with different particle sizes or by layering materials with distinct pore sizes. In such a pore-size gradient framework, the larger pores at the surface aid in better electrolyte permeation, thereby reducing the concentration gradient of Li^+ within the electrolyte and ensuring a more uniform distribution of Li^+ across the entire structure. In addition, as the pore size decreases, the specific surface area per unit volume increases, resulting in a decrease in charge transfer resistance at the bottom. Consequently, Li is more likely to deposit at the bottom and then progressively fills the space upward, achieving a "bottom–up" Li deposition.

3.5.5. Doping/Defects

The lithiophilicity gradient plays a crucial role in the deposition of lithium metal on a 3D current collector. However, abrupt lithiophobic–lithiophilic interfaces can lead to stress accumulation and fatigue failure. To mitigate this issue, introducing doping or defect engineering throughout the structure can increase its lithiophilic properties by creating additional active sites for lithium-ion binding. These active sites possess a higher affinity for lithium ions, which can also improve the material's electrical conductivity. Guiding Li^+ transport to the bottom for "bottom–up" lithium deposition in combination with the metal foil at the bottom could be an effective strategy.

3.5.6. Homogenized Electric Field

Homogenized electric fields refer to building a uniform distribution of electric fields within an electrode material, which can be achieved through various strategies such as modifying the scaffold structure or using high dielectric materials, which can lead to a reduced local electrical field gradient in the vicinity of the Li metal deposition region, homogenized E-field distribution in the whole LMA preventing preferential nucleation and growth of Li dendrites, thereby improving the stability and safety of LMAs.

3.5.7. External Magnetic Field

Applying an external magnetic field is a method of introducing a magnetic field to enhance the deposition of Li in LMBs. The magnetic field generates magnetohydrodynamic effects, resulting in circular motion in the electrolyte surrounding the current collector, promoting enhanced mass transfer and ultimately facilitating the deposition of Li^+ within the substrate. This approach enables the 3D structure of the current collector to accommodate deep lithium deposition, effectively preventing dendrite formation and improving battery performance.

3.5.8. SEI Components

Modifying the 3D framework with functional materials such as LiF and Li_3N can guide homogeneous lithium deposition and relieve volume expansion during cycling. LiF has a lower energy barrier for surface diffusion of Li-ions and can suppress dendritic Li growth, while Li_3N has high ionic conductivity and low electronic conductivity, making it effective in stabilizing the interface and promoting dendrite-free Li deposition. Both LiF and Li_3N can be uniformly incorporated onto 3D frameworks to promote homogeneous Li deposition and reduce volume expansion during cycling.

4. Strategies Enabling "Bottom–Up" Lithium Deposition

4.1. Advances in Gradient Host Design

Gradient design can be used to address the issue of Li dendrite growth in LMAs by constructing a composite anode with a gradient structure to guide "bottom–up" lithium deposition. This can be achieved by adjusting lithiophilicity or conductivity in perpendicular to the anode/separator interface, or by designing a pore size structure that gradually increases along the side away from the separator toward the side near the separator.

4.1.1. Constructing Conductivity Gradient

The electric field distribution is crucial for regulating Li deposition, and a gradient framework with increasing electronic conductivity can guide Li-ions to deposit from the bottom and grow upward. Conductivity gradient hosts can either be free-standing LMAs or be integrated on Cu foils, and their conductivity gradually decreases from bottom to top. More electrons are concentrated at the bottom of these hosts due to the conductivity differences along the vertical direction, promoting preferential Li deposition at the bottom region.

Generally, the 3D frameworks can be divided into electrically conductive frameworks (e.g., carbon-based frameworks[103,104] and metallic frameworks[57,105–107]) and dielectric frameworks (such as glass fiber mat[108]). Li metal tends to deposit on the top part of conductive frameworks due to the concentrated electric field and shorter Li^+ ions diffusion pathways from the cathode. As for the dielectric 3D frameworks, the electrochemical process cannot take place in most areas of dielectric frameworks due to their inability to support electron transport, failing to utilize the porous structure within the 3D hosts. Li et al.[102] created a conductive-dielectric gradient (CDG) host by coating the melamine sponge with Ni nanolayer that increases in thickness from top to bottom, generating a vertically increased local electric conductivity gradient (**Figure 7**a). The electrically conductive part at the bottom serves as electroactive sites for Li nucleation, together with the assist of top dielectric layer, guiding the Li metal to grow upward. This was verified by the cross-sectional scanning electron microscopy (SEM) images. The CDG structure allows for constant "bottom–up" Li metal deposition up to 8.0 mAh cm^{-2}, more importantly, without Li dendrite formation (Figure 7b).

Structured anodes often utilize carbon-based LMAs as a material of choice owing to the favorable characteristics such as lightweight, good electrical conductivity, chemical stability, and exceptional mechanical properties, which can largely elevate the energy density comparing to the heavy metal-based LMAs. As evident in Figure 7c, Hong et al.[109] used a multistep vacuum infiltration method to design a trilayer electric conductivity gradient (CG) host consisting of a top insulating layer (CNF+SiO_2), a moderately conductive middle layer (CuNW+CNF), and a highly conductive bottom layer (CuNW). According to simulation results from COMSOL Multiphysics, the concentration of Li^+ flux in the local reaction is higher in the bottom layer due to electron sequestration occurring in the top layer (Figure 7d). Li deposition on the highly conductive bottom layer is ideally favored, whereas the Li deposition on the insulating top layer is impeded. Consequently, such a structure allows for stable Li plating and stripping behavior at a current density of 0.5 mA cm^{-2} with a promising CE greater than 96% for 120 cycles (Figure 7e). Zhou et al.[8] developed a $LiNO_3$-modified conductivity gradient host (LNO-CGH) composed of four layers (Figure 7f) which include, from top to bottom, a PAN dielectric layer containing excess $LiNO_3$ particles, and three layers consisting of CNF membranes with increased concentration of CNTs (i.e., CNF, 5CCNF, and 10CCNF), achieving a upward decreased conductivity gradient that controls the migration of Li^+ to the bottom layer. This "bottom–up" Li deposition manner of Li-ions during the diffusion process has been demonstrated through COMSOL simulation results, from which

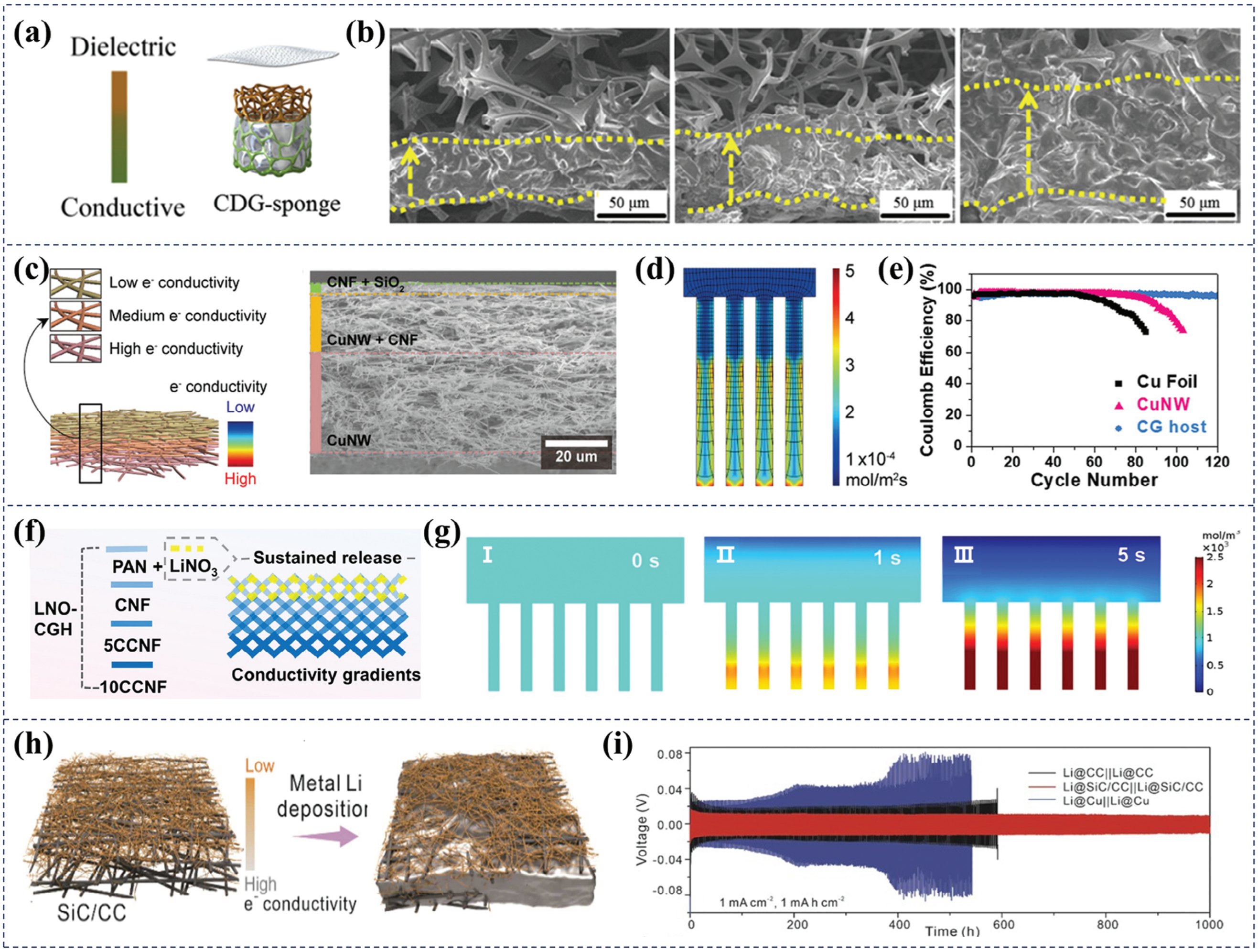

Figure 7. a) Schematic illustration of Li metal deposition behavior in CDG-sponge: "bottom–up" deposition without dendrite formation; b) Cross-sectional SEM images of the CDG-sponge after depositing 2, 5, and 8 mAh cm^{-2} of Li at 1 mA cm^{-2}. Reproduced with permission.[102] Copyright 2019, Elsevier. c) Schematic diagram and cross-sectional SEM image of a CG host; d) A scheme showing Li-ion reaction flux during the lithiation process on the CG host with the aid of COMSOL Multiphysics; e) Comparison of CE for Li||Li@host asymmetric cells. Reproduced with permission.[109] Copyright 2020, Wiley. f) Schematic illustration of LNO-CGH; g) The corresponding Li$^+$ concentration field simulation after I) 0 s, II) 1 s and III) 5 s. Reproduced with permission.[8] Copyright 2022, Elsevier. h) Schematic diagrams of the Li@SiC/CC framework before and after Li deposition; i) Lithium stripping-plating profiles of various electrodes in symmetrical cells at 1 mA cm^{-2}, 1 mAh cm^{-2}. Reproduced with permission.[46] Copyright 2022, Elsevier.

it is clearly seen that Li-ions are concentrated at the bottom layer (Figure 7g). As a film-forming agent, LiNO$_3$ is rarely used directly in carbonate electrolytes due to its extremely low solubility (<800 ppm). However, this design allows for the continuous release of LiNO$_3$ from the top layer, forming a firm nitride-rich SEI layer even in carbonate electrolytes that improves the interfacial and thermodynamic stabilities of LMA. Despite a harsh condition with an N/P ratio of 4, the LNO-CGH@Li||LiNi$_{1/3}$Co$_{1/3}$Mn$_{1/3}$O$_2$ (NCM111) cell exhibits an exceptional capacity retention (74.9%) over 120 cycles and a higher overall CE (99.9%) compared to the Cu@Li||NCM111 cell (7.3% and 98.7%, respectively). Recently, Sun and co-workers[46] created a host consisting of gradient-distributed SiC whiskers on a carbon cloth (SiC/CC). The SiC was obtained via a gas–solid reaction between gaseous SiO and CNFs, which demonstrates greatly simplified preparation process of LMAs (Figure 7h). The COMSOL simulations indicate that the SiC networks effectively decrease the electric field intensity in the upper region and form a Li-ion concentration gradient, leading to homogeneous and "bottom–up" Li metal deposition within the SiC/CC framework. Accordingly, as revealed in Figure 7i, the constructed symmetric cell with Li@SiC/CC electrode exhibits a low overpotential (ca., <20 mV) and a long lifespan (ca., 1000 h, 1 mA cm^{-2}).

3D framework constructed with lithiophilic metals which combine both the merits of metallic materials and lithiophilic materials is deemed as a promising candidate that is expected to stabilize the Li anode. As reported, Li-rich alloys usually exhibit small nucleation barrier.[110] Adopting a facile one-step vacuum evaporation method, Liu et al.[42] prepared a Li-rich Li-In anode on a Cu foil. The In$_3$Li$_{13}$ framework is designed to guide uniform lithium deposition and inhibit dendrite growth (**Figure 8**a). The thickness of the re-plated Li-In anode is about 15 μm, and some unfilled lacuna is observed on the top region. This indicates that lithium tends to deposit from the bottom rather than the

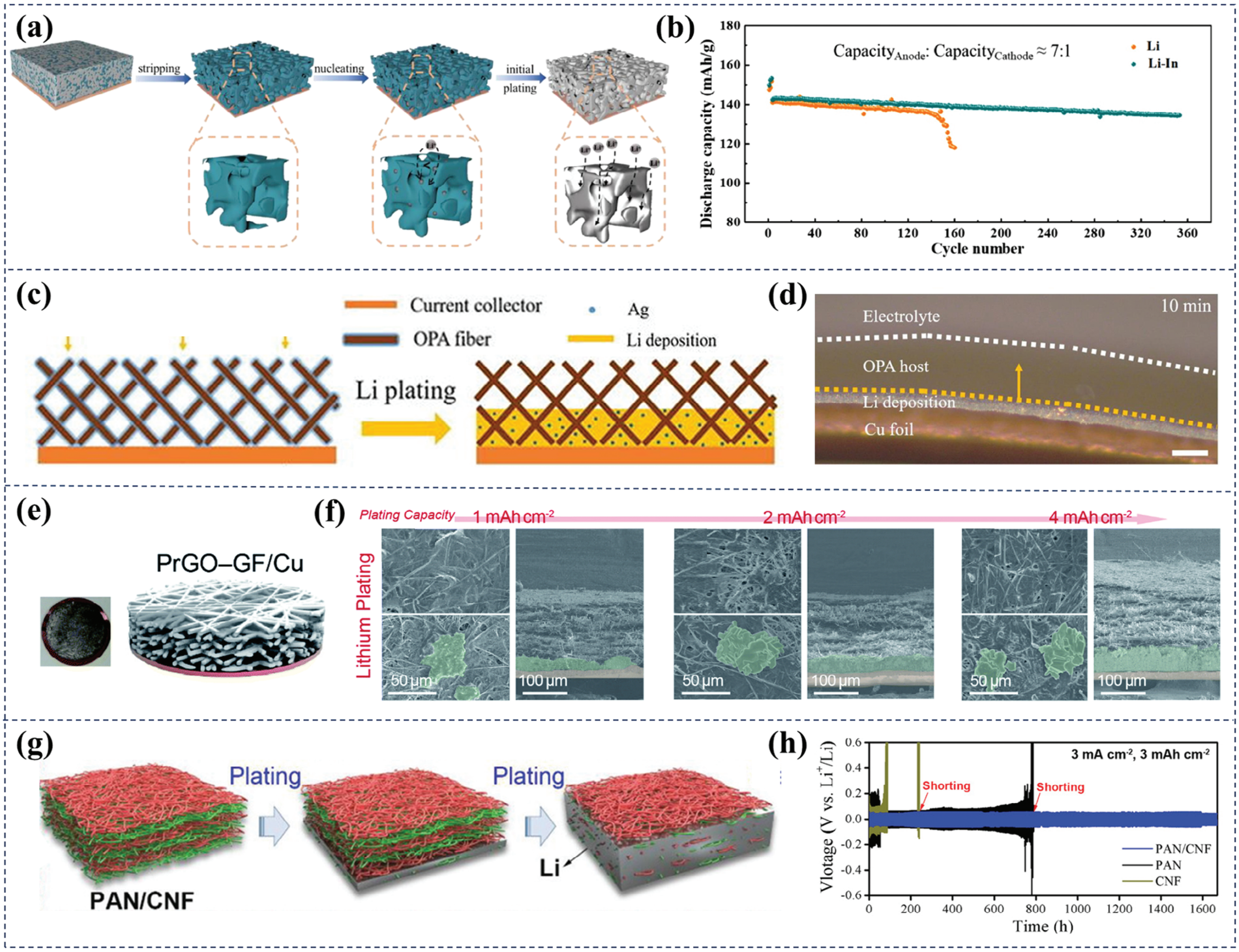

Figure 8. a) Schematic illustration of Li stripping/plating behavior on integrated Li-rich Li-In anode; b) Cycling performance of full cells with Li or Li-In anode (cycling at 1 C after 3 activation cycles at 0.1 C). Reproduced with permission.[42] Copyright 2020, Elsevier. c) Schematic illustration of the synthetic procedure of C-Ag/PVDF; d) In situ optical observation of Li deposition in the OPA framework at a current density of 4 mA cm^{-2}. Reproduced with permission.[44] Copyright 2020, Elsevier. e) Scheme of the phosphidation reaction of CuNWs; f) SEM images of the Li plating behavior on CuNW-P current collectors. Reproduced with permission.[113] Copyright 2021, Royal Society of Chemistry. g) Scheme of Li plating on PAN/CNF; h) Lithium stripping-plating profiles of different LMAs at a current density of 3 mA cm^{-2} with a plating capacity of 3 mAh cm^{-2}. Reproduced with permission.[115] Copyright 2020, Wiley.

top surface of the frame, which is related to the approximately 5 times higher resistivity of In metal than that of the Cu metal at 20 °C. When revealed in a Li-In||LFP cell with only 3.8 mAh cm^{-2} of lithium content and an N/P ratio of 7, a high discharge capacity of 137.3 mAh g^{-1} over 350 cycles at 1 C can still be retained (Figure 8b).

A nonconductive dielectric layer can also be used to guide gradient Li deposition by constructing it on top of a Cu foil. In this regard, several 3D substrates with lithiophilic functional groups, such as nitrogen-doped graphitic carbon foams[43,111] and graphitic carbon nitride,[112] have been developed. Ran et al.[44] developed a 3D insulating framework composed of oxidized PAN fibers interweaved into a 3D skeleton structure and decorated with uniformly distributed Ag nanoparticles (OPA) (Figure 8c). The insulating nature of PAN facilitates Li$^+$ transport and its oxidized surface provides polar functional groups to accelerate Li$^+$ absorption. Since electrons can only be provided from the bottom Cu current collector, the insulating PAN framework compels a "bottom–up" Li deposition. The Ag nanoparticles react with deposited Li to form a low-nucleation-barrier Li-Ag alloy, resulting in optimized nucleation overpotential and cycling performance. With the in situ optical microscope which enables the observation of Li deposition behaviors in OPA substrates, the ideal "bottom–up" Li deposition was clearly evidenced (Figure 8d). As a result, the OPA-based LMA can stably operate over 600 h while keeping at a low overpotential (<50 mV) at 4 mA cm^{-2} and 4 mAh cm^{-2}. Wang et al.[45] constructed a 3D graphene network host decorated with highly dispersed lithiophilic inorganic components (i.e., Li_2O and Li_2CO_3) and coated with an insulating interphase of boron nitride (BIG), to achieve a highly reversible and stable Li anode. Due to the Lewis acid and insulating properties of boron nitride in the BIG structure, homogeneous Li plating and "bottom–up" Li deposition can be achieved. On the contrary, Park et al.[113] reported an electrical conductivity-controlled 3D host consisting of a glass fiber (GF) backbone coated with size-/conductivity-controlled partially reduced graphene oxide (PrGO). This PrGO-coated GF was then combined with a Cu substrate to form the final 3D host (PrGO-GF/Cu), as illustrated in Figure 8e. The cross-sectional SEM images display the "bottom–up" Li growth upon increasing Li plating capacity (Figure 8f). In another work, Fan et al.[114] introduced a 3D hybrid LMA composed of molten lithium and Al_2O_3 particles on the conductive substrate, resulting in the formation of a thin layer of Li-Al-O on the surface of Al_2O_3. The insulating property of the Al_2O_3 skeleton forces Li^+ to migrate to the bottom and gain electrons from the conductive substrate, leading to a dense Li electrodeposition layer through a "bottom–up" deposition manner.

Li metal plating can only initiate in limited areas with electrochemically active sites, as electrons are unable to transfer through the dielectric regions. Consequently, it is difficult to achieve stable and durable Li plating and stripping, especially at high current densities and high cycling capacities, and such hosts cannot self-eliminate undesired dendrites. Zou et al.[115] developed a periodically conductive-dielectric nanofiber lamella host for Li metal, which enables stable and smooth Li plating based on Sand's time theory. The design consists of alternating layers of electrically conductive and dielectric materials (PAN/CNF) with polar functional groups to attract and homogenize the Li^+ flux within the matrix (Figure 8g). Each separated conductive layer possesses massive electrochemically active sites and the dielectric layers are anchored with abundant polar functional groups (i.e., nitrile and carbonyl groups) to attract Li-ions and thus, homogenize/confine the ionic flux within the matrix. Even if uneven Li deposition occurs inside the matrix, the parasitic propagation will still be blocked by the overhead conductive layers in view of the fact that they are electrically equipotential for re-homogenizing the local electric field. With this design, Li metal can only be initially plated on the bottom conductive layer and then progressively fill the overhead layers, displaying a desirable "bottom–up" plating pattern. Evident from Figure 8h, when cycling at a current density of 3 mA cm^{-2} with a cycling capacity of 3 mAh cm^{-2}, the Li@PAN/CNF||Li@PAN/CNF battery maintains excellent stability with a lower plating overpotential of 52 mV over 835 cycles, dramatically superior than those of Li@PAN||Li@PAN battery (400 cycles) and Li@CNF||Li@CNF battery (122 cycles), respectively.

To sum up, utilizing materials with gradients in terms of conductivity is an important strategy to guide uniform lithium metal deposition. The simulation results provide insight into how the Li^+ fluxes and electric field distribution can be tailored by engineering the framework architecture. The main advantage of this method is the ability to manipulate Li^+ and electron transport to achieve homogeneous Li plating. However, the cycling capacity and current density may be limited by the properties of the less conductive components. A single conductivity gradient may not be enough to achieve uniform Li plating in subsequent cycles. Further modifications combining multiple strategies are required to improve the Li deposition process. More work is still needed to further optimize these structured architectures and understand the intricacies of lithium deposition within these gradient frameworks through modeling and in-operando characterizations. Furthermore, the scalability and practical implementation also need to be addressed.

4.1.2. Constructing Lithiophilicity Gradient

The general 3D structures used for lithium anodes (e.g., carbon fibers,[116] porous Cu, Ni foam) with high specific surface areas suffer from poor affinity for lithium, resulting in high nucleation barriers and fewer nucleation sites. Materials such as Au,[42] Ag,[117] Sn,[118] Al,[119] Zn,[120] and Mg[121] have shown lower nucleation barriers and are preferred for Li growth, along with effective Janus structures to guide homogeneous Li deposition. However, even distribution of lithiophilic substances can cause preferential nucleation and deposition at the top zone under harsh conditions. Gradient distribution of lithiophilic materials in hosts has been shown to regulate the "bottom–up" Li deposition and inhibit Li dendrite growth, and this section summarizes and discusses the latest progress in lithiophilicity gradient designs for Li metal hosts.

ZnO with good Li affinity is one of the most frequently used lithiophilic materials for fabricating lithiophilicity gradient hosts. As one of the earliest studies, Nan and co-workers[116] proposed a conductive framework (carbon nanofiber) with gradient-distributed nucleation seeds of ZnO particles (donated as G-CNF) as the 3D host for LMA (**Figure** 9a,b). The distribution gradient of ZnO particles is counter to the lithium-ion concentration gradient, which could reverse the lithium nucleation tendency from top to bottom of the 3D hosts and lead to stable "bottom–up" deposition of lithium. When the lithium deposited G-CNF (G-CNF-Li) is applied in a full cell coupling with a commercial LFP cathode (N/P ratio of 15), a stable capacity of 115 mAh g^{-1} and a high capacity retention ratio of 95.7% after 300 cycles are achieved. Likewise, a lithiophilic gradient host, that is, ZnO/rGO/CNTs (G-ZGC), was reported by Zhou and co-workers.[98] The ZnO nanoparticles anchored on the graphene sheets enable hierarchical induction of Li nucleation and guide Li deposition into the 3D host. This structure delivers a CE as high as 98.2% for at least 500 cycles, and the symmetrical cell comprising the host operates smoothly for >920 h with a low overpotential below 20 mV. Electrostatic spinning is a promising way to further improve the mechanical properties of substrates. Zhao et al.[122] demonstrated a PVDF framework with a Ag concentration gradient as the 3D host for LMA (C-Ag/PVDF) (Figure 9c). The structure inhibits Li "top deposition" due to the electrically insulating polymer layer at the top, while ensuring uniform "bottom–up" Li growth through high-activity lithiophilic sites at the bottom (Figure 9d). In situ optical microscope test shows a great number of lithium (ca. 40 mAh cm^{-2}) is deposited in the bottom region. More importantly, the lithium deposits gradually and fills the whole 3D framework without obvious dendrites formation, providing evidence of the "bottom–up" Li growth mode (Figure 9e). This results in an ultralong lithium stripping-plating lifetime (>1300 h) even at a high current density of 4 mA cm^{-2} and a capacity of 4 mAh cm^{-2}. Inspired by the substances transpiration process in trees, Zhu et al.[123] designed a 3D wood-derived carbon (WDC) framework decorated with gradient-distributed metal nanoparticles to regulate Li deposition. The WDC framework preserves the natural

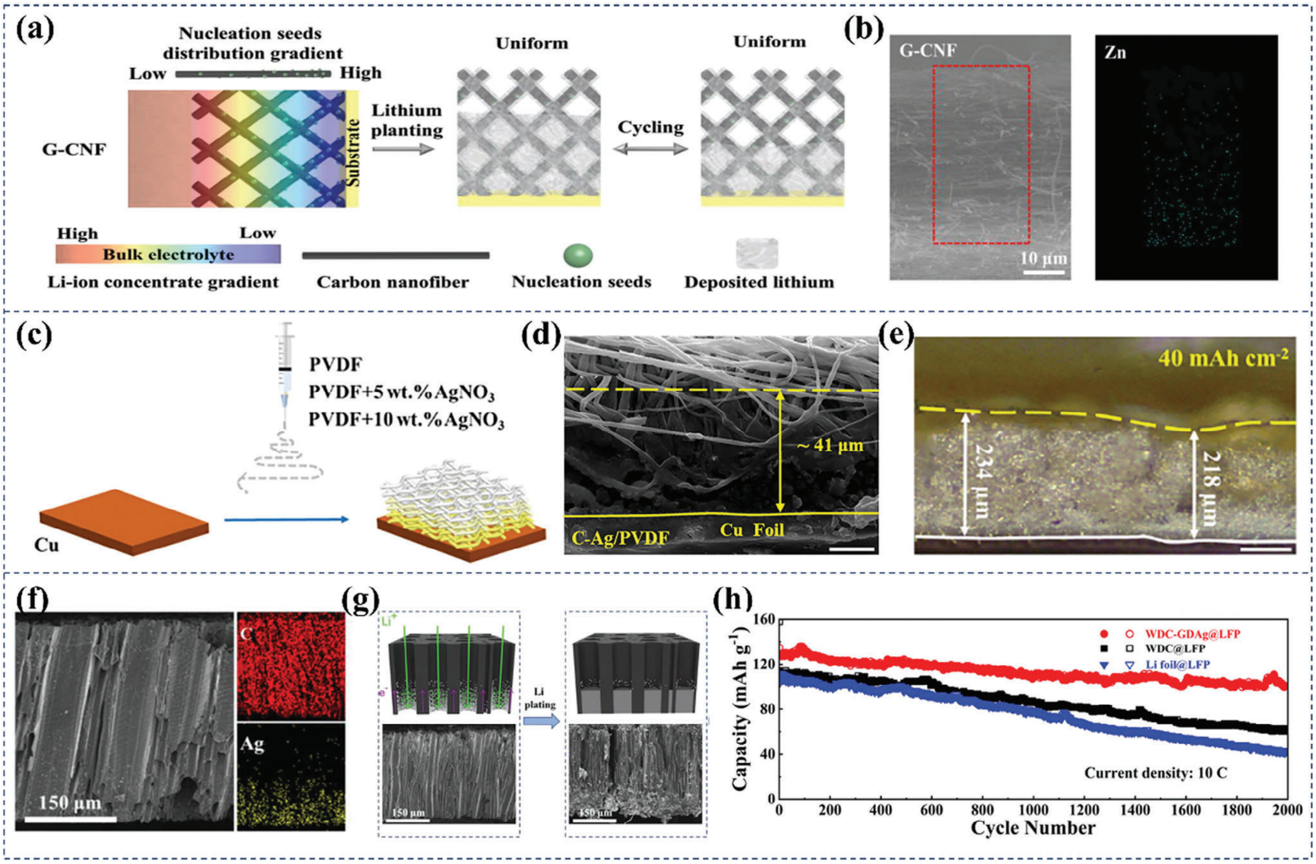

Figure 9. a) Schematic diagram of the working principle of G-CNF in regulating lithium deposition; b) Cross-sectional SEM image of G-CNF and EDS mapping of Zn element. Reproduced with permission.[116] Copyright 2019, Wiley. c) Schematic illustration of the synthetic procedure of the C-Ag/PVDF; d) Cross-view SEM images of C-Ag/PVDF after Li deposition with a capacity of 5 mAh cm^{-2}; e) In situ optical observations of Li deposition on C-Ag/PVDF at a current density of 5.0 mA cm^{-2}. Reproduced with permission.[122] Copyright 2022, Elsevier. f) Cross-sectional EDX elemental mapping images of WDC-GDAg scaffold; g) Schematic diagram and cross-sectional SEM images of WDC-GDAg at 1 mA cm^{-2} with capacities of 0 and 3 mAh cm^{-2}; h) Cycling performance of WDC-GDAg@LFP at 10 C. Reproduced with permission.[123] Copyright 2023, Wiley.

wood channel structures to provide pathways for fast Li$^+$ transport. Metal nanoparticles (Ag, ZnO, Au) deposited on the WDC framework is realized by a capillary-induced gradient method (WDC-GDM, M = Ag, ZnO, Au). Characterizations by SEM and EDX confirm the successful fabrication of WDC-GDAg scaffolds with a gradient distribution of Ag nanoparticles along the vertical channels (Figure 9f). The Li deposition behavior in the WDC-GDAg scaffold apparently follows an ideal "bottom–up" plating phenomenon (Figure 9g). Consequently, the WDC-GDAg@LFP can deliver a high capacity of 130 mAh g^{-1} and achieve stable cycling performance with high capacity retention of 78.9% even over 2000 cycles at 10 C (Figure 9h).

Magnetron sputtering is an excellent method for building gradient lithiophilic layers, where the metal can be alloyed directly with lithium without conversion reactions, so there is no loss of lithium during pre-deposition. Hong et al.[124] demonstrated a general concept to spatially guide lithium metal deposition in the interior of Janus 3D hosts with one lithiophilic surface and another lithiophobic surface. Specifically, the structure is designed by modifying a Janus 3D carbon paper electrode with evenly distributed gold nanoparticles (Au/CP) through a simple sputtering process. The lithiophilic nature of Au nanoparticles attracts Li$^+$, allowing for even and continuous deposition of metallic lithium along carbon fibers in the 3D Janus host. This results in uniform deposition throughout the entire structure, rather than just on the carbon fibers surface. The Au/CP electrode exhibits an excellent CE of 99.1% over 100 cycles at 1.0 mA cm^{-2} in the ether-electrolyte. Similarly, Li et al.[125] developed a 3D Janus current collector using lithiophilic Au layer modification on carbon fabric (CF) to create a stable and safe LMA. The Janus Au layer guides the deposition of Li to the bottom of CF resulting in high electrochemical stability and superior mechanical deformability. This development is promising for future applications in flexible and wearable electronics. Although Au or Ag has excellent lithiophilicity, the high cost greatly hinders the practical battery applications, alternatively, the low-cost non-metallic silicon is a good candidate for alloying with lithium. Yan et al.[49] proposed a gradient Si-modified carbon paper (GSCP) composite anode via magnetic sputtering. The constructed gradient lithiophilic structure ensures Li metal to selectively nucleate and grow at the bottom first and then toward the top part of GSCP (**Figure 10a**). Based on the density functional theory (DFT) calculations, the binding energy of lithium on the (001) facet of pure Li is less negative with respect

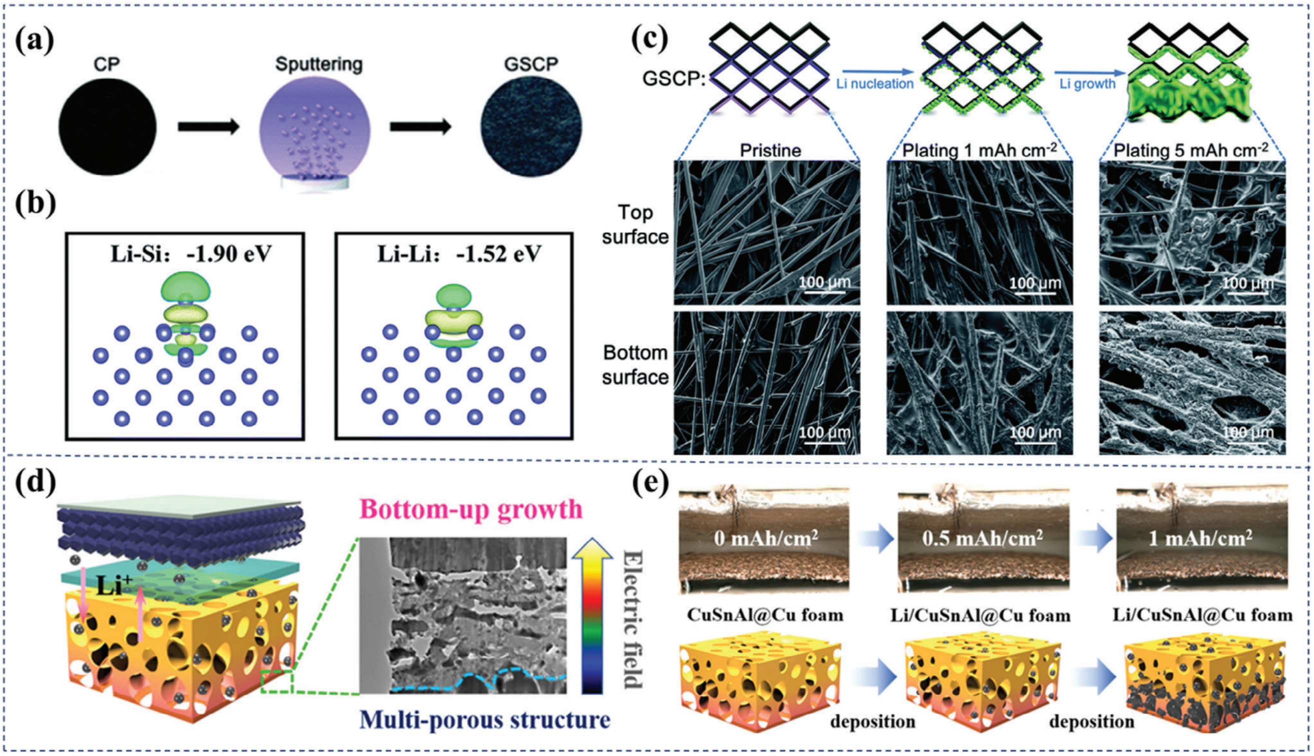

Figure 10. a) The scheme of the fabrication process for GSCP; b) The difference of charge density for Li on Si-doped Li (001) and Li (001) surfaces and their corresponding binding energies; c) Schematic Li plating behaviors on GSCP electrodes. Reproduced with permission.[49] Copyright 2019, Royal Society of Chemistry. d) Schematic demonstration of the CuSnAl@Cu foam structure and cross-sectional TEM image of its bottom zone; e) In situ optical microscope photos and corresponding Li plating scheme of CuSnAl@Cu foam at a current density of 1 mA cm^{-2}. Reproduced with permission.[126] Copyright 2022, American Chemical Society.

to the binding energy of lithium on Si-doped Li (001), ca. –1.52 versus –1.90 eV (Figure 10b), validating the lithiophilicity gradient of GSCP. This design enables stable Li plating/stripping and high space utilization of the 3D host (Figure 10c), resulting in prolonged lifespan (1350 h) with a low overpotential (15 mV). Tin is also a suitable material due to its high theoretical capacity for lithium storage (about 992 mAh g^{-1} for $Li_{4.4}Sn$) and high lithiophilicity. Recently, Lv et al.[126] developed a CuSnAl@Cu foam electrode by sputtering a CuSnAl layer on one side of Cu foam skeleton and then using a chemical dealloying process in acid solution to create micropores on the surface (Figure 10d). The CuSnAl@Cu electrode exhibits enhanced lithiophilicity, which allows for preferential Li nucleation from Sn sites due to their stronger affinity and lower nucleation barrier toward Li. This can be confirmed by in situ optical microscope (Figure 10e).

In short, the strategy of constructing a lithiophilicity gradient enables preferential lithium deposition at the lithiophilic region and meanwhile generates compact and uniform morphology. Additionally, the incorporation of a 3D conductive architecture, such as carbon paper or foam, is also imperative to impart robust mechanical support, an expanded surface for plating accommodation, and rapid electron transfer kinetics. However, compatibility between the materials with different lithiophilicity needs further optimization, and there is less flexibility in tailoring the specific gradient distribution. Overall, the lithiophilic gradient methodology exhibits promise to stabilize the LMA by orchestrating homogenous electrodeposition and mitigating dendrite propagation. Future efforts remain essential to scale up these “proof-of-concept” configurations and additional screening and optimization of promising lithiophilic materials in order to balance the desired attributes of high lithium affinity, suitable electrical conductivity, and minimal fabrication cost.

4.1.3. Constructing Dual Gradient Hosts

Dual-gradient hosts combine the advantages of electric conductivity gradient and lithiophilicity gradient, which synergistically addresses the issue of uncontrolled Li growth. Pu et al.[127] reported a deposition-regulating strategy (DRS) by coating Al_2O_3 and Au at the top and bottom regions of a bare nickel scaffold (BNS), respectively. The Al_2O_3 coating lowers the local electric conductivity in the top region to form a conductivity gradient as compared to the bottom metallic Ni/Au. The bottom Au serves as the lithiophilic coating to form a lithiophilicity gradient as compared to high-barrier Al_2O_3 coating. The resulting DRS anode demonstrates a high CE of ≈98.1% for 500 cycles (3.5 mAh cm^{-2}; 2 mA cm^{-2}). It also shows better performance than Li anodes on Cu foil and BNS at high rate (10 mA cm^{-2}) and very low temperature (−15 °C).

Physical vapor deposition (PVD) and chemical vapor deposition (CVD) are established techniques for engineering lithiophobic–lithiophilic gradients in advanced battery anodes. PVD offers precise control over film thickness and composition

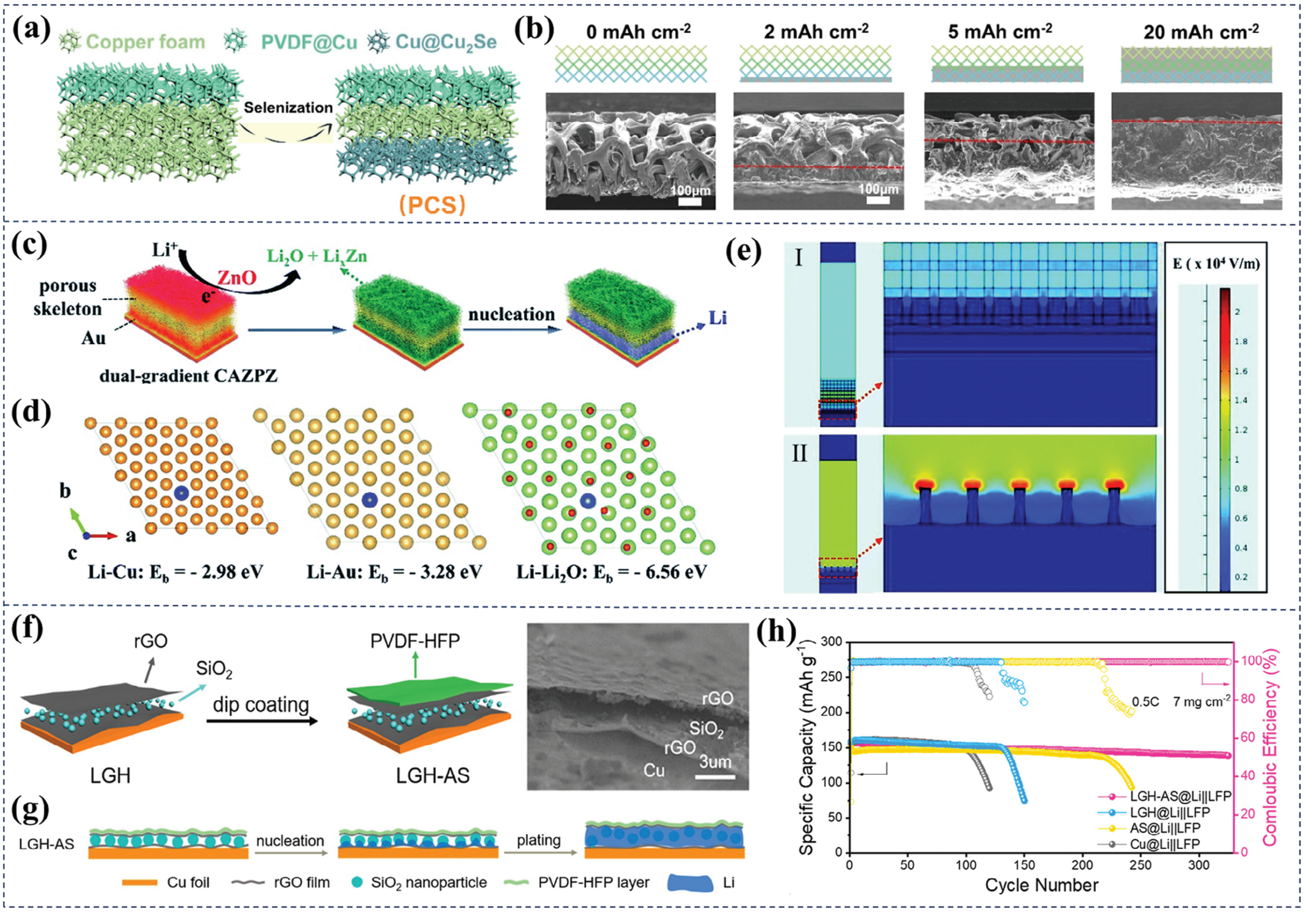

Figure 11. a) Schematic illustration of the synthesis procedures of the PCS electrode; b) Schematic illustration and side-view SEM images of the PCS to PCS/Li (deposited Li amount: 2 mAh cm^{-2}, 5 mAh cm^{-2}, and 20 mAh cm^{-2} at 1 mA cm^{-2}). Reproduced with permission.[50] Copyright 2019, American Chemical Society. c) Schematic diagram of Li plating/stripping behavior on CAZPZ current collectors; d) The calculated binding energies between Li atoms and Cu, Au, and Li_2O substrates; e) Simulation models of electric field values of the plated Li on the (I) CAZPZ and (II) Cu current collectors after Li nucleation. Reproduced with permission.[129] Copyright 2021, Royal Society of Chemistry. f) Fabrication and characterization of the LGH-AS electrode; g) Li is preferentially plated from the bottom to the top in the SiO_2-embeded interlayer with the protection of an upper rGO/PVDF-HFP layer; h) Specific capacities, CEs, and cycling performance of full cells derived from the four Li anode hosts at 0.5 C. Reproduced with permission.[131] Copyright 2021, American Chemical Society.

at lower temperatures, but is less suited for complex geometries and large-scale applications due to slower deposition rates and potential adhesion challenges. In contrast, CVD provides excellent uniformity and adhesion, even on intricate structures, and produces dense, high-quality films. Nevertheless, CVD often operates at higher temperatures and can involve toxic precursors, which may raise environmental and safety concerns. Huang et al.[50] developed a gradient structure of PVDF@Cu@Cu_2Se on Cu foam (PCS) using an auto coater machine to apply the PVDF slurry to the Cu foam, with the uncoated side reacting with selenium gas via CVD (**Figure** 11a). The upper PVDF layer prevents Li^+ reduction at the anode/separator interface, while the bottom lithiophilic Cu_2Se nanoparticles with high ionic conductivity capture Li^+ for uniform deposition to promote stable lithium plating/stripping. The cross-sectional SEM images provide good evidence of the “bottom–up” deposition of lithium (Figure 11b). The PCS/Li||LFP cell with a low N/P ratio of 2.5 demonstrates a high-capacity retention rate (94.4% at 1 C) over 450 cycles and stable CEs compared to those of Li||LFP cell. Starting from the same idea, Zhang et al.[47] used a gradient nucleation method to alleviate the negative impact of Li dendrite growth on 3D current collectors during Li plating. They coated Au and polymer on the bottom and top sides of Cu mesh, respectively. The Au-coated area exhibits the lowest overpotential and preferentially initiated Li nucleation, confining subsequent Li deposition mainly inside the polymer/Cu mesh/Au.

Due to the light weight of carbon material, it is also a great choice to use it for building a double-gradient host. Li et al.[128] developed a 3D CNF host called CBG with bidirectional gradient modification, including a ZnO top–down gradient and a Sn bottom–up gradient. During the first cycle, lithiation of ZnO with Li^+ leads to the formation of Li-Zn alloy and Li_2O. This process imparts high Li^+ diffusion capability and moderate conductivity to the scaffold. Additionally, metallic Sn lowers the Li nucleation potential due to its strong affinity to Li, guiding preferential Li deposition from the bottom. Owing to the low bulk density of CBG (0.1 g cm^{-3}), the weight percentage of lithium is 51wt% in the composite anode when depositing a capacity of 5 mAh cm^{-2} of Li. Then, Liu et al.[35] used a suction filtration method to fabricate dual-gradient networks with an upper layer of CNTs and a lower layer composed of a 3D composite of Ag nanowires and CNTs. Initially, the uniformly dispersed Ag nanowires in the lower layer enable the conductive framework to create a progressive deposition route for metallic Li, owing to the strong conductivity and lithiophilicity of Ag itself. In addition to building a gradient conductive layer by modifying the carbon material host with a more conductive material, it is also possible to combine the carbon material with a Cu foil collector to provide a highly conductive bottom layer. Zheng et al.[129] developed a Cu-Au-ZnO-PAN-ZnO (CAZPZ) current collector for the LMA, where lithiophilic Au and ZnO layers provide nucleation sites and decrease Li nucleation overpotential, resulting in homogeneous Li nucleation (Figure 11c). DFT calculations indicate that the Au surface has more negative binding energy than the Cu surface (−3.28 vs −2.98 eV) with Li, suggesting that Au is more lithium-friendly and thus favoring the decreased Li nucleation overpotential (Figure 11d). The upper ZnO layer reacts with Li^{+} and electrons to form a highly ion-conductive and lithiophilic ASEI layer of Li_2O/Li_xZn, which regulates well-distributed Li^{+} flux. Additionally, the high mechanical strength of Li_2O prevents direct penetration of Li. The comparative simulation results of the electric field distributions of the CAZPZ-Li and Cu-Li anodes after Li nucleus formation suggest that the CAZPZ current collector is a better choice for promoting uniform Li^{+} flux and heterogeneous Li deposition (Figure 11e). Zhang et al.[130] designed a Si@CNFs@ZnO skeleton coated ZnO-Cu foil (SCZ) through the combination of electrostatic spinning and magnetron sputtering techniques. The introduction of lithiophilic ZnO particles at the bottom of the SCZ reduces the overpotential to 12.4 mV and the Cu foil provides a better conductivity than the CNF skeleton, resulting in a 3D dual-gradient host that induces "bottom−up" lithium deposition. The sputtered Si could be lithiated to form Li_xSi alloy, which provides a homogeneous channel for Li^{+} transport on the surface and promotes the uniform lithium deposition. As a result, the SCZ-Li||LFP full cell delivers a high capacity of ≈104 mAh g^{-1} (≈94.82% capacity retention) after 2000 cycles at 5 C. Cai et al.[131] developed an ASEI gradient host consisting of a bottom rGO layer, a SiO_2 interlayer, an upper rGO layer, and a top poly(vinylidenefluoride-hexafluoropropylene) (PVDF-HFP) layer (LGH-AS) (Figure 11f). The design allows for enhanced adhesion of SiO_2 particles, conducting electrons from Cu foils, forming electronic pathways, and floatable Li storage space. The upper rGO film suppresses Li dendrites while constructing a flat and relatively dense ASEI. Furthermore, the top PVDF-HFP layer keeps the whole electrode surface insulated, which guides Li plating priorly in the SiO_2-filled interlayer (Figure 11g). The LGH-AS@Li||LFP cell exhibits an average CE of 99.87% with a capacity retention ratio of 90.22% after 300 cycles at 0.5 C (Figure 11h).

The dual-gradient design is an effective strategy to construct LMA hosts with directional lithium deposition. One of the primary advantages of this strategy is the synergistic effect of the dual gradients, which provides a controlled environment for Li deposition, resulting in high CE and extended cycle life of the batteries. Additionally, the dual-gradient approach can be adapted to various substrate materials, including Cu foam, Ni scaffolds, and carbon-based substrates, allowing for flexibility in designing LMAs that are compatible with a wide range of battery chemistries and configurations. However, the complexity of fabricating these dual-gradient structures can be considered a major disadvantage, as it often requires sophisticated and multi-step processes, such as CVD and magnetron sputtering. This not only increases the production cost but also poses challenges in scaling up the manufacturing process for commercial applications.

4.1.4. Constructing Pore-Size Gradient

A pore-size gradient structure can be created in the anode where pores gradually increase in size by modulating the size of nanoparticles, which allows for more lithium storage in the larger pores and faster Li^{+} migration. This results in lower concentration gradients within the 3D host, making better use of the available space and preventing lithium metal from depositing at the top surface.

Lee et al.[132] created a pore-size gradient structure by sintering Cu metal powders, which allowed for conformal electrodeposition of Li metal due to the gradual decrease in total resistance along the depth of the framework (Grad) (**Figure 12a**). The charge-transfer and ionic resistances gradually decrease and increase, respectively, with increasing distance from the framework top surface, leading to preferential deposition of Li metal initiating from the innermost part of the framework (Figure 12b). The relatively smaller void spaces in the bottom region are fully filled up with Li, an indication of super conformal Li metal "bottom–up" growth (Figure 12c). The distribution maps of the local current density as a function of the pore depth reveal the uniform Li plating is ascribed to the reduced local current density. This structure delivers stable capacity retention over 760 cycles with an areal capacity of 0.5 mAh cm^{-2} at 2 mA cm^{-2}, indicating excellent electrochemical performance. In another work, Noh et al.[33] created a carbon-based anode (3D-CPA) with varying pore sizes using a polymer template (Figure 12d). The top layer has larger pores (50 µm) to allow for efficient Li ion transport, while the bottom layer has smaller pores (15 µm) to prevent dendrite formation. Therefore, the as-prepared 3D-CPA with a pore-size gradient could direct the Li^{+} transport into the inner pores of the bottom layer via the larger pores of the top layer, without the formation and growth of Li dendrites, thereby resulting in stable cycling performance (Figure 12e).

The pore-size gradient can also be constructed by combining layers with different pore size. Liu et al.[133] used three different 1D carbon materials with varying diameters – multiwalled CNTs (20–30 nm), larger multiwalled CNTs (60–80 nm), and carbon fibers (>150 nm) to create carbon skeletons with gradient pore sizes (GPCS) through a successive casting method (Figure 12f). The 3D distribution of solid phase (PVDF + CNT + CF) and pores in GPCS prove that a carbon electrode with a hierarchical structure was successfully constructed (Figure 12g). The upper portion of the GPCS exhibits a lower absolute current density due to its smaller surface area, leading to slower Li-ion consumption in the upper portion but quicker mass transfer from the bulk electrolyte, resulting in a lower lithium salt concentration gradient compared to the CNTS counterpart. The larger pore size distribution and higher porosity in the upper portion of the GPCS allow for better utilization of inner space and storage of

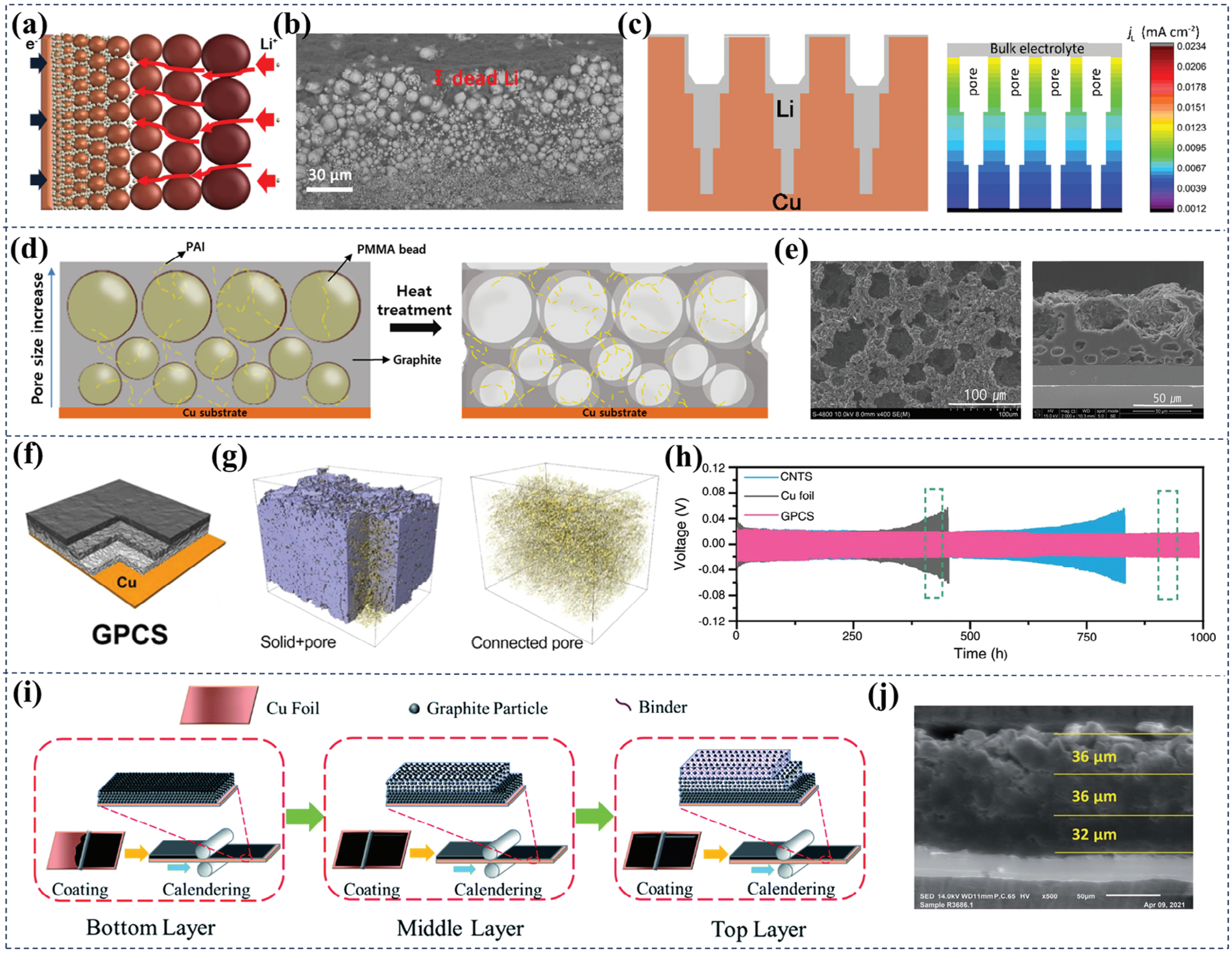

Figure 12. a) Schematic illustration of Li metal plating within the pore-size gradient frameworks; b) Cross-sectional SEM images of the Grad framework after 20 cycles with an areal capacity of 1 mAh cm^{-2} at 2 mA cm^{-2}; c) Schematic illustrations and the distribution maps of the local current density as a function of the pore depth at the total current of 0.2 mA cm^{-2} for gradient cylindrical pore models. Reproduced with permission.[132] Copyright 2021, American Chemical Society. d) Schematic representation of 3D-CPA with a pore-size gradient; e) Top view and cross-sectional SEM images of 3D-CPA. Reproduced with permission.[33] Copyright 2021, American Chemical Society. f) Scheme of the GPCS fabrication process; g) 3D distribution of solid phase (PVDF + CNT + CF) and pore in GPCS; h) Cycling stability of the Li||Li@GPCS, Li||Li@CNTS, and Li||Li@Cu cells at 1 mA cm^{-2}, 1 mAh cm^{-2}. Reproduced with permission.[133] Copyright 2022, Wiley. i) Schematic illustration of the fabrication process for 3-layered electrodes with varied porosities along the thickness direction; j) SEM images showing the cross-sectional view of the 3-layered graphite electrodes. Reproduced with permission.[134] Copyright 2022, Royal Society of Chemistry.

lithium metal. The Li||Li@GPCS cell delivers a stable and low overpotential of 15 mV for almost 1000 h at 1 mA cm^{-2} and 1 mAh cm^{-2} (Figure 12h).

In addition to the design of lithium anode body for LMBs, the aperture gradient structure can also be used for the design of graphite anode structure for lithium-ion batteries. Varied porosities can improve electrolyte infiltration, decrease polarization, and increase active material utilization in thick electrodes for fast charging applications by promoting mass transport and preventing lithium plating. Yang et al.[134] developed a 3-layer graphite electrode with different porosities in each layer using a conventional bar coating method (Figure 12i). Observations of the cross-sectional view of this structure demonstrate that the compaction degree varies along the thickness in the 3-layer graphite electrode: a dense bottom layer near the current collector (32 µm), a relatively loose middle layer (36 µm), and a loose top layer (36 µm) (Figure 12j). Such a design achieves a decreased porosity from surface to bottom. Compared to conventional electrodes with uniform porosity, this gradient porosity electrode has lower overall porosity and higher areal mass loading thanks to the favored mass transportation and prevented dendritic Li formation. This approach has scientific and practical significance in designing and manufacturing fast charge electrodes. **Table 1** summarizes the electrochemical performances and operation parameters of previously reported gradient structures.

In summary, building pore-size gradients is an effective strategy to enhance lithium metal and graphite anode performance by

Table 1. Electrochemical performances and operation parameters of previously reported Gradient structures.

Configuration	Half-cell (CE, current density [mA cm^{-2}], capacity [mAh cm^{-2}], cycle)	Symmetric cell (cycle, current density [mA cm^{-2}], capacity [mAh cm^{-2}])	Full-cell (current density, capacity retention, cycle)	Capacity of Deposited Li for full-cell [mAh cm^{-2}]	Electrolyte	References
Conductivity Gradient						
CDG-sponge	98.4%, 0.5, 1.0, 500	780, 1.0, 1.0	1 C[b], 99.4%,100 (cathode: LFP[a])	3.0	1 M LiTFSI in DOL&DME (1:1 in v/v) with 2% $LiNO_3$	[102]
CG	N.A.	500, 1.0, 1.0	1 C[b], 90.0%, 100 (cathode: NCM811[a])	6.0	1 M LiTFSI in DOL&DME (1:1 in v/v) with 1% $LiNO_3$ 1 M $LiPF_6$ in EC&DEC (1:1 in v/v) with 10% FEC, 1% VC	[109]
LNO-CGH	97.3%, 1.0, 1.0, ≈200	N.A.	1 C[b], 74.9%, 100 (cathode: NCM[a])	5.0	1 M $LiPF_6$ in EC&DEC (1:1 in v/v) with 5% FEC	[8]
SiC/CC	N.A., 5.0, 3.0, 50	1000, 1.0, 1.0	0.5 C, 80.0%, 120 (cathode: LFP)	3.0	1 M LiTFSI in DOL&DME (1:1 in v/v) with 2% $LiNO_3$	[46]
Li-In+ Cu foil	95%, 0.5, 0.5, 100	225, 0.5, 0.5	1 C, 80.8%, 360 (cathode: LFP)	5.0	1 M $LiPF_6$ in EC&DMC (1:1 in v/v)	[42]
OPA	95.6%, 1.0, 1.0, 125	1100, 0.5, 1	0.5 C[b], 84.0%, 100 (cathode:NC90[a])	4.0	1 M $LiPF_6$ in EC&DEC (1:1 in v/v) with 5% FEC	[44]
BIG	98.5%, 0.5, 1.0, 300	1600, 0.5, 1	0.5 C, 88.2%, 300 (cathode: LFP)	3.0	1 M LiTFSI in DOL&DME (1:1 in v/v) with 1% $LiNO_3$	[45]
PrGO-GF/Cu	N.A., 1.0, 1.0, 200	1300, 1, 1	0.5 C, N.A, 500 (cathode: LFP)	4.0	1 M LiTFSI in DOL&DME (1:1 in v/v) with 1% $LiNO_3$	[113]
Al_2O_3	N.A.	900, 1, 1	1 C, 93.6%, 200 (cathode: LFP)	N.A.	1 M $LiPF_6$ in EC&DEC (1:1 in v/v) with 10% FEC, 1% VC	[114]
PAN/CMF	98.1%, 1.0, 2.0, 250	1800, 1, 1	1 C, 70.0%, 100 (cathode: NCM811)	5.0	1 M LiTFSI in DOL&DME (1:1 in v/v) with 2% $LiNO_3$ 1 M $LiPF_6$ in EC&DMC&EMC (1:1:1 in v/v)	[115]
Lithiophilicity Gradient						
G-CNF	98.1%, 0.5, 0.5, 700	1700, 0.2, 0.2	1 C, 95.7%, 300 (cathode: LFP)	5.0	1 M LiTFSI in DOL&DME (1:1 in v/v) with 1% $LiNO_3$ 1 M $LiPF_6$ in EC&DEC (1:1 in v/v) with 1% VC	[116]
G-ZGC	≈98.2%, 1.0, 1.0, 500	920, 1.0, 1.0	N.A.	5.0	1 M LiTFSI in DOL/DME (1:1 in v/v) with 2% $LiNO_3$ 1 M $LiPF_6$ in EC&DEC (1:1 in v/v)	[135]
C-Ag/PVDF	≈96.0%, 0.5, 1.0, 180	1300, 4.0, 4.0	0.5 C, 98.0%, 200 (cathode: LFP)	3.0	1 M $LiPF_6$ in EC&DMC (1:1 in v/v) with 5% FEC 1 M LiTFSI in DOL&DME (1:1 in v/v) with 2% $LiNO_3$ 1 M $LiPF_6$ in EC&DMC (1:1 in v/v)	[122]
CuNW-P	97.4%, 1.0, 1.0, 150	1000, 1.0, 1.0	0.5 C, 98.8%, 300 (cathode: LFP)	3.0	1 M LiTFSI in DOL&DME (1:1 in v/v) with 1% $LiNO_3$	[136]

(*Continued*)

Table 1. (Continued)

Configuration	Half-cell (CE, current density [mA cm^{-2}], capacity [mAh cm^{-2}], cycle)	Symmetric cell (cycle, current density [mA cm^{-2}], capacity [mAh cm^{-2}])	Full-cell (current density, capacity retention, cycle)	Capacity of Deposited Li for full-cell [mAh cm^{-2}]	Electrolyte	References
GSCP	99.0%, 1.0, 1.0, 400	>1350, 1.0, 1.0	10 C[b)], 84.5%, 5000 (cathode: LTO[a)])	5.0	1 M LiTFSI in DOL&DME (1:1 in v/v)	[49]
CuSnAl@Cu	N.A.	2000, 1.0, 1.0	1 C, 99.6%, 300 (cathode: LFP)	1.0	1 M $LiClO_4$ in EC&DEC (1:1 in v/v)	[126]
Dual Gradient						
DRS	98.1%, 1.0, 1.0, 500	500, 2.0, 3.5	N.A.	N.A.	1 M LiTFSI in DOL&DME (1:1 in v/v) with 1% $LiNO_3$	[127]
PCS	98.2%, 1.0, 1.0, 250	≈1100, 1.0, 1.0	1 C, 94.4%, 450 (cathode: LFP)	2.0	1 M LiTFSI in DOL&DME (1:1 in v/v) with 1% $LiNO_3$	[50]
poly/Cu mesh/Au	94.3%, 1.0, 2.0, 100	400, 1.0, 1.0	2 C, 96.4%, 150 (cathode: LFP)	3.0	1 M LiTFSI in DOL&DME (1:1 in v/v) with 1% $LiNO_3$ 1 M $LiPF_6$ in EC&DEC (1:1 in v/v)	[47]
CBG	97.0%, 3.0, 1.0, 120	600, 1.0, 1.0	0.5 C, 99.8%, 300 (cathode: LFP)	5.0	1 M LiTFSI in DOL&DME (1:1 in v/v) with 1% $LiNO_3$	[128]
CAZPZ	99.0%, 0.5, 1.0, 120	600, 1.0, 1.0	5 C, 97.3%, 1000 (cathode: LFP)	5.0	1 M $LiPF_6$ in EC&EMC&DMC (1:1:1 in v/v)	[129]
SCZ	94.8%, 1.0, 1.0, 200	900, 1.0, 1.0	1 C, 84.8%, 500 (cathode: LFP)	5.0	1 M LiTFSI in DOL&DME (1:1 in v/v) with 2% $LiNO_3$ 1 M LiTFSI in DOL&DME (1:1 in v/v) with 1% $LiNO_3$	[130]
LGH-AS	98.1%, 0.5, 0.5, 275	600, 2.0, 1.0	0.5 C, 90.2%, 300 (cathode: LFP)	4.0	1 M LiTFSI in DOL&DME (1:1 in v/v) with 1% $LiNO_3$	[131]
Pore-Size Gradient						
Grad	98.8%, 2.0, 1.0, 350	≈250, 2.0, 0.5	1.0 C, N.A., 200 (cathode: LFP)	3.0	1 M LiTFSI in DME	[132]
3D-CPA	98.8%, 0.6, 1.0 250	660, 1.0, 2.0	0.5 C, 99.8%, 250 (cathode: LFP)	4.0	1 M $LiPF_6$ in EC&DEC (1:1 in v/v) with 10% FEC	[33]
GPCS	98.0%, 0.5, 1.0, 320	1000, 1.0, 1.0	0.7 C, 99.9%, 600 (cathode: LFP)	4.5	1 M LiTFSI in DOL&DME (1:1 in v/v)	[133]

[a)] NCM811 = $LiNi_{0.8}Co_{0.1}Mn_{0.1}O_2$, NCM = $LiNi_{1/3}Co_{1/3}Mn_{1/3}O_2$, NC90 = $LiNi_{0.9}Co_{0.1}O_2$, LTO = $Li_4Ti_5O_{12}$, LFP = $LiFePO_4$; [b)] 1 C value: NCM811 = 200 mA g^{-1}, NCM = 150 mA g^{-1}, NC90 = 200 mA g^{-1}, LTO = 175 mA g^{-1}, LFP = 170 mA g^{-1}.

promoting uniform lithium plating and improving mass transport. The larger pores in the top sections allow for facile electrolyte penetration to utilize the inner electrode space. However, fabricating an optimized gradient structure can be complex and difficult to scale up. The gradation scale needs to be carefully tailored according to specific electrode materials and battery operating conditions to achieve desired performance enhancements. Further work is needed to develop scalable manufacturing methods for graded pore electrodes.

The determination of the gradient scale from bottom to top depends on several factors such as the battery design, material properties, and operational conditions. There isn't a single optimal value for the gradient scale, and it's often a trade-off between several performance metrics. There are numerous challenges in this field that are worth exploring, such as determining how to precisely control the gradient scale to optimize the performance of LMBs, understanding and simulating the impact of the gradient scale on battery performance, designing and preparing new composite materials with an optimized gradient scale. Research into these topics will aid in gaining a deeper understanding of the gradient effect and will promote the further advancement of LMB technologies.

4.2. Other Strategies

4.2.1. Engineering Doping/Defects

We have previously detailed the construction of lithiophilicity gradient that guides the deposition of lithium metal to the bottom. However, when it comes to the abrupt lithiophobic–lithiophilic interface, the asymmetric Li deposition feature can lead to stress accumulation on both sides. It is known that Li preferentially deposits on the lithiophilic side due to a lower nucleation barrier. Upon Li plating process, a localized expansion on the lithiophilic side occurs. In contrast, the lithiophobic side undergoes minimal expansion due to its limited lithium uptake. This asymmetry in expansion creates a mechanical gradient, inducing stress within the current collector. The stress originates from the differential strain, where the expanding lithiophilic side exerts a force on the adjacent, less expanding lithiophobic regions. The induced stress is not merely a surface effect but extends into the bulk of the material due to the 3D nature of the current collector. The material's response to this stress is an intrinsic property, depending on their mechanical properties such as Young's modulus and yield strength. Over repeated cycling, the stress can lead to the formation of microcracks or the delamination of the collector, damaging the mechanical integrity and decaying the electrochemical performance of the batteries. Thus, while designing a stable 3D current collector, resistance to repeated stress should be taken into sufficient consideration. Introducing doping or defect engineering throughout the structure can eliminate the impacts of the abrupt lithiophobic–lithiophilic interface. Furthermore, a 3D current collector with high mechanical strength is better equipped to withstand expansion and contraction.

The introduction of nitrogen doping into carbon materials can increase their lithiophilic properties by creating additional active sites for lithium-ion-binding beneficial from the higher affinity for lithium ions. Thus, Cheng et al.[137] created a successive nitrogen gradient through in situ floating polymerization of polyaniline on polymer fibers (NCNF). The bottom side (marked as NCNF-B) in contact with aniline monomer solution obtains a high N content. EDS result clearly demonstrates a nitrogen concentration gradient, decreasing from 15.1% to 8.7% from bottom to top. To counteract the stress fatigue caused by repeated Li deposition at the bottom side, they pyrolyzed CuCNF and NCNF fibers that had been pressed together (**Figure** 13a). As shown in Figure 13b, after 50 cycles the deformation of CuCNF-NCNF shows that the lithiophobic side (top) is sensitive to fatigue break. The collector bent in the opposite direction of Li deposits. Thus, the CuCNF top layer exhibits not only lithiophobic feature, but also strong mechanical property, which can serve as a "reinforcing rib" during cycling. Quantitative mechanical testing reveals the CuCNF possesses a higher tensile strength of 3.07 MPa and larger strain of 40% compared to those of the CNF. The CuCNF exhibits a significantly higher nominal fracture energy of 492 J m^{-3} (vs 217 J m^{-3} for CNF), indicating superior resistance of the CuCNF to repeated deformation during cycling (Figure 13c). This optimized mechanical–electrochemical gradient structure enables both uniform Li plating and protection of the current collector. In another work, Ma et al.[138] developed a 3D lithiophilic–lithiophobic Janus-faced graphene oxide (JFG) substrate for dendrite-free and long-life LMBs by combining a pore-size gradient with a doping gradient (Figure 13d). Ammonium chloride was used to build a 3D porous network due to its foaming agent feature and meanwhile to introduce N atoms into the carbonized graphite lattice during high-temperature treatment process. One side of GO is occupied by large pores with a depth of ≈ 10 µm, while the other side possesses a relatively dense structure with small pores and average depth of ≈ 20 µm (Figure 13e). The macropore-enriched GO away from the cathode provides space for Li storage, while the GO near the cathode has dense structure with nanopore channels that inhibit Li dendrite growth but allow Li-ions to penetrate. EDS plots demonstrate the gradient nitrogen doping in the 3D structure. The combination of pore-size and N-doping gradients allow for uniform "bottom–up" lithium deposition and low nucleation overpotential and highly reversible Li plating/stripping performance.

Oxygen defects in metal oxides can be modulated to optimize the structure and surface polarity of 3D bodies for better charge and mass transfer. Metal–organic frameworks (MOFs) with high specific surface area are often used as precursors for metal oxides and carbonaceous nanomaterials due to their versatility and tunability, and their pyrolysis may lead to the generation of oxygen defects. These defects act as mobile electron donors and inhibit the growth of Li dendrites by mitigating anion concentration gradients. Herein, Wu et al.[139] developed an electrode for lithium-ion batteries by coating Cu foil with pyrolyzed Mg-MOF, which exhibits a 3D nanoporous structure of oxygen-rich defective magnesium oxide and carboxyl-rich amorphous carbon (MgO_x-C) (Figure 13f). The carboxyl group acts as a pro-lithium site to guide the uniform entry of Li^+, while the oxygen defect in the magnesium oxide domain acts as a pro-anion site to absorb anions from the electrolyte and improve charge transfer. The optimized geometries and bonding states of the $TSFI^-$ anions attracted on the MgO and MgO_x (200) surfaces indicate that two Mg–O bonds are prone to be generated between MgO_x and $TFSI^-$ due to the loss of O in MgO_x, which causes the nearby Mg to combine with another O of $TFSI^-$, leading to a much higher binding energy of 4.34 eV (Figure 13g). The resulting Li@MgO_x-C electrode allows stable Li plating and stripping for over 400 cycles at 1 mA cm^{-2} with a plating capacity of 2 mAh cm^{-2}.

The examples illustrate how thoughtful design of dopant distribution or oxygen defect gradients in the anode structure can create favorable interfaces to guide uniform lithium deposition and prevent dendrite formation. However, this approach also faces challenges like poor scalability, degraded mechanical integrity with increased cycling, and sensitivity to the concentration and distribution of dopants or defects. Although this doping/defect engineering approach shows promise for controlling dendrite growth, further work is still needed to optimize scalable processing techniques and determine optimal doping concentrations for stable cycling performance.

4.2.2. Building Homogenized Electric Field

The 3D conducting host reduces dendrite growth by reducing the average current density per electrode area, but electric field (E-field) polarization within the anode can cause metal to preferentially nucleate and grow on the top surface, leading to dendrite

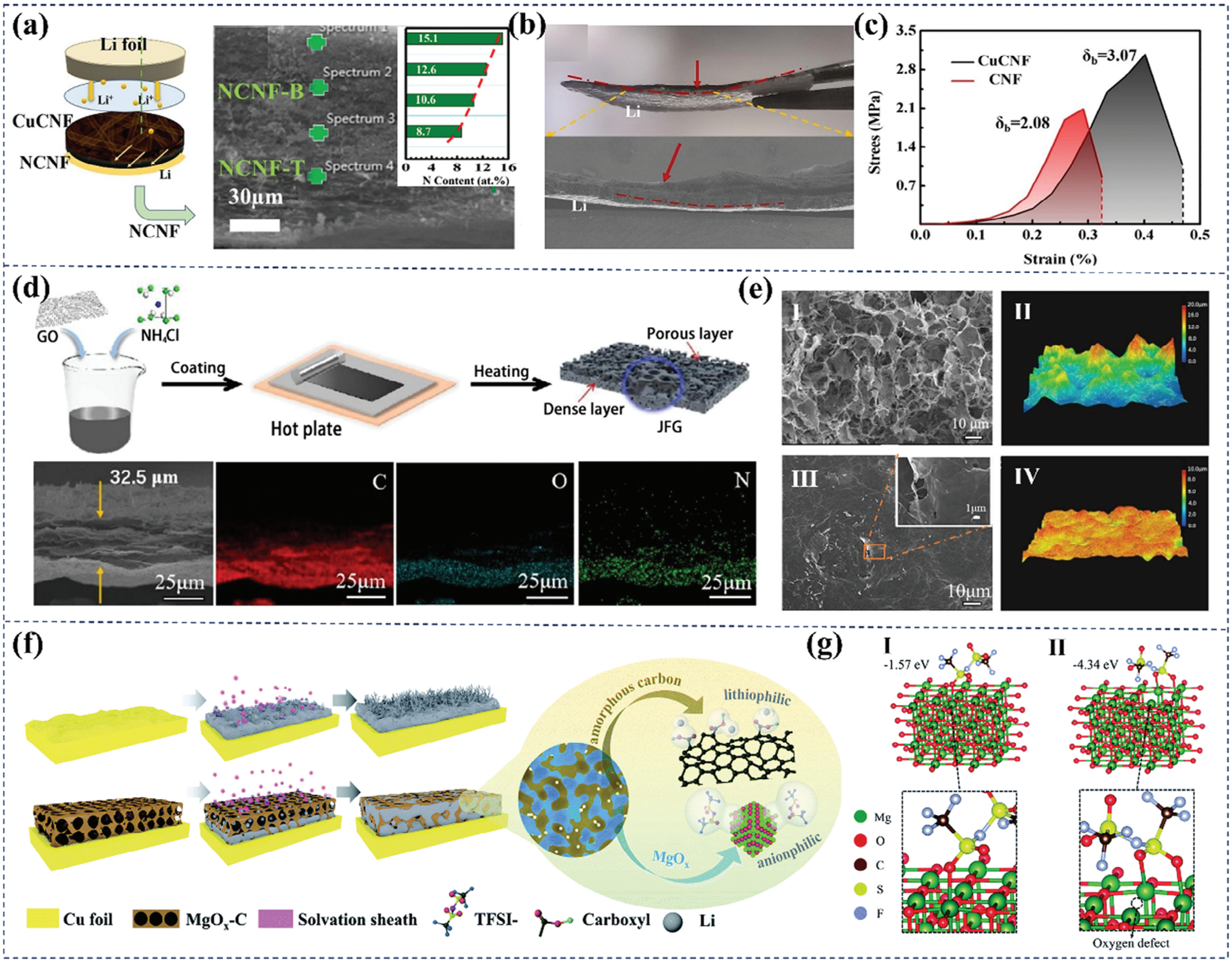

Figure 13. a) The N-doping gradient distribution of NCNF; b) Deformation of CuCNF-NCNF after cycling; c) Tensile stress-strain curve of the CNF and CuCNF. Reproduced with permission.[137] Copyright 2021, Elsevier. d) Schematic illustration, cross-sectional SEM image and the corresponding C, O, N elemental mappings of JFG; e) (I, III) SEM images and (II, IV) super-large depth of field 3D microscopic images of the (I, II) porous and (III, IV) dense layers. Reproduced with permission.[138] Copyright 2022, Elsevier. f) Schematic illustration of Li morphology evolution during Li plating on Cu foil with and without MgO_x-C coating; g) Schematic diagrams of the optimized geometries and bonding states of the $TFSI^-$ anions attracted on the (I) MgO and (II) MgO_x (200) surfaces. Reproduced with permission.[139] Copyright 2020, Royal Society of Chemistry.

aggregation. To achieve stable and safe LMAs, it is critical to homogenize the electric field distribution within the whole electrode. In the following we will discuss how "bottom–up" lithium deposition can be achieved by adopting an electric field modulation strategy.

Zou et al.[140] developed a technology that uses a self-supported and reticular scaffold made of conductive Ni nanowires coated with a thin dielectric and Li^+ conductive layer of Li_2O (called Ni@Li_2O-NW) to modulate the electric field of LMA (**Figure** 14a). The E-field in the controlled sample (Ni-NW membrane) is more concentrated on top of the reticular anode, causing a shielding effect within the anode. Consequently, lithium metal growth is preferentially initiated on the Ni-NW skeleton near the cathode, exacerbating the shielding effect. Finite element analysis simulations disclose that partially replacing the conductive Ni-NW with a thin layer of dielectric Li_2O can homogenize the E-field distribution in the entire LMA (Figure 14b) and thus reduce locally uneven Li^+ flux distribution during Li deposition. This leads to unprecedented capacity retention (103.8%) and CE of (99.9%) at 1 C after 300 cycles in a Li@ Ni@Li_2O-NW||LFP full cell. Developing highly conductive lithium hosts with ample sub-space to homogenize E-field distribution and ion flux is necessary for ultra-stable and dendrite-free LMAs. Zhang et al.[141] used free-standing and surface-oxidized 3D hollow porous Cu fibers (3D-HPCFs) to manipulate both E-field and Li^+ flux distribution for enhanced electrochemical plating behavior of Li (Figure 14c). Simulations using COMSOL show homogenization of Li^+ flux and E-field throughout the electrode due to interconnected "sub-spaces" in the unique hollow porous structure of 3D-HPCFs and less-conductive surface oxide layer on the Cu matrix (Figure 14d). Additionally, dispersed CuO/Cu_2O nanoparticles anchored on the surface of 3D-HPCFs serve as seeds for uniform Li metal

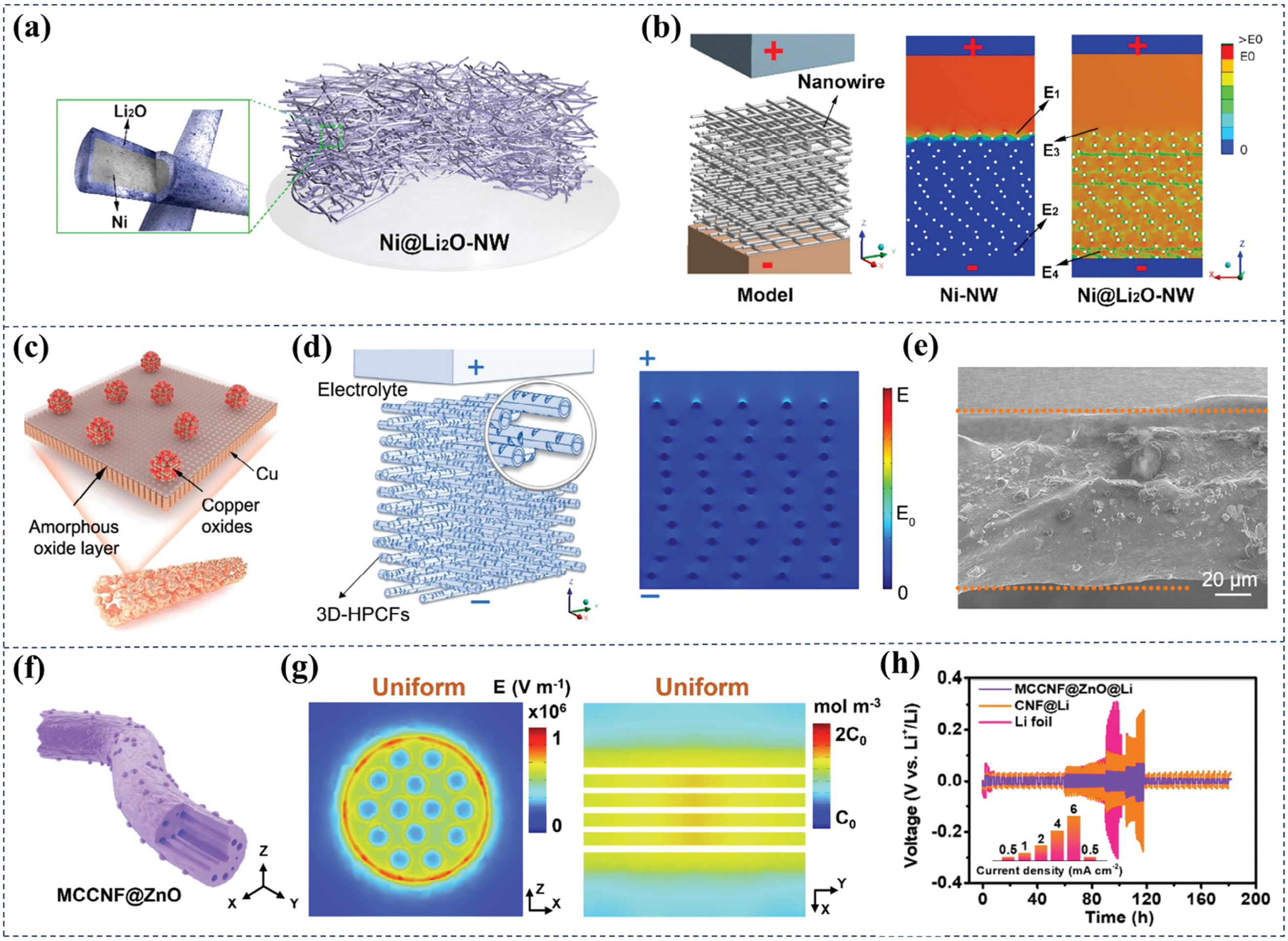

Figure 14. a) Schematic illustration of the Ni@Li_2O-NW; b) Simulation model of the domain and E-field distributions of bare Ni-NW and Ni@Li_2O-NW scaffold. Reproduced with permission.[140] Copyright 2018, Elsevier. c) A scheme of surface construction; d) simulation models and corresponding E-field distribution of 3D-HPCFs; e) Cross-sectional SEM image of 3D-HPCF electrode after 30 cycles. Reproduced with permission.[141] Copyright 2020, American Chemical Society. f) Simulation models of the domains and g) the corresponding E-field distributions and simulation of Li^+ flux distribution within MCCNF@ZnO; h) Voltage profiles of symmetric Li foil, CNF@Li and MCCNF@ZnO@Li cells at varied current densities. Reproduced with permission.[142] Copyright 2022, Elsevier.

deposition. After deep, electrochemical Li plating/stripping (15 mAh cm^{-2}) for 30 cycles, metallic Li could still be plated throughout the entire matrix and the surface remained very smooth (Figure 14e). Similarly, Chen et al.[142] designed MCCNF@ZnO, a super-lithiophilic amorphous zinc oxide-doped CNF framework with evenly distributed parallel nanochannels (Figure 14f). The use of highly interconnected parallel nanochannels and uniformly dispersed amorphous ZnO in the substrate can improve ion migration rates and enhance electrolyte affinity. Moreover, these conductive multichannels minimize partial current density, preventing electrochemical polarization and facilitating uniform metallic deposition (Figure 14g). Thus, the deposition of Li metal within the porous nanochannels and the even distribution on the lithiophilic surface of MCCNF@ZnO were evidenced. As a result, the MCCNF@ZnO@Li||Li cell exhibits good cycling with low overpotentials, 11.8, 22.6, 31.9, 45.9, and 58.3 mV at 0.5, 1, 2, 4, and 6 mA cm^{-2} respectively, indicating favorable Li plating/stripping kinetics and superior interfacial properties (Figure 14h).

Due to the polarizing effect of high dielectric materials, the E-field lines are drawn toward the high dielectric material (dictated by Gauss Law) which leads to lower divergence of the E-field in the vicinity of the Li metal deposition, and thus to a lower local E-field gradient. The study reported by Wang et al.[143] suggests that using porous 3D barium titanate (BTO) scaffolds with a high dielectric constant can suppress dendrite growth and promote a more homogeneous and denser Li metal filling within the pores of the scaffold. This is because the scaffold establishes an immobile surface charge density that opposes the applied field and draws electrical field lines toward itself, lowering the divergence of E-field in the vicinity of deposited Li. Thus, improved average plating/stripping efficiency and extended cycling life of the cell are achieved, compared to cells using bare Cu or a low dielectric scaffold material (i.e., Al_2O_3). This research suggests that high dielectric scaffolds could be a promising approach for developing safer and more efficient LMBs.

The studies discussed demonstrate that designing hosts with specific microstructures and composites to homogenize the

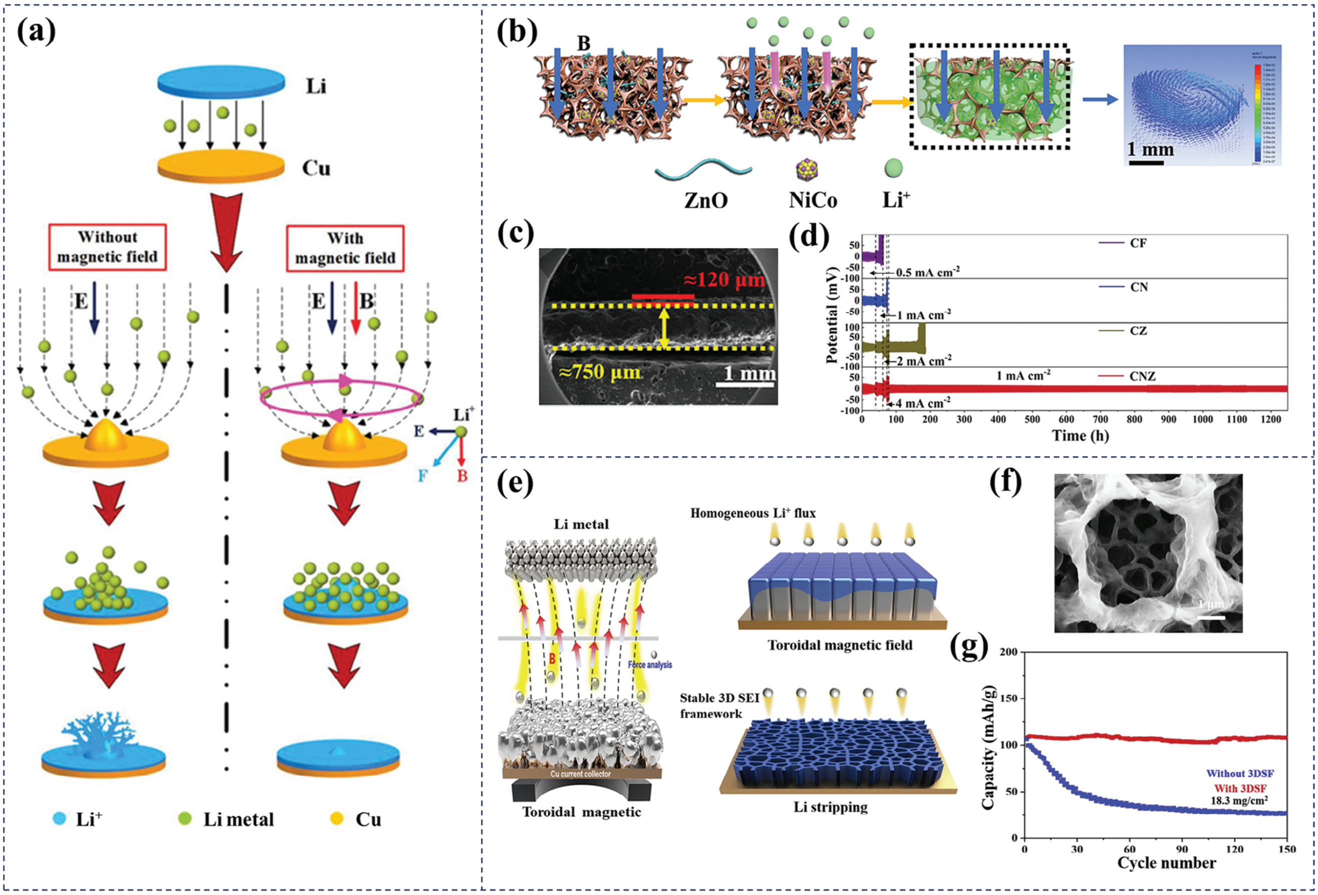

Figure 15. a) Schematically illustrating the effects of magnetic field on Li deposition. Reproduced with permission.[144] Copyright 2019, Wiley. b) Schematic diagrams of Li deposition on CNZ; c) Cross-sectional SEM image for CNZ with magnetic field for the thicknesses of 0.8 mm with lithium deposition; d) Rate performance of the four current collectors as LMAs. Reproduced with permission.[31] Copyright 2022, Wiley. e) Li deposition/stripping behaviors with TMF; f) Magnified SEM images of 3DSF after stripping Li; g) Long cycle performances of LFP full cell (18.3 mg cm^{-2}) at 1 C. Reproduced with permission.[146] Copyright 2019, Elsevier.

electric field distribution can be an effective strategy to stabilize LMAs. The more homogeneous electric field enables uniform lithium flux and stable plating, preventing localized dendrite growth. However, challenges remain in scalability and optimization of conductivity-dielectric property balance. Further studies could explore combining multiple approaches like conductive scaffolds with insulating particles or layered dielectric materials. Controlling electric field distribution by rational electrode design is also a promising direction for practical dendrite-free LMAs. Further optimization is still needed to balance factors like ionic and electronic conductivity while homogenizing the electric field.

4.2.3. Applying External Magnetic Field

During Li plating, Li-ion flux concentrated on defects or protrusions can lead to the growth of dendrites. The application of a magnetic field can create a Lorentz force on charged Li-ions, changing their diffusion direction and disrupting the ion concentration gradient, resulting in uniform ion distribution and dendrite-free behavior, known as the magnetohydrodynamics (MHD) effect. Utilizing the magnetic field to homogenize the ion distribution and suppress the dendrite formation is advantageous in several aspects. First of all, as an external field, the introduction of the magnetic field can be applied directly and conveniently to the energy storage system. Second, adopting permanent magnets is a green strategy, which can work in a sustainable way throughout the electrochemical process without consuming redundant energy. Third, as a physical driving force, the magnetic field is universally applicable to various conditions regardless of the types of metal anodes, electrolytes, or battery systems.

Shen et al.[144] applied a parallel magnetic field (magnetic field||electric field, B||E) to a lithium metal cell to reduce the formation of Li dendrites and improve electrochemical performance (**Figure** 15a). The magnetic field generates a Lorenz force perpendicular to the electric and magnetic fields, inducing convection and homogenizing Li^+ distribution. This MHD effect reduces concentration polarization of the electrode interface, resulting in enhanced electrochemical performance compared to a control sample without magnetic field. Furthermore, Sheikholeslami et al.[145] discovered that smaller ferromagnetic particles, like Fe-Co-Ni magnetic materials, provide a stronger driving force when combined with an external magnetic source. This combination accelerates Li^+ movement and leads to denser lithium deposition within the Cu foam. In view of this, Zhang et al.[31] designed a 3D Cu-based magnetic current collector containing nickel-cobalt alloy and zinc oxide (CNZ, Figure 15b). By applying a magnetic field, micromagnetic fields are introduced into the battery via the ferromagnetic nickel–cobalt alloy. This results in enhanced electron and ion movement facilitating dense Li deposition inside the CNZ. Zinc oxide, on the other hand, reduces the nucleation overpotential of lithium, resulting in an even and dense layer of lithium (Figure 15c). For all respective current densities of 0.5, 1, 2, 4, and 1 mA cm^{-2}, the CNZ symmetric cell exhibits the lowest plating/stripping overpotentials of 37, 50, 81, 97, and 35 mV. Furthermore, an exceptionally stable cycling for more than 1250 h (Figure 15d) is obtained.

Inorganic components within the SEI such as LiF and Li_2O have been found to possess favorable mechanical strength and Li^+ conductivity. Therefore Li et al.[146] introduced a toroidal magnetic field (TMF) to regulate the motion behaviors of ions (Figure 15e). Under the TMF, Li^+ migration is accelerated resulting in low concentration gradient and rendering the planar and "bottom–up" growth. After stripping, a stable and dense 3D SEI framework (3DSF) structure is formed (Figure 15f). This SEI has good mechanical strength and ionic conductivity, inducing uniform dendrite-free deposition of lithium metal. Coupling a high-loading LFP (18.3 mg cm^{-2}) with 3DSF, the full cell maintains 98.2% of initial capacity at 1 C after 150 cycles (Figure 15g).

The imposition of magnetic fields constitutes a facile and effective approach to manipulate ionic distribution and govern deposition morphologies. The utilization of magnetic current collectors encompassing ferromagnetic constituents engenders localized micro-magnetic field environments that afford enhanced regulation over ionic and electronic fluxes. However, the needs for additional magnets and optimization of the field strength/distribution increase cell complexity and weight. More critically, the scalable incorporation of magnetic components with various 3D architectures remains a challenge for practical adoption. Looking forward, further optimization of magnetic field strength, direction, and distribution in 3D architectures will be important. Integrating magnetic components with various 3D hosts in a scalable manner also needs to be conceived. If these challenges can be overcome, magnetically-regulated 3D LMAs have great potential to enable long-life and high-energy LMBs.

4.2.4. Manipulating Desirable SEI Components

While the use of 3D host materials has shown great promise in inhibiting dendrite growth and accommodating volume changes in LMAs, the 3D framework LMAs still suffer from an unstable SEI. To remedy the deficiencies of the self-formed SEI, incorporating an ASEI onto a 3D host material can further enhance the stability of the interface, facilitate "bottom–up" lithium deposition, and better accommodate the volume change of LMAs. Therefore, manipulating the desirable SEI components is a promising strategy for improving the electrochemical performance and safety of LMBs.

As one of the main components of the SEI, LiF has a positive impact on Li-ion conduction and transport. Meanwhile, the electrical insulation feature of LiF would also change the electronic conductivity of the 3D current collector, thus affecting the electroactive sites. Furthermore, LiF has a lower energy barrier for surface diffusion of Li-ions than Li_2CO_3, making it a promising material to suppress dendritic Li growth. Zhou et al.[147] developed a 3D host substrate for Li metal by combining oxidized PAN fibers, LiF nanoparticles and a Cu foil conductive bottom layer (OPAN-LiF). The OPAN-LiF host serves as a good buffer and its thickness increases slightly with deposition capacity. After lithium is stripped, the void space in the 3D framework can be largely recovered with a layer of SEI covering on the fiber surface, and polar functional groups act as regulating points to guide lithium deposition from the bottom and fill the void space gradually (**Figure 16**a,b). In contrast, Yang et al.[148] used magnetron sputtering to construct enriched-sparse ion-conductive LiF gradient layers on Cu foam host (sputtering thickness 120 nm) (Figure 16c). The homogeneous Li deposition on the Cu foam/LiF skeleton observed by in situ optical microscope further reveals the important role of sputtered LiF in guiding the Li deposition process (Figure 16d). The enhanced Li-ion conduction and transport thanks to the Cu foam/LiF skeleton contribute to a higher capacity retention ratio by 48% in full cells after 400 cycles at 0.5 C (Figure 16e).

Among various ASEI components, Li_3N stands out in restraining the growth of Li dendrites due to its high ionic conductivity (10^{-3} – 10^{-4} S cm^{-1}) and low electrical conductivity ($<10^{-12}$ S cm^{-1}). Furthermore, the Li_3N-based SEI has good thermodynamic stability, as revealed by its existence as a stable SEI component under Cs^+ sputtering using time-of-flight secondary ion mass spectrometry (Tof-SIMS) technique[149] and high Young's modulus.[150] Therefore, constructing a Li_3N-based SEI layer on a 3D host is a promising approach to stabilize the electrode/electrolyte interface, facilitate uniform Li deposition, and mitigate volume changes in LMAs. Cao et al.[142] designed a 3D Li anode with a gradient Li_3N in situ constructed on a carbon-based framework (CC/Li/Li_3N) by infusing molten lithium into g-C_3N_4 coated carbon cloth (Figure 16f). After the molten Li infusion, the generated Li_3N will spontaneously diffuse and migrate to the upper part of the electrode over time, resulting in a Li_3N gradient in the electrode. By examining the three possible Li^+ adsorption sites on the surfaces of Li (001) and Li_3N (001) and the corresponding adsorption energies, it is clear that for the surface of Li_3N (001), the N-top site is the most stable site for Li^+ adsorption with an adsorption energy of −2.44 eV (Figure 16g). Thus, the Li_3N-rich dense ASEI film can provide continuous interface protection and guarantee fast Li^+ flux across the anode/electrolyte interface. The 3D framework of the anode with uniformly distributed Li_3N can reduce the local current density and effectively alleviate infinite volume expansion during cycling, promoting dendrite-free Li deposition. The CC/Li/Li_3N anode delivers stable Li plating/stripping for over 1000 h, much longer than bare Li anode (Figure 16h).

The use of ASEIs containing beneficial SEI components has shown great promise for stabilizing the electrode/electrolyte interface and enabling uniform lithium deposition in 3D LMAs. Strategies such as constructing gradient LiF layers or dense Li_3N-rich films on 3D hosts can enhance Li-ion conduction, provide continuous interface protection, and facilitate "bottom–up" lithium growth. However, more research is still needed to understand the optimal composition and architecture. The scalable fabrication of high quality ASEI layers requires further

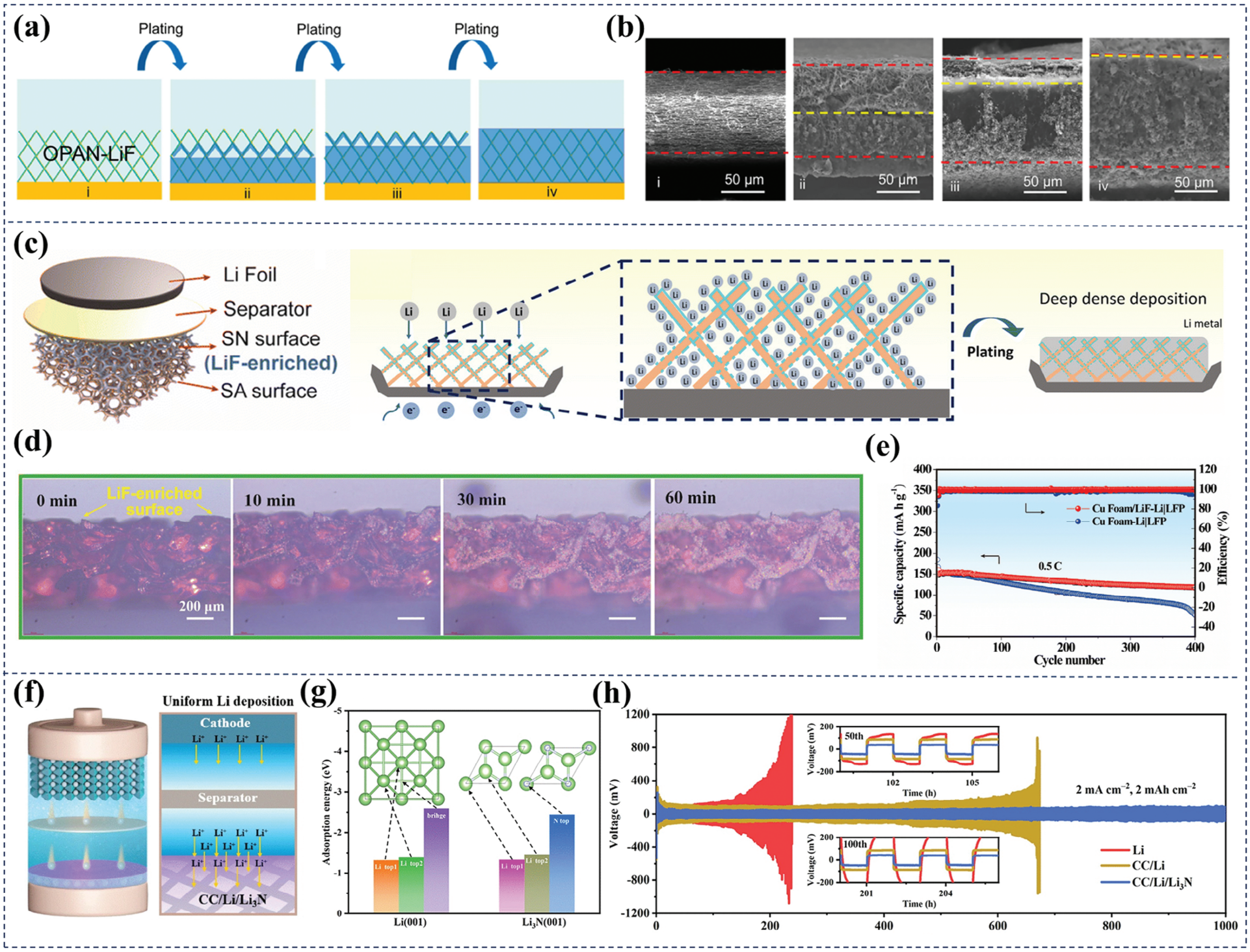

Figure 16. a) Schematic illustration and b) cross-sectional view SEM images of Li plating behaviors on OPAN-LiF: i) bare substrate, plating ii) 6, iii) 10, iv) 14 mAh cm^{-2} of Li. Reproduced with permission.[147] Copyright 2019, Elsevier. c) Half-cell configuration and scheme of Li deposition on Cu foam/LiF skeleton; d) In situ optical microscope observation of Li deposition processes on Cu foam with sputtered LiF at 2 mA cm^{-2}; e) Galvanostatic cycle tests of full cells at 0.5 C. Reproduced with permission.[148] Copyright 2022, Royal Society of Chemistry. f) The illustration of Li deposition behavior in CC/Li/Li_3N||LFP; g) Binding energy of Li on (001) surface of Li and Li_3N substrates; h) The voltage–time curves of CC/Li/Li_3N symmetric batteries at 2 mA cm^{-2}. Reproduced with permission.[142] Copyright 2022, Elsevier.

development. Overall, Other advantageous SEI components like Li_2O and Li_2S that improve ionic conductivity and flexibility can also be explored. Advanced characterization techniques should be applied to gain in-depth understanding of the role of ASEIs in regulating the lithium deposition. Machine learning may help accelerate the design and screening of ASEI materials and structures. **Table 2** summarizes the electrochemical performances and operation parameters of other previously reported strategies.

5. Conclusion and Perspectives

We summarize the main advances in achieving “bottom–up” lithium deposition through different strategies, including the construction of gradient hosts such as electrical conductivity gradient, lithiophilicity gradient, dual gradient, pore-size gradient and doping/defect design, introduction of electric field or external magnetic field, and SEI component design. Overall, the development of novel hosts provides promising solutions for solving the issues of LMAs and puts forward their practical applications in LMBs. However, there are still remaining challenges to be addressed, such as the scalability and cost-effectiveness of the fabrication materials and processes, the stability and durability of the 3D hosts under harsh conditions, and the compatibility with other battery components. Further research and innovation are needed to overcome these obstacles and achieve the ultimate goal of safe and high-performance LMBs. Finally, the problems that still exist in the design of the 3D Li metal hosts are given which can serve as the guidance for the future design of Li host (**Figure 17**).

1) The complex electrochemical processes involved in “bottom–up” lithium deposition within a 3D host can be difficult to fully understand, as they are highly dependent on the

Table 2. Electrochemical performances and operation parameters of other previously reported strategies.

Configuration	Half-cell (CE, current density [mA cm^{-2}], capacity [mAh cm^{-2}], cycle)	Symmetric cell (cycle, current density [mA cm^{-2}], capacity [mAh cm^{-2}])	Full-cell (current density, capacity retention, cycle)	Capacity of Deposited Li for full-cell [mAh cm^{-2}]	Electrolyte	References
Doping/Defects						
CuCNF + NCNF	>96.0%, 2.0, 1.0, 250	1000, 1.0, 1.0	0.5 C, 95.8%, 500 (cathode: LFP)	2.0	1 M LiTFSI in DOL&DME (1:1 in v/v) with 1% $LiNO_3$ 1 M $LiPF_6$ in EC&DEC&DMC (1:1:1 in v/v)	[137]
JFG	> 95%, 1.0, 1.0, 110	220, 1.0, 1.0	1 C, 94.0%, 220 (cathode: LFP)	N.A.	1.0 M $LiPF_6$ in EC&EMC (3:7 in v/v)	[138]
MgO_x-C	98.0%, 1.0, 1.0, 500	120, 5.0, 10.0	0.5 C, 84.0%, 100 (cathode: LFP)	N.A.	1 M LiTFSI in DOL&DME (1:1 in v/v) with 2% $LiNO_3$	[139]
Homogenized Electric Field						
Ni@Li_2O-NW	95.0%, 1.0, 1.0, 150	450, 1.0, 1.0	N.A.	N.A.	1 M $LiPF_6$ in EC&DEC (1:1 in v/v) with 0.1M $LiNO_3$	[140]
3D-HPCFs	92.5%, 1.0, 2.0, 180	1500, 0.5, 2.0	1 C, 99.9%, 300 (cathode: LFP)	2.0	1 M LiTFSI in DOL&DME (1:1 in v/v) with 1% $LiNO_3$ 1 M $LiPF_6$ in EC&DEC&DMC (1:1:1 in v/v)	[141]
MCCNF@ZnO	99.2%, 1.0, 1.0, >500	3300, 0.5, 1.0	1 C, 99.5%, 200 (cathode: LFP)	3.0	1 M LiTFSI in DOL&DME (1:1 in v/v) with 1% $LiNO_3$ 1 M $LiPF_6$ in EC&DEC (1:1 in v/v)	[142]
BTO	99.8%, 2.0, 1.0, 240	≈325, 2, 1.0	0.33 mA cm^{-2}, 99.4%, 70 (cathode: NCM811)	0	1 M $LiPF_6$ in EC&DMC (1:1 in v/v)	[143]
External Magnetic Field						
CNZ	95.0%, 1.0, 1.0, 590	560, 2.0, 1.0	1 C, 96.0%, 300 (cathode: LFP)	6.0	1 M LiTFSI in DOL&DME (1:1 in v/v) with 1% $LiNO_3$ 1 M $LiPF_6$ in EC&DEC&DMC (1:1:1 in v/v)	[31]
3DSF	>93.3%, 1.0, 1.0, 100	1700, 1.0, 1.0	3 C, 92.8%, 1000 (cathode: LFP)	10.0	1 M LiTFSI in DOL&DME (1:1 in v/v) with 1% $LiNO_3$	[146]
SEI Components						
OPAN-LiF	>98.7%, 1.0, 1.0, 380	700, 2.0, 1.0	5 C, 89.0%, 1600 (cathode: LFP)	2.5	1 M LiTFSI in DOL&DME (1:1 in v/v) with 2% $LiNO_3$	[147]
Cu foam/LiF	N.A., 1.0, 1.0, 450	1700, 2.0, 2.0	0.5 C, 80.0%, 400 (cathode: LFP)	N.A.	1 M LiTFSI in DOL&DME (1:1 in v/v) with 2% $LiNO_3$	[148]
CC/Li/Li_3N	>96.0%, 2.0, 1.0, 250	1000, 2.0, 2.0	0.5 C, 98.5%, 300 (cathode: LFP)	N.A.	1.0 M $LiPF_6$ in EC&EMC (3:7 in v/v)	[151]

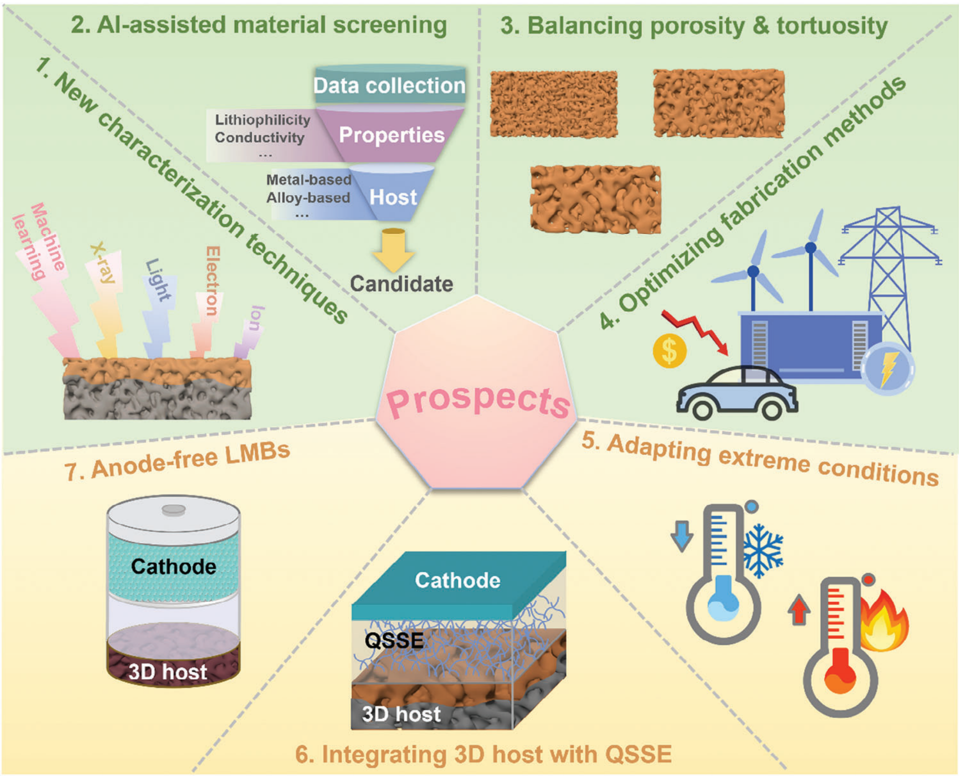

Figure 17. Future prospects for lithium metal anodes.

specific properties of the host material and electrolyte used. Understanding the behavior of Li metal and SEI is crucial when designing high-performance and safe LMBs. Therefore, investigating the electrochemical processes during Li deposition and stripping is important for developing strategies to prevent SEI degradation and improve Li cycling efficiency. Cryo-electron microscopy enables imaging of the electrode surface at low temperatures, while in situ characterization techniques allow for real-time monitoring of the Li deposition process and factors such as current density and electrolyte composition. Finite element modeling can simulate the movement of ions, electrons, and Li atoms at the electrode–electrolyte interface. These techniques provide a better perspective on the dynamics of the lithium plating/stripping process in real batteries.

2) Traditional high-throughput computations are powerful but restricted by long simulation time and limited accuracy, while purely experimental mapping is hindered by material synthesis and measurement costs. Integrating artificial intelligence (AI) with experimental work offers significant potential to enhance research efficiency, overcoming many limitations of purely computational or experimental approaches. By leveraging machine learning models trained on quantum mechanics simulations and experimental data, AI can rapidly predict the properties of potential structures, focusing on characteristics crucial for controlled Li deposition such as conductivity, lithiophilicity, and pore architecture. This predictive capacity streamlines the material design process, sparing significant time and resources by pinpointing promising candidates for synthesis and testing. Additionally, AI-driven interrogation of literature can guide researchers toward the most valuable research avenues, replacing indiscriminate experimentation with a targeted search for knowledge. The synergistic integration of experiments with AI thus offers a new paradigm for dramatically enhancing the efficiency of materials science and related fields.
3) The pore structure and tortuosity of 3D Li metal hosts have a significant impact on Li plating/stripping morphology and kinetics, which in turn affects the battery capacity, energy density, power capability, and cycle life. Smaller pores with higher surface area create more nucleation sites for uniform Li plating, but also increase electrochemical surface area for undesirable side reactions. Larger pores facilitate Li-ion transport and charge transfer, enabling higher power density, but can induce non-uniform Li deposition. A high tortuosity often hinders the uniform ions' flow, leading to localized current hotspots that can cause uneven Li deposition. Additionally, lower tortuosity in the host structure ensures a more direct pathway for Li^{+} transport, which can significantly improve the kinetics of Li plating and stripping. An optimized pore size distribution that balances these factors is ideally needed. Thus, the design of 3D lithium metal hosts necessitates a comprehensive consideration of the porosity and tortuosity in conjunction with other modification strategies to achieve a "bottom–up" Li deposition.
4) 3D Li metal hosts have emerged as a promising architecture to stabilize the LMA and enable high-energy–density LMBs. However, scalable fabrication of 3D Li metal hosts remains an

immense challenge. For instance, current methods relying on templating or additive manufacturing have their intrinsic limit for scale up and mass production. The advent and exploration of more scalable techniques like freeze casting and electrodeposition have raised considerable interests. However, narrowing the gap toward massive production still requests further development to achieve commercially viable throughput and efficient quality control. Equally important is identifying host materials that balance performance, cost, and processability. Carbon-based scaffolds are attractive due to their high electronic conductivity and light weight, but it is generally difficult to maintain volume integrity over lithium plating/stripping, resulting in the morphology change of deposited Li. Such a disadvantage can be complimentarily overcome by the selection of metal-based hosts (e.g. Cu, Ni, stainless steel) that are robust enough to suppress any volume change. Nevertheless, the increased weight and complex processing should not be overlooked. Composite-based frameworks like CNT-Cu are promising but require specialized fabrication techniques. Considering of commercial viability, processing costs must decrease significantly. Raw materials share a small fraction of the total cost compared to those of processing and fabrication. As production scales up, it is worthy to mention that recycling host and reuse of Li will be critical for minimizing not only the material costs but also the environmental impact. Capital equipment, maintenance, and labor costs must also decline along with high-volume manufacturing. In summary, scalable 3D Li metal hosts hold promise to enable high-performance next-generation batteries, but require substantial progress in material processing, cost reduction, and manufacturing innovations. Realizing the full potential, however, will rely on creative solutions across the battery supply chains.

5) Most of the current research on LMAs is conducted at room temperature (≈25 °C) and in inert atmospheres. From a practical standpoint, an ideal LMB should be able to operate steadily and safely in complicated and even extreme working environments, such as air, water, and temperatures higher than 55 °C or lower than −20 °C. However, there is a concern that these external environments are often overlooked in the research process of LMAs. Low temperatures reduce electrolyte ionic conductivity and increase charge transfer resistance, causing more severe dendrites growth. High temperatures increase side reactions and cause separator shrinking issues. Meanwhile, temperature affects Li deposition morphology, SEI layer properties, Li strength, and electrochemical performance. Introducing the "bottom–up" Li deposition strategy into the design of LMAs for extreme environments offers a promising approach to address the challenges of passivation layer formation, non-uniform Li deposition, and limited cycle life. In addition, at temperatures below −20 °C, the charge transfer kinetics of common organic liquid electrolytes and electrodes are slow, and the ionic conductivity is significantly reduced. Organic liquid electrolytes can even freeze at such low temperatures, underscoring the need for suitable electrolytes that can maintain stable low-temperature lithium metal anodes. The synergistic potential of "bottom–up" Li deposition strategies and electrolyte formulations holds great promise for enabling practical LMAs under extreme conditions, which is crucial for constructing safe, long-cycling, low-cost, and high-energy LMBs.
6) Solid-state electrolytes (SSEs) have recently gained significant attention due to their potential to enable energy storage systems with high safety and high energy density. However, the practical application of solid-state Li metal batteries (SSLMBs) is hindered by poor contact between the LMA and SSEs upon cycling. Notably, quasi-SSEs (QSSE) consisting of small amount of liquid electrolyte or plasticizer, provide excellent ionic conductivity and mechanical strength. More importantly, QSSEs provide much improved interfacial electrode/electrolyte contact. Therefore, integrating 3D host structures that enable "bottom–up" Li deposition with QSSE in LMBs may be a viable strategy to simultaneously improve safety and electrochemical performance. Understanding the fundamental failure mechanisms associated with the Li/SSE interface is also crucial for designing highly efficient SSE-based LMBs.
7) The contradiction between the safety hazard and high energy density of lithium has inspired the development and design of anode-free lithium metal batteries (AFLMBs). In AFLMBs, the only lithium source comes from the lithium stored in the cathode, showing great benefits for boosting the energy density, safety, and reducing the cost. Current collectors with a 3D porous structure contribute to an increase in available nucleation surface area, a decrease in localized current density, redistribution of the Li^+ flux, thus mitigating Li dendrite growth. Furthermore, 3D host exhibits the capability to accommodate the volume expansion. However, a 3D host structure may introduce plenty of voids and inert components, thereby weakening the volumetric energy density of AFLMBs. In addition, there are significant challenges that must be overcome before this technology can become commercially viable. A major issue is the lack of excess lithium to compensate for irreversible capacity losses during cycling, resulting in poor cycling stability. Additional challenges include controlling dendrite growth and lithium morphology, scalability of advanced materials and fabrication processes, and safety concerns related to internal shorts. "Bottom–up" Li deposition design of the 3D host enables uniform Li deposition and increases the utilization rate of active lithium, further enhancing the safety and cycling stability of AFLMBs. While the prospects are exciting, the realization of a practical and stable AFLMB with adequate cycle life remains a substantial challenge for researchers in both academia and industry working in this burgeoning field.

Acknowledgements

X.W. and Z.C. contributed equally to this work. This work was supported by Natural Science Foundation of China (Grants 52277215 and 52122702) and Nature Science Foundation of Heilongjiang Province of China (Grant JQ2021E005). S.P. acknowledges the support of Helmholtz Association.

Open access funding enabled and organized by Projekt DEAL.

Conflict of Interest

The authors declare no conflict of interest.

Keywords

3D hosts, “bottom–up” lithium deposition, construction strategies, lithium metal anodes

Received: December 8, 2023
Revised: January 28, 2024
Published online:

[1] B. Liu, J. G. Zhang, W. Xu, *Joule* **2018**, *2*, 833.
[2] Z. Chen, G. T. Kim, J. K. Kim, M. Zarrabeitia, M. Kuenzel, H. P. Liang, D. Geiger, U. Kaiser, S. Passerini, *Adv. Energy Mater.* **2021**, *11*, 2101339.
[3] X. D. Ren, L. F. Zou, X. Cao, M. H. Engelhard, W. Liu, S. D. Burton, H. Lee, C. J. Niu, B. E. Matthews, Z. H. Zhu, C. M. Wang, B. W. Arey, J. Xiao, J. Liu, J. G. Zhang, W. Xu, *Joule* **2019**, *3*, 1662.
[4] C. J. Niu, H. Lee, S. R. Chen, Q. Y. Li, J. Du, W. Xu, J. G. Zhang, M. S. Whittingham, J. Xiao, J. Liu, *Nat. Energy* **2019**, *4*, 551.
[5] Y. F. Cheng, J. B. A. Chen, Y. M. Chen, X. Ke, J. Li, Y. Yang, Z. C. Shi, *Energy Storage Mater.* **2021**, *38*, 276.
[6] H.-P. Liang, M. Zarrabeitia, Z. Chen, S. Jovanovic, S. Merz, J. Granwehr, S. Passerini, D. Bresser, *Adv. Energy Mater.* **2022**, *12*, 2200013.
[7] Q. Y. Yang, Z. Yu, Y. Li, W. Zhang, H. W. Yuan, H. J. Li, W. Ma, S. M. Zhu, S. Li, *Rare Met.* **2022**, *41*, 2800.
[8] S. Zhou, C. Y. Fu, Z. Chang, Y. F. Zhang, D. M. Xu, Q. He, S. M. Chai, X. Y. Meng, M. Y. Feng, Y. P. Zhang, J. D. Lin, A. Q. Pan, *Energy Storage Mater.* **2022**, *47*, 482.
[9] R. Xu, X. B. Cheng, C. Yan, X. Q. Zhang, Y. Xiao, C. Z. Zhao, J. Q. Huang, Q. Zhang, *Matter* **2019**, *1*, 317.
[10] Z. Y. Tu, S. Choudhury, M. J. Zachman, S. Y. Wei, K. H. Zhang, L. F. Kourkoutis, L. A. Archer, *Joule* **2017**, *1*, 394.
[11] Y. Liu, D. Lin, P. Y. Yuen, K. Liu, J. Xie, R. H. Dauskardt, Y. Cui, *Adv. Mater.* **2017**, *29*, 1605531.
[12] Z. Chen, H. P. Liang, Z. Lyu, N. Paul, G. Ceccio, R. Gilles, M. Zarrabeitia, A. Innocenti, M. Jasarevic, G. T. Kim, S. Passerini, D. Bresser, *Chem. Eng. J.* **2023**, *467*, 143530.
[13] L. Dong, Y. Liu, K. Wen, D. Chen, D. Rao, J. Liu, B. Yuan, Y. Dong, Z. Wu, Y. Liang, *Adv. Sci.* **2022**, *9*, 2104699.
[14] A. M. Haregewoin, A. S. Wotango, B. J. Hwang, *Energy Environ. Sci.* **2016**, *9*, 1955.
[15] W. M. Zhao, Y. J. Ji, Z. R. Zhang, M. Lin, Z. Wu, X. Zheng, Q. Li, Y. Yang, *Curr. Opin. Electrochem.* **2017**, *6*, 84.
[16] J. Zheng, M. H. Engelhard, D. Mei, S. Jiao, B. J. Polzin, J.-G. Zhang, W. Xu, *Nat. Energy* **2017**, *2*, 1.
[17] C.-C. Lin, Z. Chen, H. Euchner, T. Eisenmann, K. Geng, T. Diemant, S. Fang, C.-H. Yen, S. Passerini, C.-C. Hu, *ACS Appl. Energy Mater.* **2023**, *6*, 2140.
[18] Z. F. Liu, Y. J. Jiang, Q. M. Hu, S. T. Guo, L. Yu, Q. Li, Q. Liu, X. L. Hu, *Energy Environ. Mater.* **2021**, *4*, 336.
[19] H. Y. Huo, X. N. Li, Y. Chen, J. N. Liang, S. X. Deng, X. J. Gao, K. Doyle-Davis, R. Y. Li, X. X. Guo, Y. Shen, C. W. Nan, X. L. Sun, *Energy Storage Mater.* **2020**, *29*, 361.
[20] H. Jiang, X. Lin, C. Wei, J. Feng, X. Tian, *Small* **2022**, *18*, 2104264.
[21] H. D. Nguyen, G. T. Kim, J. L. Shi, E. Paillard, P. Judeinstein, S. Lyonnard, D. Bresser, C. Iojoiu, *Energy Environ. Sci.* **2018**, *11*, 3298.
[22] Z. Chen, G.-T. Kim, Z. Wang, D. Bresser, B. Qin, D. Geiger, U. Kaiser, X. Wang, Z. X. Shen, S. Passerini, *Nano Energy* **2019**, *64*, 103986.
[23] X. W. Yu, A. Manthiram, *Energy Storage Mater.* **2021**, *34*, 282.
[24] K. Yang, L. K. Chen, J. B. Ma, Y. B. He, F. Y. Kang, *InfoMat* **2021**, *3*, 1195.
[25] Y. Wang, Z. Chen, Y. Wu, Y. Li, Z. Yue, M. Chen, *ACS Appl. Mater. Interfaces* **2023**, *15*, 21526.
[26] M. Chen, W. Liu, Z. Yue, Y. Wang, Y. Wu, Y. Li, Z. Chen, *Batteries* **2023**, *9*, 270.
[27] Y. C. Liu, D. Gao, H. F. Xiang, X. Y. Feng, Y. Yu, *Energy Fuels* **2021**, *35*, 12921.
[28] S. Park, H. J. Jin, Y. S. Yun, *Adv. Mater.* **2020**, *32*, 2070386.
[29] Y. Z. Chen, A. Elangovan, D. L. Zeng, Y. F. Zhang, H. Z. Ke, J. Li, Y. B. Sun, H. S. Cheng, *Adv. Funct. Mater.* **2020**, *30*, 906444.
[30] J. Yun, B. K. Park, E. S. Won, S. H. Choi, H. C. Kang, J. H. Kim, M. S. Park, J. W. Lee, *ACS Energy Lett.* **2020**, *5*, 3108.
[31] J. L. Zhang, H. B. Chen, M. Wen, K. Shen, Q. Chen, G. Y. Hou, Y. P. Tang, *Adv. Funct. Mater.* **2022**, *32*, 2110110.
[32] J. R. Wang, M. M. Wang, F. Chen, Y. X. Li, L. M. Zhang, Y. Zhao, C. H. Chen, *Energy Storage Mater.* **2021**, *34*, 22.
[33] H. J. Noh, M. H. Lee, B. G. Kim, J. H. Park, S. M. Lee, J. H. Choi, *ACS Appl. Mater. Interfaces* **2021**, *13*, 55227.
[34] C. Y. Lu, M. Tian, X. J. Zheng, C. H. Wei, M. H. Rummeli, P. Strasser, R. Z. Yang, *Chem. Eng. J.* **2022**, *430*, 132722.
[35] T. Zhang, C. Li, F. Wang, A. Noori, M. F. Mousavi, X. Xia, Y. Zhang, *Chem. Rec.* **2022**, *22*, e202200083.
[36] Y. C. Liu, B. Y. Yuan, C. Sun, Y. H. Lu, X. P. Lin, M. H. Chen, Y. S. Xie, S. Q. Zhang, C. Lai, *Adv. Funct. Mater.* **2022**, *32*, 2202771.
[37] T. Li, S. Gu, L. Chen, L. Zhang, X. Qin, Z. Huang, Y. B. He, W. Lv, F. Kang, *Small* **2022**, *18*, 2203273.
[38] Y. Nan, S. Li, Y. Shi, S. Yang, B. Li, *Small* **2019**, *15*, 1903520.
[39] Y. Zhao, L. Wang, J. Zou, Q. Ran, L. Li, P. Chen, H. Yu, J. Gao, X. Niu, *J. Energy Chem.* **2022**, *65*, 666.
[40] D. Y. Han, G. J. Song, S. H. Kim, S. J. Park, *Small Struct.* **2022**, *3*, 2200120.
[41] K. Yan, Z. D. Lu, H. W. Lee, F. Xiong, P. C. Hsu, Y. Z. Li, J. Zhao, S. Chu, Y. Cui, *Nat. Energy* **2016**, *1*, 16010.
[42] S. S. Liu, Y. L. Ma, Z. X. Zhou, S. F. Lou, H. Huo, P. J. Zuo, J. J. Wang, C. Y. Du, G. P. Yin, Y. Z. Gao, *Energy Storage Mater.* **2020**, *33*, 423.
[43] G. Huang, J. Han, F. Zhang, Z. Wang, H. Kashani, K. Watanabe, M. Chen, *Adv. Mater.* **2019**, *31*, 1805334.
[44] Q. W. Ran, L. P. Wang, L. Li, Y. L. Zhao, Z. G. Lu, S. Y. Chen, J. Zou, P. Y. Chen, J. Gao, X. B. Niu, *Chem. Eng. J.* **2021**, *426*, 130780.
[45] S. Wang, L. Zhang, X. Cai, T. Chu, D. Liu, C. Han, X. Qin, F. Kang, B. Li, *J. Mater. Chem. A* **2021**, *9*, 25004.
[46] B. Sun, Q. Zhang, W. Xu, R. Zhao, H. Zhu, W. Lv, X. Li, N. Yang, *Nano Energy* **2022**, *94*, 106937.
[47] S. Zhang, W. Deng, X. Zhou, B. He, J. Liang, F. Zhao, Q. Guo, Z. Liu, *Mater. Today Energy* **2021**, *21*, 100770.
[48] H. H. Weldeyohannes, L. H. Abrha, Y. Nikodimos, K. N. Shitaw, T. M. Hagos, C. J. Huang, C. H. Wang, S. H. Wu, W. N. Su, B. J. Hwang, *J. Power Sources* **2021**, *506*, 230204.
[49] X. L. Yan, Q. F. Zhang, W. J. Xu, Q. S. Xie, P. F. Liu, Q. L. Chen, H. F. Zheng, L. S. Wang, Z. Z. Zhu, D. L. Peng, *J. Mater. Chem. A* **2020**, *8*, 1678.
[50] S. B. Huang, H. Zhang, L. Z. Fan, *ACS Appl. Mater. Interfaces* **2022**, *14*, 17539.
[51] H. He, L. Zeng, D. Luo, J. He, X. Li, Z. Guo, C. Zhang, *Adv. Mater.* **2023**, *35*, 2211498.
[52] J. H. Kwak, S. Park, S. Shin, S. Park, C. Kang, S.-H. Yu, J. Moon, H.-D. Lim, *Energy Storage Mater.* **2023**, *59*, 102762.
[53] X. He, Y. Ni, Y. Li, H. Sun, Y. Lu, H. Li, Z. Yan, K. Zhang, J. Chen, *Adv. Mater.* **2022**, *34*, 2106565.
[54] M. Wu, Z. Wen, Y. Liu, X. Wang, L. Huang, *J. Power Sources* **2011**, *196*, 8091.
[55] Y. Jin, S. Fang, M. Chai, L. Yang, K. Tachibana, S. Hirano, *J. Power Sources* **2013**, *226*, 210.

[56] Y. Zhang, J. Qian, W. Xu, S. M. Russell, X. Chen, E. Nasybulin, P. Bhattacharya, M. H. Engelhard, D. Mei, R. Cao, F. Ding, A. V. Cresce, K. Xu, J. G. Zhang, *Nano Lett.* **2014**, *14*, 6889.

[57] C. P. Yang, Y. X. Yin, S. F. Zhang, N. W. Li, Y. G. Guo, *Nat. Commun.* **2015**, *6*, 8058.

[58] Z. Liang, D. Lin, J. Zhao, Z. Lu, Y. Liu, C. Liu, Y. Lu, H. Wang, K. Yan, X. Tao, *Proc. Natl. Acad. Sci. U. S. A.* **2016**, *113*, 2862.

[59] Z. Wang, X. Li, Y. Chen, K. Pei, Y. W. Mai, S. Zhang, J. Li, *Chem* **2020**, *6*, 2878.

[60] Z. Hu, W. Deng, B. He, J. Liang, X. Zhou, Z. Liu, *Nano Energy* **2022**, *93*, 106805.

[61] F. Cheng, X. Yang, O. Ka, L. Wen, X. Wang, W. Lu, *J. Mater. Chem. A* **2023**, *11*, 4205.

[62] S. S. Zhang, X. Fan, C. Wang, *Electrochim. Acta* **2017**, *258*, 1201.

[63] V. I. Kalikmanov, in *Nucleation Theory*, Springer, Berlin **2012**.

[64] P. C. Zou, Y. M. Sui, H. C. Zhan, C. Y. Wang, H. L. Xin, H. M. Cheng, F. Y. Kang, C. Yang, *Chem. Rev.* **2021**, *121*, 5986.

[65] A. Pei, G. Zheng, F. Shi, Y. Li, Y. Cui, *Nano Lett.* **2017**, *17*, 1132.

[66] P. Biswal, S. Stalin, A. Kludze, S. Choudhury, L. A. Archer, *Nano Lett.* **2019**, *19*, 8191.

[67] D. Kashchiev, *J. Chem. Phys.* **1982**, *76*, 5098.

[68] D. W. Oxtoby, D. Kashchiev, *J. Chem. Phys.* **1994**, *100*, 7665.

[69] D. R. Ely, R. E. Garcia, *J. Electrochem. Soc.* **2013**, *160*, A662.

[70] Y. Q. Chen, Y. Luo, H. Z. Zhang, C. Qu, H. M. Zhang, X. F. Li, *Small Methods* **2019**, *3*, 1800551.

[71] D. Wang, W. Zhang, W. Zheng, X. Cui, T. Rojo, Q. Zhang, *Adv. Sci.* **2017**, *4*, 1600168.

[72] M. Ohring, *Appl. Opt.* **1992**, *31*, 7162.

[73] Z. Z. Tong, S. B. Wang, Y. K. Liao, S. F. Hu, R. S. Liu, *ACS Appl. Mater. Interfaces* **2020**, *12*, 47181.

[74] D. Aurbach, Y. Cohen, *J. Electrochem. Soc.* **1997**, *144*, 3355.

[75] C. Y. Tang, S. J. Dillon, *J. Electrochem. Soc.* **2016**, *163*, A1660.

[76] W. Cao, Q. Li, X. Yu, H. Li, *eScience* **2022**, *2*, 47.

[77] R. Akolkar, *J. Power Sources* **2014**, *246*, 84.

[78] J. N. Chazalviel, *Phys. Rev. A* **1990**, *42*, 7355.

[79] H. J. S. Sand, *Philos. Mag.* **1901**, *1*, 45.

[80] G. Marshall, P. Mocskos, *Phys. Rev. E* **1997**, *55*, 549.

[81] C. Brissot, M. Rosso, J. N. Chazalviel, S. Lascaud, *J. Power Sources* **1999**, *81*, 925.

[82] P. Bai, J. Li, F. R. Brushett, M. Z. Bazant, *Energy Environ. Sci.* **2016**, *9*, 3221.

[83] B. G. Kim, D. W. Kang, G. Park, S. H. Park, S.-M. Lee, J. W. Choi, *Chem. Eng. J.* **2021**, *422*, 130017.

[84] Y. Tang, K. Shen, Z. Lv, X. Xu, G. Hou, H. Cao, L. Wu, G. Zheng, Y. Deng, *J. Power Sources* **2018**, *403*, 82.

[85] H. Zhao, D. Lei, Y. B. He, Y. Yuan, Q. Yun, B. Ni, W. Lv, B. Li, Q. H. Yang, F. Kang, *Adv. Energy Mater.* **2018**, *8*, 1800266.

[86] W. Li, S. Zheng, Y. Gao, D. Feng, Y. Ru, T. Zuo, B. Chen, Z. Zhang, Z. Gao, H. Geng, *Nano Lett.* **2023**, *23*, 7805.

[87] G. J. Lim, Z. Lyu, X. Zhang, J. J. Koh, Y. Zhang, C. He, S. Adams, J. Wang, J. Ding, *J. Mater. Chem. A* **2020**, *8*, 9058.

[88] C. Chen, S. Li, P. H. Notten, Y. Zhang, Q. Hao, X. Zhang, W. Lei, *ACS Appl. Mater. Interfaces* **2021**, *13*, 24785.

[89] W. Chen, S. Li, C. Wang, H. Dou, X. Zhang, *Energy Environ. Mater.* **2023**, *6*, e12412.

[90] Y. Li, J. Li, H. Xiao, T. Xie, W. Zheng, J. He, H. Zhu, S. Huang, *Adv. Funct. Mater.* **2023**, *33*, 2213905.

[91] C. Li, C. Zheng, F. Cao, Y. Zhang, X. Xia, *J. Electron. Mater.* **2022**, *51*, 4107.

[92] C. Lu, M. Tian, C. Wei, J. Zhou, M. H. Rümmeli, R. Yang, *J. Colloid Interface Sci.* **2023**, *632*, 1.

[93] Q. Kang, Z. Zhuang, Y. Li, Y. Zuo, J. Wang, Y. Liu, C. Shi, J. Chen, H. Li, P. Jiang, *Nano Res.* **2023**, *16*, 9240.

[94] Z. Feng, L. Mo, K. Chen, Y. Qian, L. Zhang, S. Yang, R. Bagherzadeh, F. Lai, W. Fan, C. Zhang, *Sci. China Mater.* **2023**, *66*, 3065.

[95] H. Chen, A. Pei, J. Wan, D. Lin, R. Vilá, H. Wang, D. Mackanic, H.-G. Steinrück, W. Huang, Y. Li, *Joule* **2020**, *4*, 938.

[96] J. Wu, Z. Rao, X. Liu, Y. Shen, L. Yuan, Z. Li, X. Xie, Y. Huang, *Adv. Funct. Mater.* **2021**, *31*, 2009961.

[97] Y. Zhang, W. Luo, C. Wang, Y. Li, C. Chen, J. Song, J. Dai, E. M. Hitz, S. Xu, C. Yang, *Proc. Natl. Acad. Sci. U. S. A.* **2017**, *114*, 3584.

[98] J. Zhou, F. Wu, G. Wei, Y. Hao, Y. Mei, L. Li, M. Xie, R. Chen, *J. Power Sources* **2021**, *495*, 229773.

[99] H. Jiang, Y. Zhou, C. Guan, M. Bai, F. Qin, M. Yi, J. Li, B. Hong, Y. Lai, *Small* **2022**, *18*, 2107641.

[100] H. Qi, A. W. Xie, R. Z. Zuo, *Energy Storage Mater.* **2022**, *45*, 541.

[101] Z. Liang, G. Y. Zheng, C. Liu, N. Liu, W. Y. Li, K. Yan, H. B. Yao, P. C. Hsu, S. Chu, Y. Cui, *Nano Lett.* **2015**, *15*, 2910.

[102] J. Li, P. Zou, S. W. Chiang, W. Yao, Y. Wang, P. Liu, C. Liang, F. Kang, C. Yang, *Energy Storage Mater.* **2020**, *24*, 700.

[103] S. Jin, S. Xin, L. Wang, Z. Du, L. Cao, J. Chen, X. Kong, M. Gong, J. Lu, Y. Zhu, *Adv. Mater.* **2016**, *28*, 9094.

[104] C. Zhang, Z. Huang, W. Lv, Q. Yun, F. Kang, Q.-H. Yang, *Carbon* **2017**, *123*, 744.

[105] P. Zou, Y. Wang, S.-W. Chiang, X. Wang, F. Kang, C. Yang, *Nat. Commun.* **2018**, *9*, 464.

[106] S. H. Wang, Y. X. Yin, T. T. Zuo, W. Dong, J. Y. Li, J. L. Shi, C. H. Zhang, N. W. Li, C. J. Li, Y. G. Guo, *Adv. Mater.* **2017**, *29*, 1703729.

[107] S. S. Chi, Y. Liu, W. L. Song, L. Z. Fan, Q. Zhang, *Adv. Funct. Mater.* **2017**, *27*, 1700348.

[108] X. B. Cheng, T. Z. Hou, R. Zhang, H. J. Peng, C. Z. Zhao, J. Q. Huang, Q. Zhang, *Adv. Mater.* **2016**, *28*, 2888.

[109] S. H. Hong, D. H. Jung, J. H. Kim, Y. H. Lee, S. J. Cho, S. H. Joo, H. W. Lee, K. S. Lee, S. Y. Lee, *Adv. Funct. Mater.* **2020**, *30*, 1908868.

[110] M. Salanne, B. Rotenberg, K. Naoi, K. Kaneko, P. L. Taberna, C. P. Grey, B. Dunn, P. Simon, *Nat. Energy* **2016**, *1*, 16070.

[111] C. Niu, H. Pan, W. Xu, J. Xiao, J.-G. Zhang, L. Luo, C. Wang, D. Mei, J. Meng, X. Wang, Z. Liu, L. Mai, J. Liu, *Nat. Nanotechnol.* **2019**, *14*, 594.

[112] Z. Lu, Q. Liang, B. Wang, Y. Tao, Y. Zhao, W. Lv, D. Liu, C. Zhang, Z. Weng, J. Liang, *Adv. Energy Mater.* **2019**, *9*, 1803186.

[113] K. H. Park, D. W. Kang, J. W. Park, J. H. Choi, S. J. Hong, S. H. Song, S. M. Lee, J. Moon, B. G. Kim, *J. Mater. Chem. A* **2021**, *9*, 1822.

[114] L. Fan, S. Li, L. Liu, W. Zhang, L. Gao, Y. Fu, F. Chen, J. Li, H. L. Zhuang, Y. Lu, *Adv. Energy Mater.* **2018**, *8*, 1802350.

[115] P. C. Zou, S. W. Chiang, H. C. Zhan, Y. M. Sui, K. W. Liu, S. Y. Hu, S. Y. Su, J. Li, F. Y. Kang, C. Yang, *Adv. Funct. Mater.* **2020**, *30*, 1910532.

[116] Y. Nan, S. M. Li, Y. Z. Shi, S. B. Yang, B. Li, *Small* **2019**, *15*, 1903520.

[117] S. Cui, P. Zhai, W. Yang, Y. Wei, J. Xiao, L. Deng, Y. Gong, *Small* **2020**, *16*, 1905620.

[118] M. Wan, S. Kang, L. Wang, H.-W. Lee, G. W. Zheng, Y. Cui, Y. Sun, *Nat. Commun.* **2020**, *11*, 829.

[119] H. Fan, S. Li, Y. Yu, H. Xu, M. Jiang, Y. Huang, J. Li, *Adv. Funct. Mater.* **2021**, *31*, 2100978.

[120] S.-S. Chi, Q. Wang, B. Han, C. Luo, Y. Jiang, J. Wang, C. Wang, Y. Yu, Y. Deng, *Nano Lett.* **2020**, *20*, 2724.

[121] S. H. Choi, S. J. Lee, D. J. Yoo, J. H. Park, J. H. Park, Y. N. Ko, J. Park, Y. E. Sung, S. Y. Chung, H. Kim, *Adv. Energy Mater.* **2019**, *9*, 1902278.

[122] Y. L. Zhao, L. P. Wang, J. Zou, Q. W. Ran, L. Li, P. Y. Chen, H. L. Yu, J. Gao, X. B. Niu, *J. Energy Chem.* **2022**, *65*, 666.

[123] Z. Zhu, B. Liu, Y. Qian, Y. Fang, X. Lei, X. Liu, J. Zhou, Y. Qian, G. Wang, *Adv. Energy Mater.* **2023**, *13*, 2203687.

[124] B. Hong, H. L. Fan, X. B. Cheng, X. L. Yan, S. Hong, Q. Y. Dong, C. H. Gao, Z. Zhang, Y. Q. Lai, Q. Zhang, *Energy Storage Mater.* **2019**, *16*, 259.

[125] D. D. Li, Y. Gao, C. Xie, Z. J. Zheng, *Appl. Phys. Rev.* **2022**, *9*, 011424.

[126] Y. Lv, Q. X. Zhang, C. Li, C. Ma, W. Y. Guan, X. Z. Liu, Y. Ding, *ACS Sustainable Chem. Eng.* **2022**, *10*, 7188.
[127] J. Pu, J. C. Li, K. Zhang, T. Zhang, C. W. Li, H. X. Ma, J. Zhu, P. V. Braun, J. Lu, H. G. Zhang, *Nat. Commun.* **2019**, *10*, 1896.
[128] T. Li, S. C. Gu, L. K. Chen, L. H. Zhang, X. Y. Qin, Z. J. Huang, Y. B. He, W. Lv, F. Y. Kang, *Small* **2022**, *18*, 2203273.
[129] H. F. Zheng, Q. F. Zhang, Q. L. Chen, W. J. Xu, Q. S. Xie, Y. X. Cai, Y. T. Ma, Z. S. Qiao, Q. Luo, J. Lin, L. S. Wang, B. H. Qu, B. S. Sa, D. L. Peng, *J. Mater. Chem. A* **2020**, *8*, 313.
[130] L. Zhang, H. F. Zheng, B. Liu, Q. S. Xie, Q. L. Chen, L. Lin, J. Lin, B. H. Qu, L. S. Wang, D. L. Peng, *J. Energy Chem.* **2021**, *57*, 392.
[131] Q. C. Cai, X. Y. Qin, K. Lin, Z. J. Yang, X. Hu, T. Li, F. Y. Kang, B. H. Li, *Nano Lett.* **2021**, *21*, 10252.
[132] J. Lee, E. S. Won, D. M. Kim, H. Kim, B. Kwon, K. Park, S. Jo, S. Lee, J. W. Lee, K. T. Lee, *ACS Appl. Mater. Interfaces* **2021**, *13*, 33056.
[133] H. Liu, J. Di, P. Wang, R. Gao, H. Tian, P. F. Ren, Q. X. Yuan, W. X. Huang, R. P. Liu, Q. Liu, M. Feng, *Carbon Energy* **2022**, *4*, 654.
[134] Z. W. Yang, C. Wu, S. Li, L. Qiu, Z. G. Yang, Y. J. Zhong, B. H. Zhong, Y. Song, G. K. Wang, Y. X. Liu, Z. G. Wu, X. D. Guo, *Adv. Funct. Mater.* **2022**, *32*, 2107897.
[135] J. H. Zhou, F. Wu, G. L. Wei, Y. T. Hao, Y. Mei, L. Li, M. Xie, R. J. Chen, *J. Power Sources* **2021**, *495*, 229773.
[136] C. Zhang, R. Lyu, W. Lv, H. Li, W. Jiang, J. Li, S. Gu, G. Zhou, Z. Huang, Y. Zhang, J. Wu, Q.-H. Yang, F. Kang, *Adv. Mater.* **2019**, *31*, 1904991.
[137] X. Cheng, J. J. Ban, Q. Wang, H. J. Xu, G. S. Shao, J. H. Hu, G. Q. Cao, *Appl. Surf. Sci.* **2021**, *563*, 150247.
[138] J. J. Ma, J. L. Yang, Y. W. Zhao, Q. L. Ma, Z. Wang, W. Qian, B. Xia, L. Li, W. H. Zeng, J. X. Chen, H. W. Xu, S. S. Chen, D. P. He, Z. B. Wang, S. C. Mu, *Chem. Eng. J.* **2022**, *433*, 133561.
[139] Q. P. Wu, Z. G. Yao, A. C. Du, H. Wu, M. S. Huang, J. Xu, F. H. Cao, C. L. Li, *J. Mater. Chem. A* **2021**, *9*, 5606.
[140] P. C. Zou, S. W. Chiang, J. Li, Y. Wang, X. Y. Wang, D. Wu, A. Nairan, F. Y. Kang, C. Yang, *Energy Storage Mater.* **2019**, *18*, 155.
[141] D. Zhang, A. Dai, M. Wu, K. Shen, T. Xiao, G. Y. Hou, J. Lu, Y. P. Tang, *ACS Energy Lett.* **2020**, *5*, 180.
[142] A. L. Chen, M. Y. Gao, L. L. Mo, J. Wang, Z. Xu, Y. E. Miao, T. X. Liu, *J. Colloid Interface Sci.* **2022**, *614*, 138.
[143] C. Wang, M. Liu, M. Thijs, F. G. B. Ooms, S. Ganapathy, M. Wagemaker, *Nat. Commun.* **2021**, *12*, 6536.
[144] K. Shen, Z. Wang, X. Bi, Y. Ying, D. Zhang, C. Jin, G. Hou, H. Cao, L. Wu, G. Zheng, *Adv. Energy Mater.* **2019**, *9*, 1900260.
[145] M. Sheikholeslami, M. Gorji-Bandpy, *Powder Technol.* **2014**, *256*, 490.
[146] Y. Li, M. J. Xiao, C. L. Shen, L. M. Cui, W. Yang, C. Zhang, X. H. Chen, L. Q. Mai, Y. Zhao, X. Xu, *Cell Rep. Phys. Sci.* **2022**, *3*, 101080.
[147] S. Zhou, Y. F. Zhang, S. M. Chai, I. Usman, Y. Qiao, S. Z. Luo, X. F. Xie, J. Chen, S. Q. Liang, A. Q. Pan, H. S. Zhou, *Chem. Eng. J.* **2021**, *404*, 126508.
[148] H. Yang, H. F. Zheng, H. M. Yu, B. H. Qu, L. B. Chen, J. M. Niu, Y. J. Chen, *Nanoscale* **2022**, *14*, 13722.
[149] N. Ahmad, S. Sun, P. Yu, W. Yang, *Adv. Funct. Mater.* **2022**, *32*, 2201528.
[150] S. Ni, M. Zhang, C. Li, R. Gao, J. Sheng, X. Wu, G. Zhou, *Adv. Mater.* **2023**, *35*, 2209028.
[151] W. Z. Cao, W. M. Chen, M. Lu, C. Zhang, D. Tian, L. Wang, F. Q. Yu, *J. Energy Chem.* **2023**, *76*, 648.

Xi Wang is currently a Ph.D. student under the supervision of Prof. Minghua Chen and Prof. Zhen Chen at Harbin University of Science and Technology. Her research interest focuses on lithium metal anodes, especially 3D current collectors, to enable high energy density lithium–metal batteries.

Zhen Chen is currently a professor at the Harbin University of Science and Technology. She received her B.S. degree at the Southeast University (SEU) in China in 2014, and Ph.D. degree at the Nanyang Technological University (NTU) in Singapore in 2018. From 2019 to 2022, she worked as a scientist at the Helmholtz Institute Ulm (HIU), Karlsruhe Institute of Technology (KIT) in Germany. Her research activities mainly focus on the development of key materials and relevant applications in the field of electrochemical energy storage with a special focus on developing high-performance solid-state secondary batteries.

Kai Jiang is currently a professor at Huazhong University of Science and Technology. He received his B.S. degree and Ph.D. degree from Wuhan University in 1999 and 2006, respectively. From 2007 to 2009, he worked as a visiting scientist at Auburn University in the United States. Before joining Huazhong University of Science and Technology in 2012, he worked as a postdoctoral researcher at the Massachusetts Institute of Technology. His main research directions are new energy materials and new energy storage technologies.

Minghua Chen is currently a professor at Harbin University of Science and Technology since 2017. He received Ph.D. from Harbin University of Science and Technology, followed by exchange student and visiting scientist at Nanyang Technological University (NTU) from 2013 to 2016. His research interests are dielectric insulation characteristics of engineering dielectric, and the application and development of new energy materials and devices.

Stefano Passerini is Distinguished Senior Fellow at Karlsruhe Institute of Technology (Germany). His research focuses on the understanding and development of materials for high-energy batteries, with the goal to create sustainable energy storage systems from environmentally friendly and available materials and processes. Co-author of about 800 scientific papers (Scopus H-Index: 118; > 50000 citations), a few book chapters and several international patents, he has been awarded the Research Award of the Electrochemical Society Battery Division. He is fellow of the International Society of Electrochemistry and the Electrochemical Society Inc., and member of the Leopoldina German Academy of Science.